1.0

4 5
5 0
5 6
6 3

2.8

2.5

3.2

2.2

3 6

4 0

2.0

1.1

1.8

1.25

1.4

1.6

MICROCOPY RESOLUTION TEST CHART
NATIONAL BUREAU OF STANDARDS-1963-A

LEVEL II

A FAR-INFRARED LASER STUDY
OF JOSEPHSON POINT CONTACTS

VE RI TAS

By

David A. Weitz

May 1978

Technical Report No. 14

TR-14

D D C
RECEIVED
JUL 17 1978

151 p.

Division of Applied Sciences

Harvard University   Cambridge, Massachusetts

410 457

78 07 12 006

SECURITY CLASSIFICATION OF THIS PAGE *(When Data Entered)*

REPORT DOCUMENTATION PAGE		READ INSTRUCTIONS BEFORE COMPLETING FORM
1. REPORT NUMBER Technical Report No. 14	2. GOVT ACCESSION NO.	3. RECIPIENT'S CATALOG NUMBER
4. TITLE *(and Subtitle)* A FAR-INFRARED LASER STUDY OF JOSEPHSON POINT CONTACTS		5. TYPE OF REPORT & PERIOD COVERED Interim Report
		6. PERFORMING ORG. REPORT NUMBER
7. AUTHOR(s) David Allan Weitz		8. CONTRACT OR GRANT NUMBER(s) N00014-77-C-0085 N00014-75-C-0648 NSF DMR 76-11323
9. PERFORMING ORGANIZATION NAME AND ADDRESS Division of Applied Sciences Harvard University Cambridge, Mass. 02138		10. PROGRAM ELEMENT, PROJECT, TASK AREA & WORK UNIT NUMBERS
11. CONTROLLING OFFICE NAME AND ADDRESS		12. REPORT DATE May 1978
		13. NUMBER OF PAGES 152
14. MONITORING AGENCY NAME & ADDRESS *(if different from Controlling Office)*		15. SECURITY CLASS. *(of this report)* Unclassified
		15a. DECLASSIFICATION/DOWNGRADING SCHEDULE

16. DISTRIBUTION STATEMENT *(of this Report)*

Approved for public release; distribution unlimited.

17. DISTRIBUTION STATEMENT *(of the abstract entered in Block 20, if different from Report)*

18. SUPPLEMENTARY NOTES

19. KEY WORDS *(Continue on reverse side if necessary and identify by block number)*

Superconductivity
Far-infrared laser
Josephson effect
Point contacts
Microwave and far-infrared detection

20. ABSTRACT *(Continue on reverse side if necessary and identify by block number)*

We have studied the high-frequency behavior of niobium cat-whisker point contacts using radiation from an optically pumped far-infrared (FIR) laser. *is studied*

The FIR molecular laser had a dielectric-waveguide cavity and was pumped by a CO_2 laser. We have extended the use of capacitive-mesh output couplers throughout the FIR spectrum, between 42 μm and 1.2 mm, and have found the optimum grid constants for several lines. At shorter wavelengths, *is extended* *micrometers*

DD $_{1\ JAN\ 73}^{FORM}$ 1473 EDITION OF 1 NOV 65 IS OBSOLETE
S/N 0102-014-6601

78 07 12 006

20. Abstract continued

the laser performance was improved by the use of a novel hybrid capacitive-mesh hole output coupler.

We find the coupling of the FIR radiation to the point contact is found to depend in a simple manner on the resistance of the contact. The FIR laser radiation induces constant-voltage steps on the dc I-V curves of our junctions, allowing us to study the high-frequency ac Josephson effect.

When the point contacts are classified on the basis of their response to the FIR laser radiation, their dc I-V curves fall into recognizable groups. We find that the ac Josephson effect has a strong correlation with the gap-related structure on the I-V curve, but none at all with the apparent excess current observed in all the contacts. For high-performance junctions, these and other features of the I-V curves are very reproducible from contact to contact, allowing a comparison with the available theories. The experimental evidence seems to suggest that our point contacts are best modelled as extremely small metallic constrictions.

We have measured the power dependence of the current half-widths of the constant-voltage steps using FIR frequencies from 245 GHz to 2.52 THz (fundamental step voltages from ~ 0.2 to ~ 2 times the energy gap). We find that the shape of the power-dependence curves is fitted reasonably well by a voltage-bias version of a theory that includes the frequency-dependence of the Josephson effect. However, the magnitude of the observed steps is considerably smaller than predicted. Some of this discrepancy is caused by heating and noise effects. After corrections are made for these effects, our fundamental step data is used to obtain the FIR frequency dependence of the Josephson effect. Our data verifies the intrinsic roll off of the strength of the Josephson effect above the energy-gap frequency.

The high-quality junctions were tested as frequency-selective, incoherent FIR detectors, with the dc bias in the vicinity of the incipient laser step. The response was found to be linear in the laser power, and the best measured responsivity at 604 GHz was $\sim 2 \times 10^5$ V/W, while the best noise equivalent power was $\sim 10^{13}$ W/$\sqrt{Hz}$, with a 450 Hz chopping frequency. The NEP is limited by the voltage noise in the junction, which was found to have an approximately $1/f^2$ frequency dependence. The detector performance is degraded considerably at higher FIR frequencies. The shape of the laser-induced steps was used to measure the effective noise temperatures, which increase with bias voltage in agreement with a heating model of metallic constrictions. Also studied was the low-laser-power behavior of the I-V curves near the critical current, which may be of importance for mixing applications with external local oscillators.

A FAR-INFRARED LASER STUDY OF JOSEPHSON POINT CONTACTS

By

David Allan Weitz

Technical Report No. 14

May 1978

Division of Applied Sciences

Harvard University · Cambridge, Massachusetts

ABSTRACT

We have studied the high-frequency behavior of niobium cat-whisker point contacts using radiation from an optically pumped far-infrared (FIR) laser.

The FIR molecular laser had a dielectric-waveguide cavity and was pumped by a CO_2 laser. We have extended the use of capacitive-mesh output couplers throughout the FIR spectrum, between 42 μm and 1.2 mm, and have found the optimum grid constants for several lines. At shorter wavelengths, the laser performance was improved by the use of a novel hybrid capacitive-mesh hole output coupler.

We find the coupling of the FIR radiation to the point contact to depend in a simple manner on the resistance of the contact. The FIR laser radiation induces constant-voltage steps on the dc I-V curves of our junctions, allowing us to study the high-frequency ac Josephson effect.

When the point contacts are classified on the basis of their response to the FIR laser radiation, their dc I-V curves fall into recognizable groups. We find that the ac Josephson effect has a strong correlation with the gap-related structure on the I-V curve, but none at all with the apparent excess current observed in all the contacts. For high-performance junctions, these and other features of the I-V curves are very reproducible from contact to contact, allowing a comparison with the available theories. The

experimental evidence seems to suggest that our point contacts are best modelled as extremely small metallic constrictions.

We have measured the power dependence of the current half-widths of the constant-voltage steps using FIR frequencies from 245 GHz to 2.52 THz (fundamental step voltages from ~0.2 to ~2 times the energy gap). We find that the shape of the power-dependence curves is fitted reasonably well by a voltage-bias version of a theory that includes the frequency-dependence of the Josephson effect. However, the magnitude of the observed steps is considerably smaller than predicted. Some of this discrepancy is caused by heating and noise effects. After corrections are made for these effects, our fundamental step data is used to obtain the FIR frequency dependence of the Josephson effect. Our data verifies the intrinsic roll off of the strength of the Josephson effect above the energy-gap frequency.

The high-quality junctions were tested as frequency-selective, incoherent FIR detectors, with the dc bias in the vicinity of the incipient laser step. The response was found to be linear in the laser power, and the best measured responsivity at 604 GHz was $\sim 2 \times 10^5$ V/W, while the best noise equivalent power was $\sim 10^{-13}$ W/$\sqrt{\text{Hz}}$, with a 450 Hz chopping frequency. The NEP is limited by the voltage noise in the junction, which was found to have an approximately $1/f^2$ frequency dependence. The detector performance is degraded

considerably at higher FIR frequencies. The shape of the laser-induced steps was used to measure the effective noise temperatures, which increase with bias voltage in agreement with a heating model of metallic constrictions. Also studied was the low-laser-power behavior of the I-V curves near the critical current, which may be of importance for mixing applications with external local oscillators.

TABLE OF CONTENTS

vi

Table of Contents (Continued)

LIST OF FIGURES

List of Figures (Continued)

List of Figures (Continued)

LIST OF TABLES

CHAPTER I

INTRODUCTION

Since it was first predicted[1] in 1962, the Josephson
effect has aroused considerable interest, both for its fas-
cinating fundamental nature, and for the potential applica-
tions of Josephson-effect devices. One problem of particu-
lar interest has been the determination of both the intrinsic
fundamental limitations of the high-frequency behavior of
the Josephson effect and the practical limitations imposed
on devices by geometry, material, and other experimental
parameters. Josephson-effect devices can be loosely classed
into three broad categories: tunnel junctions, microbridges,
and point contacts. The high-frequency performance of
tunnel junctions is generally limited by shunt capacitance.
There have been recent advances in fabricating small-area,
low-capacitance, high-current-density tunnel junctions,[2]
but the high-frequency Josephson behavior of these has not
yet been reported. The major limitation in the high-frequency
performance of microbridges is Joule heating.[3] Even the
best quality variable-thickness bridges (VTB's),[4] whose
geometry optimizes the removal of the Joule heat, are still
limited at higher voltages by power dissipation because of
their characteristically low impedance. Point contacts, in

1

particular the niobium "cat-whisker" type, avoid both these problems. Because of their very small area, their capacitance can be extremely small,[5] and because of their higher impedance and favorable three-dimensional geometry, the effects of heating can be minimized.[6] In fact, cat-whisker point contacts have demonstrated the best high-frequency performance of all to date, showing direct evidence of the ac Josephson effect at ~ 8 THz (17 mV).[7] Thus they are the best device for study of the <u>intrinsic</u> limitations in the high-frequency behavior of the Josephson effect. In this report, we present the results of a detailed study of the high-frequency performance of niobium cat-whisker point contacts.

We study the Josephson effect by monitoring the constant-voltage steps induced on the dc I-V curves by laser radiation. The voltage, V, of the step is related to the nth harmonic of the laser frequency, nf_L, by the usual Josephson relation, $V = nhf_L/2e$. In practical units, the constant of proportionality is $2e/h = 483.6$ GHz/mV. The low-temperature energy-gap voltage, which is $2\Delta/e \approx 3.1$ mV for niobium, sets the voltage scale of interest. Thus the high-voltage region considered in this report is approximately 0.5-10 mV. The corresponding Josephson frequencies lie in the far-infrared (FIR) region of the spectrum, from ~ 250 GHz to over 5 THz.

The source of the required radiation was a molecular FIR laser, optically pumped by a CO_2 laser. It could be

operated on numerous wavelengths in the FIR, from 42 μm
(7.2 THz) to 1.22 mm (245 GHz). The output power on the
stronger lines was typically ~10 mW, with up to ~80 mW on
the strongest line. The output mode was nearly Gaussian,
so it could be well focused. Chapter II contains a detailed
description of the laser system.

The method used to fabricate the point contacts, and
the experimental apparatus used to test them are described
in Chapter III. Both the shape of the dc I-V curve and the
high-frequency performance of niobium cat-whisker point
contacts can vary considerably from junction to junction.
Chapter III also contains the results[8] of a systematic study
of the high-frequency behavior of contacts with various types
of dc characteristics. A strong correlation is found between
the high-frequency ac Josephson effect and certain features
on the dc I-V curves. In particular, we find that the
sharpness of the structure at the energy gap correlates
strongly with the existence of the ac Josephson effect at
high voltages. We test the junctions using two different
FIR frequencies, looking either for the fundamental Joseph-
son step induced by 119 μm (2.52 THz) laser radiation at
5.22 mV, or, for a finer voltage grid, the harmonics of the
1.25 mV step induced by 496 μm (604 GHz) radiation. Those
point contacts that perform well at high frequencies and
show a strong Josephson effect at high voltages are found
to be quite reproducible from junction to junction.[8] The

characteristic features of the I-V curves of these point contacts serve to identify the high-quality junctions without the need for a high-frequency test. Furthermore, this consistency and reproducibility has allowed us to study quantitatively the unique characteristics of this sort of junction.

In Chapter IV, we discuss the theoretical models that have been used to calculate dc I-V curves of Josephson-effect devices, and compare the calculations with our measurements. The comparison suggests some interesting details about the physical nature of the minute active region of the point contact. In order to interpret the remainder of our experimental data, we need to relate the behavior of the high-frequency Josephson effect to that of the constant-voltage steps induced on the dc I-V curves. The available theoretical models that do this are discussed in the latter part of Chapter IV.

Chapter V contains a detailed description of the measurement of the intrinsic FIR frequency dependence of the strength of the Josephson step. We have measured the power dependence of the current half-widths of the constant-voltage steps induced by six different laser frequencies. We find that these are remarkably reproducible from junction to junction,[9] showing that the high-quality point contacts are as consistent in their high-frequency behavior as they are in their dc I-V characteristics. We use the maximum current half-width of the fundamental laser-induced step normalized to the zero-

power critical current, I_1^{max}/I_c, as a measure of the strength
of the Josephson effect at the laser frequency.[10,11] The
measured value of I_1^{max}/I_c must be corrected for the effects
of noise rounding and heating, both of which are discussed
in Chapter V. The corrected values of I_1^{max}/I_c for a series
of laser frequencies give a measure of the intrinsic fre-
quency dependence of the Josephson effect.

Josephson cat-whisker point-contact devices have con-
siderable promise as detectors, mixers, and oscillators.
The extension of the operating range to FIR frequencies
introduces questions concerning their high-frequency per-
formance and the importance of additional noise resulting
from the higher levels of dissipated power. In an attempt
to investigate some of these questions, we have measured
the characteristic noise levels of our high-quality junctions,
both with and without incident FIR radiation. In Chapter VI,
we use the analysis of the noise rounding of Josephson
steps at high laser power levels to measure the effective
noise temperature as a function of bias voltage. We find
that it is consistent with heating-enhanced Johnson noise
but not with shot noise. In order to study their performance
as a frequency-selective, incoherent detector, we examine
the response of the junctions to low levels of FIR laser
radiation in the vicinity of the incipient first step. The
minimum detectable power in this case is limited by low-
frequency voltage fluctuations. We have measured the
spectral density of these fluctuations from ~10 Hz to ~30

kHz, and present the results in Chapter VI. We also note the peculiar behavior of the dc I-V curves near the critical current when our junctions are irradiated by low levels of laser radiation, which may be of importance in mixing applications with an external local oscillator. Chapter VI closes with a summary of the results obtained to date with Josephson point-contact mixer-receivers, and discusses their future potential as useful devices.

The major conclusions of this work are summarized in Chapter VII.

CHAPTER II

FAR-INFRARED LASER

2.1 Introduction

FIR laser action in an optically pumped molecular gas
was first reported by Chang and Bridges[12] in 1970. Improve-
ments and advances in the technology were rapid, and now
optically pumped lasers are an important and widely used
source of FIR radiation, with over 700 lines having been
reported.[13] This chapter describes in detail the laser
system used for these experiments.

The following section gives a very brief outline of the
theory of an optically pumped FIR laser. Section 2.3 con-
tains a description of the CO_2 pump laser, and the FIR
cavity is described in Section 2.4. An important component
of the FIR cavity is the capacitive-mesh output coupler,[14]
described in detail in Section 2.5. Finally, the typical
performance characteristics of the laser system are described
in Section 2.6.

2.2 Simple Theory

The basic principles of an optically pumped FIR laser
are quite simple. The pump radiation, usually supplied by
a CO_2 laser, is absorbed in the lasing molecule, raising it

7

to a particular rotational sublevel of an upper vibrational state that is otherwise essentially unpopulated within the Boltzman distribution in thermal equilibrium. Lasing action then occurs between the excited level and the next lower rotational sublevel within the pumped vibrational band. The resulting laser radiation is in the FIR region of the spectrum. The FIR laser transitions have a preferential polarization with respect to the pump. Thus a linearly polarized pump beam will result in an FIR beam polarized either parallel or perpendicular to the pump, depending on the particular lasing transition involved.

Optical pumping is a very efficient means of excitation. Because of the narrow bandwidth of the CO_2 laser, only a single rotational (J) sublevel is populated, unlike discharge lasers where there is no control over the upper levels that are excited. However, the narrow bandwidth of the pump also creates problems. It must lie within the absorption bandwidth of the lasing molecule, which limits the useful transitions to chance coincidences between the pump and absorbing transitions. Furthermore, since the absorption is highly frequency dependent, the CO_2 laser must be tuned within its Doppler-broadened gain bandwidth to maximize the FIR output intensity. This puts more stringent requirements on the CO_2 laser stability.

More detailed theories of the optically pumped FIR laser have been developed.[15-17] All rely on rate equations to give the qualitative dependences of the output power on

various parameters such as lasing gas pressure, pump frequency, and the pump absorption coefficient. However, considerable spectroscopic data on the lasing molecule is required for a detailed comparison to experiment. Thus only one molecule, CH_3F, for which enough spectroscopic data is available, has been treated in detail.[15] Good agreement is found between the theory and experiment for this case. None of these theories includes the effects of two-photon or Raman-type processes, which can also be important.[18]

For operation well above threshold, a simplified expression for the FIR output power is[19]

$$P_{FIR} \approx \left(\frac{1}{1 + \frac{g_2}{g_3}} \right) \left(\frac{h\nu_{FIR}}{h\nu_P} \right) \left(\frac{T}{T + A + \delta} \right) \left(\frac{\alpha}{\alpha + \beta_P} \right) P_P .$$

(2.1)

Here, P_{FIR} and P_P are respectively the FIR output power and pump power entering the cavity; ν_{FIR} and ν_P are the FIR and pump frequencies; g_2 and g_3 are the degeneracies of the upper and lower lasing sublevels; T is the fraction of the FIR power coupled out per pass; A is the single pass FIR cavity loss; δ is the excited state FIR absorption per pass; α is the fraction of the pump power absorbed in the lasing gas; and β_P is the fraction of the pump power lost due to absorption in the walls and mirrors of the FIR cavity.

The rotational sublevels involved in lasing generally have quite high J quantum numbers. Thus $g_2 \gtrsim g_3$, and the first term in Eq. (2.1) is always $\lesssim \frac{1}{2}$. This term reflects

the fact that the upper and lower lasing state lifetimes
are approximately equal and the laser is operating in a
saturated condition. For every two molecules excited
(assuming $g_2 = g_3$), one can contribute to the output power
by emitting an FIR photon and decaying to the lower state,
but this then destroys the population inversion necessary
for laser action. Thus, only $\sim \frac{1}{2}$ the excited molecules can
contribute to the output. The second term in Eq. (2.1) is
the familiar Manley-Rowe condition.[20] Since the laser action
is really an energy down-conversion process, the maximum
available output power is limited by the ratio of output to
input photon energies for the optimum case of one photon in
giving one out. The third term in Eq. (2.1) represents the
effect of the FIR losses due to either absorption in the
excited state (δ) or the cavity (A) compared to the fraction
lost to usable output power (T). The last bracketed term
in Eq. (2.1) represents the fraction of the pump power use-
fully absorbed in exciting the lasing gas.

The first two bracketed terms in Eq. (2.1) set the
theoretical upper limit to output power. It is useful to
define the conversion efficiency,

$$\eta = P_{FIR}/P_P \; .$$

(2.2)

Thus the maximum attainable conversion efficiency is

$$\eta_{max} = \left(\frac{1}{1 + g_2/g_3} \right) \left(\frac{h\nu_{FIR}}{h\nu_P} \right)$$

$$\approx \frac{1}{2} \left(\frac{h\nu_{FIR}}{h\nu_P} \right) \; .$$

(2.3)

Because the laser action is an energy down-conversion process, it is very inefficient, with $\eta_{max} \sim 5 \times 10^{-2}$ at an FIR wavelength λ_{FIR} of 100 μm, and $\eta_{max} \sim 5 \times 10^{-3}$ at $\lambda_{FIR} \approx 1$ mm. How closely the experimental η approaches η_{max} depends on the success in optimizing the other two terms of Eq. (2.1).

According to Eq. (2.1), the experimentally controllable parameters that reduce the conversion efficiency are the FIR losses due to A and δ and the pump losses due to β_P. The detrimental effects of the FIR losses can be kept quite small. A well designed FIR cavity can keep A to just a few percent, while allowing a reasonably high fraction of the power to be coupled out, thereby increasing T. The excited state absorption is pressure dependent, and thus can be kept small by using low pressures. It is the last bracketed term in Eq. (2.1) that is the most difficult to optimize. For most gases used, α is quite small, with the typical absorption coefficients in the range of 0.1-0.01 m^{-1} at the working pressures.[21] It is thus essential to have good coupling of the pump radiation to the FIR cavity mode to minimize β_P. Even so, the combination of relatively high cavity pump losses and low pump absorption is the major cause of the poor η obtained experimentally.

The pump absorption can be increased by raising the pressure of the lasing gas. However, besides increasing δ, a higher pressure also increases the rotational cross-relaxation rate γ_R, due to collisions. This is the rate at which the excited atoms are thermalized among all the J

sublevels of the upper vibrational band. The thermalization occurs rapidly because of the small energy differences between the J levels compared to $k_B T$. For example, at room temperature and for $\lambda_{FIR} = 500$ μm, $h\nu_{FIR}/k_B T \sim 0.1$. The collisions cause nonradiative transitions out of the upper lasing state, and the resulting thermalization creates a Boltzman-like distribution of states in the upper vibrational band, destroying the population inversion. This effectively limits the operating pressure to ~ 0.1 mTorr.

Another major limitation of the efficiency of these FIR lasers is the relatively slow vibrational relaxation rate, γ_V, of the excited vibrational band compared to the rotational cross-relaxation rate, γ_R, within the band ($\gamma_R \gg \gamma_V$). This creates a bottleneck for removing molecules from the lower laser level, and increases the thermalization within the excited vibrational state due to rotational cross-relaxation. Furthermore, $(\gamma_V)^{-1}$ is the effective lower-laser-state lifetime, and, for operation well above threshold, a decrease in this lifetime would increase the output power. Thus techniques to increase γ_V can lead to higher operating pressures and therefore to higher output powers. One such technique is to reduce the diameter of the FIR cavity,[22,23] to decrease the molecular diffusion time to the walls. A collision with the cavity wall will effectively relax a molecule from the excited vibrational state. This technique is successful with some, but not all, laser gases.[24] The addition of

an appropriate buffer gas to collisionally de-excite the
pumped molecules will also increase γ_V.[25] This method has
been quite successful with CH_3F, using C_6H_{14} as a buffer gas.

Despite recent improvements, the experimentally achieved
η remain quite low. Using the best systems designed to date,
the strongest FIR lines have typical experimental η of only
~ 10% of η_{max}.[26] The weaker lines have considerably lower η.
Thus there is still room for improvement, although the over-
all efficiency will always be low.

2.3 CO_2 Laser

The pump power was supplied by a modified commercial
CO_2 laser.[27] It had a 12-mm-dia., 1.8-m-long cavity, whose
active region was enclosed by two ZnSe Brewster-angle windows.
It was tuned to a single CO_2 transition by a 75 lines/mm
grating, which served as one end mirror. The other end mir-
ror, which was a semi-transparent output coupler, had a 20 m
radius of curvature and was mounted on a PZT stack for fine
frequency tuning of the output within the Doppler-broadened
CO_2 gain bandwidth. The relatively large radius of curvature
of the output coupler helped to reduce the divergence of
the output beam[28] and to improve the selectivity of the grat-
ing. The laser cavity was mounted on a granite base and
enclosed by a metal cover to improve the thermal stability.

The very large gain of the CO_2 laser could create problems
by allowing lines to lase even if their cavity mode required
a reflection on the side wall of the laser tube. This

caused two or even three adjacent CO_2 lines to lase at the same time, and the output mode did not have the Gaussian-like shape required for good focusing. These problems were corrected by the use of an output coupler with a lower reflectivity,[29] which decreased the optical feedback and made the off-center lines less likely to lase. Output coup-lers with reflectivities of 36% and 65% were used for the stronger and weaker CO_2 lines respectively. With careful adjustment of the alignment, a nearly Gaussian output beam containing only the required laser line could be obtained over most of the PZT scan. Single-line output powers were typically $\sim$ 12-25 W in the 9.5 μm bands and $\sim$ 20-50 W in the 10.5 μm bands.

In order to maintain a good output mode shape, it was essential that the Brewster-angle windows be kept clean. Small amounts of dirt on the surface would cause the laser to operate in higher-order modes. In particular, a thin film was found to be deposited on the inner surface of the windows while the laser was in operation. This built up slowly in time, causing both the power and mode structure to deteriorate. The problems were avoided by ultrasonic cleaning of the Brewster-angle windows in a soap and water bath after every $\sim$ 100 hours of CO_2 laser operation.

2.4 Far-Infrared Cavity

The most efficient FIR laser performance obtained to

date has been with relatively large-diameter, highly over-moded dielectric-waveguide cavities.[26] A Gaussian CO_2 pump beam can be coupled in with large f-number ($\sim$ f/50-f/200) optics through a central coupling hole in one mirror. It will couple to the FIR cavity very efficiently,[21] and will undergo one or more round trips before interacting with the walls. Furthermore, even the relatively large (2-4 mm-dia.) coupling hole required for the high f-number focusing optics gives only small FIR losses ($\lesssim$ 1%). Increasing the number of CO_2 pump-beam passes increases α; decreasing the inter-action of the pump beam with the cavity walls decreases β_p. The net result is an improved conversion efficiency.

The FIR properties of the cavity are also excellent. Because it is so highly overmoded (2r $\gg \lambda_{FIR}$, where r is the cavity radius), the FIR propagation losses are quite small.[30] The EH_{11} mode has the lowest losses and is linearly polarized and nearly Gaussian in shape. This mode can be efficiently excited by the linearly-polarized, Gaussian pump beam. It also transforms efficiently into the TEM_{00} Gaussian free-space mode so that the mirrors can be external to the wave-guide without incurring large losses.[31] This simplifies the design and operation of the laser cavity. Finally, the out-put mode shape[32] is nearly Gaussian for good focusing and is linearly polarized for efficient coupling to a polarization-sensitive detector.

The laser system is shown schematically in Fig. 2.1.
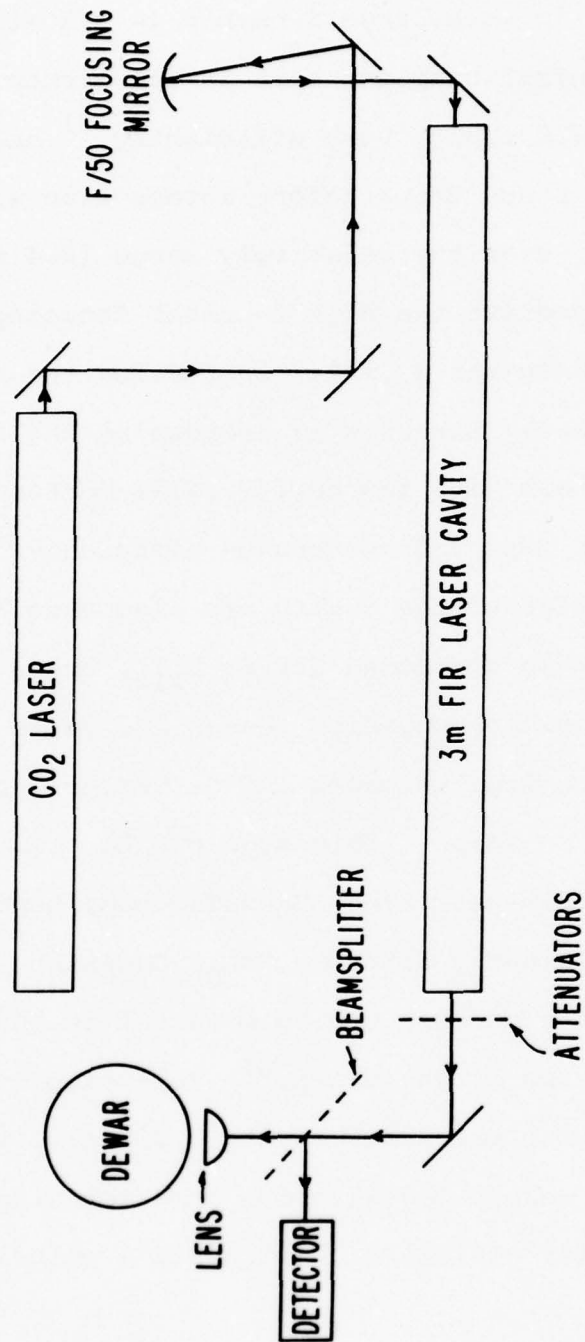
Fig. 2.1   Schematic of the experimental set up.

The FIR cavity was a 38-mm-dia., 3-m-long Pyrex industrial
pipe with two flat end mirrors. Using an $\sim$ f/50 focusing
mirror, the CO_2 beam was injected into the cavity through
a BaF_2 vacuum window and a 3-mm-dia. central coupling hole
in the back mirror. This mirror was mounted on a differential-
micrometer-driven translation stage with two bellows vacuum
seals to the cavity. This allowed the cavity length to be
tuned, which was necessary because the frequency separation
of the cavity modes is larger than the gain bandwidths of
the FIR laser lines. The second mirror served as both the
output coupler and a vacuum window. The laser was always
operated in the sealed-off mode and was pumped with a dif-
fusion pump to attain the required vacuum.

The FIR output beam was monitored by a thermal detector[33]
fed by a beamsplitter. At longer wavelengths ($\lambda > 300$ μm)
various thicknesses of plexiglass were used as attenuators
to vary the intensity, while different thicknesses of mylar
served the same purpose at shorter wavelengths. The polari-
zation of the output beam could be rotated 90° by rotating
that of the pump beam with a polarization flipper.[34]

2.5 Capacitive-Mesh Output Coupler

In order to take full advantage of the favorable charac-
teristics of the FIR cavity, it is important to use a well
designed output coupling mirror, a component which has
received much attention recently. This mirror should have
high reflectivity at the pump wavelength, λ_p, partial

reflectivity and low absorptivity at the FIR wavelength, λ_{FIR}, and should couple out over a broad area of the laser mode to limit diffraction. Among the schemes that have been used to meet these requirements are: a) hybrid metal mesh dielectric (MMD) mirrors,[35,36] b) hybrid metal dielectric hole (MDH) couplers,[21,26] c) etalons,[26,36,37] and d) capacitive-mesh couplers.[38] We have extended the use of capacitive-mesh couplers throughout the FIR spectrum, and have used a novel hybrid capacitive-mesh hole coupler for improved performance at shorter FIR wavelengths.

We have chosen to use capacitive-mesh couplers because of the relative simplicity and low cost of their fabrication compared to the other schemes. Unlike etalons, the substrate thickness does not have to be finely adjusted; unlike MMD couplers, their fabrication does not require photolithographic masking techniques; and unlike MMD and MDH couplers, they do not require a dielectric reflection coating for the pump radiation. The capacitive mesh itself meets the reflectivity requirements at both the pump and the FIR wavelengths. The mesh period, g, [see Fig. 2.2(a)] is comparable to λ_{FIR} for partial FIR transmission,[39] but is much greater than λ_p for reasonably high reflectivity of the 10-μm-pump radiation. The high reflectivity at λ_p allows the use of a crystal-quartz substrate which is strongly absorbing at 10 μm, eliminating the necessity of filtering any remaining pump power from the output. It also removes the need for a dielectric

	g(μm)	2a(μm)
A	34	8
B	51	14
C	76	21
D	102	19
E	127	15
F	212	36
G	254	27
H	318	25
I	508	55
J	564	33
K	847	60
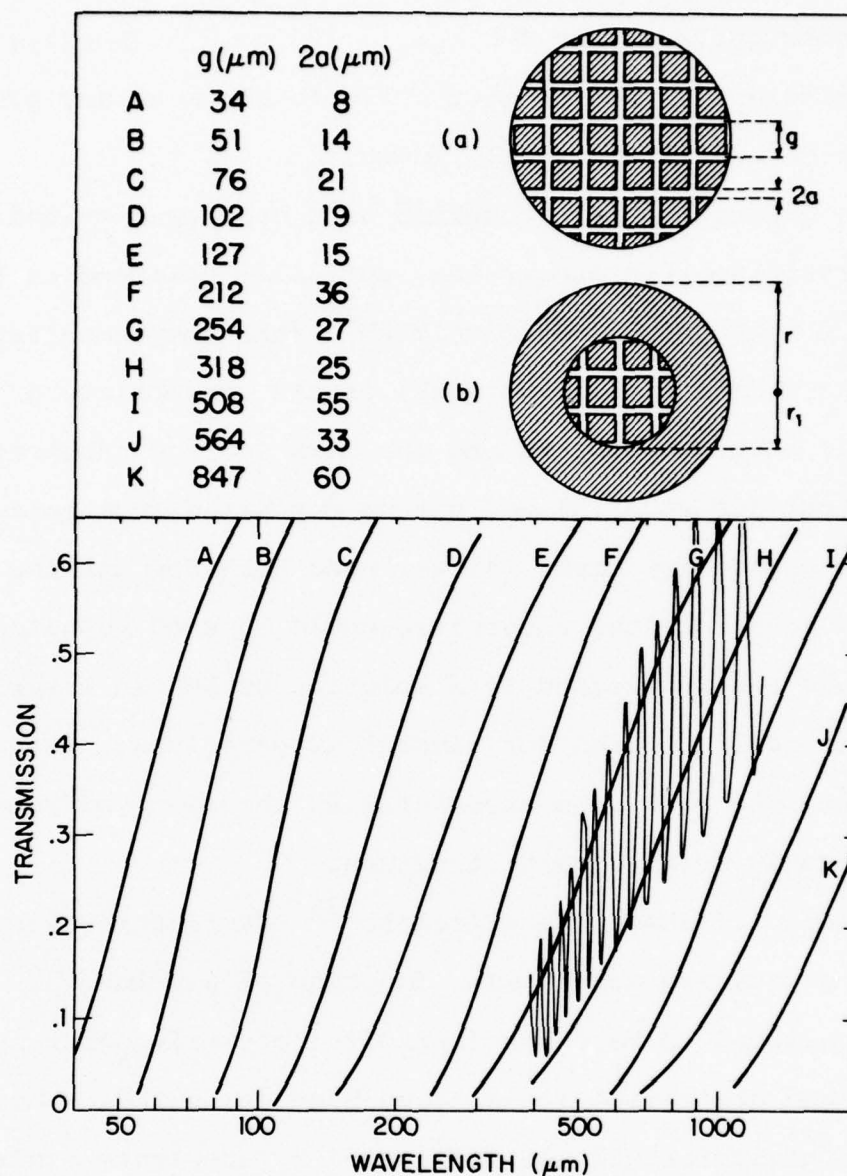
Fig. 2.2   Calculated transmission of capacitive meshes on crystal quartz as a function of wavelength. The thin line shows the etalon effects for mesh #G on a 2-mm-thick quartz substrate. The inset on the upper right shows schematically (a) a capacitive-mesh output coupler and (b) a hybrid capacitive-mesh hole coupler.

coating, reducing the FIR absorption losses which can other-
wise become quite severe for $\lambda_{FIR} \lesssim 100 \ \mu m$.[21] Finally, by
using different values of g, the FIR feedback at any given
λ_{FIR} can be relatively finely tuned.

The capacitive-mesh couplers were made on 2-mm-thick,
z-cut crystal-quartz substrates, optically polished on both
sides. A horizontal inductive mesh[40] (the complementary
structure to the capacitive mesh) of the appropriate g
served as both the support and the mask for the substrate
while about 300 nm of Al was vacuum deposited from below to
form the capacitive mesh. Al was used both for its low cost
and good adhesion; the substrates could be used repeatedly
(they were easily cleaned in a solution of KOH in water) and
the masks could be used for several evaporations. Attempts
to use Au were much less successful as shadowing effects
led to poorly defined mesh structure.

Figure 2.2 shows the calculated[39] FIR transmission of
various capacitive meshes as a function of wavelength. The
mesh is assumed to be on an (infinite) crystal-quartz sub-
strate, and absorption losses have been neglected. The
exact transmission will be influenced by substrate etalon
effects[38] as shown by the thin line in Fig. 2.2, which is
the calculated transmission of mesh #G on a 2-mm-thick quartz
substrate. In those cases where the thickness of the sub-
strate is known to sufficient accuracy, the calculated trans-
missions are in good agreement with those measured experi-
mentally. For example, at 496 μm, the measured transmission

of the substrate and mesh with g = 318 μm was ~ 10%, while the calculated value was ~ 7%. On the same substrate, a mesh with g = 254 μm had a measured transmission of ~ 25% compared to the calculated value of ~ 24%. The use of a plot similar to Fig. 2.2, and which included all the available electroformed meshes[40] suitable for masks was helpful as a guide in the initial determination of appropriate g and 2a for a given λ_{FIR}. If more than one mesh giving the required transmission was available, g/2a was chosen to maximize the area covered by metal, to improve the λ_p reflectivity. Because they were so simple to fabricate, a number of different mirrors could easily be tested to determine experimentally the optimum mesh constants.

We have used capacitive-mesh couplers throughout the FIR spectrum, from 42 μm to 1.2 mm. Table 2.1 lists the laser lines we have tried with the mesh constants that have worked at those wavelengths. When several different meshes were used for the same line, the values of g and 2a for the output coupler that gave the best performance are underlined. Optimizing the FIR transmission within the range of ~(5-50)% can increase the output power by ~(20-50)%. For example, changing g from 318 μm to 254 μm increased the 496-μm-output power by ~ 25%. The stronger lines (e.g., 119 μm) will lase even when they are severely under- or over-coupled, but the output power is decreased by more than an order of magnitude. This list is not meant to show all of the

Table 2.1

Mesh Constants For FIR Wavelengths

$\lambda_{FIR}[\mu m]$	Gas	Pump Line	g(2a)[μm]	(Best values underlined)
41.7	CH_3OH	9P(32)	34(7.6).[a]	
70.5	CH_3OH	9P(34)	34(7.6);[b]	51(14).[c]
118.8	CH_3OH	9P(36)	34(7.6);	51(14); 76(21); 318(25).
148.5	CH_3NH_2	9P(24)	76(21);	254(27).
170.6	CH_3OH	9P(36)	76(21);	318(25).
202.4	CH_3OH	9P(36)	76(21).	
233.9	N_2H_4	10R(8)	212(36);	254(27).
415	CH_2CF_2	10P(14)	847(60).	
496.1	$C^{12}H_3F$	9P(20)	254(27);	318(25)
554.4	CH_2CF_2	10P(14)	847(60).	
890.0	CH_2CF_2	10P(22)	847(60).	
1221.8	$C^{13}H_3F$	9P(32)	564(33);	847(60).

a)   Hybrid -- r_1 = 3 mm

b)   Hybrid -- r_1 = 8 mm

c)   Hybrid -- r_1 = 10 mm

unoptimized values of g which will work for each line. The highest FIR output power is obtained with the laser operating in the EH_{11} mode.[32] Using the optimized mesh constants, we obtain typical output powers of $\sim$ 10 mW at 496 μm and $\sim$ 80 mW at 119 μm, with $\sim$ 17-20 W pump power. With a 1.2-m-long cavity we obtain at least 6 mW at 1.22 mm, using $\sim$ 12 W pump power.[41]

We have made some preliminary comparisons with MDH couplers at a number of λ_{FIR}, and find that the total output power seems to be approximately the same (to within $\sim$ 50%). However, changing the grid constants of the capacitive-mesh couplers gave finer control of the reflectivity over the central portion of the coupler and allowed better optimization and improved performance for some λ_{FIR}. Of course, the diffractive divergence of the output beam is reduced with the capacitive-mesh couplers.

For λ_{FIR} < 100 μm, it was necessary to use a hybrid capacitive-mesh hole coupler to obtain good laser performance. A second evaporation produced a ring-shaped Al mirror and left a center hole, of radius r_1, covered only with the appropriate capacitive mesh, as shown schematically in Fig. 2.2(b). This not only increased the FIR feedback, but also considerably improved the CO_2 reflectivity, which drops off substantially for the mesh constants necessary for these λ_{FIR}. At 70.5 μm, the best performance was obtained with r_1 = 10 mm (compared to r = 19 mm for the waveguide cavity) and a mesh with g = 51 μm. Figure 2.3 shows a spatial scan across the
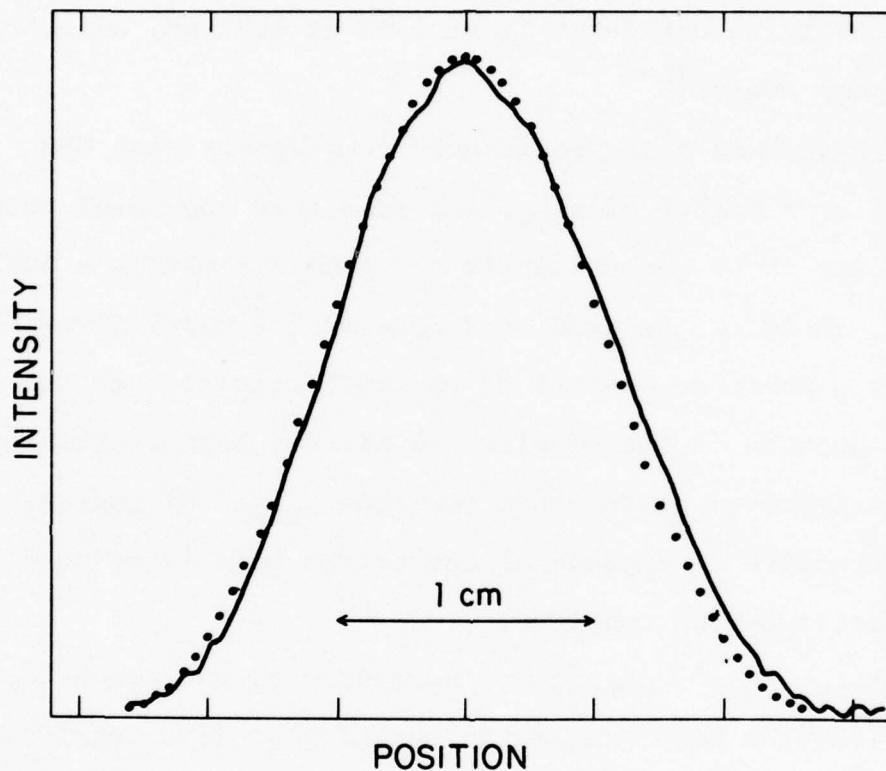
Fig. 2.3   Scan across the output of the strongest
mode at 70.5 μm, using a 20-mm-dia. hybrid capacitive-
mesh hole output coupler with g = 51 μm. The detec-
tor had an aperture of 1 mm and was 3.17 m away from
the laser. The dots are the calculated far-field
pattern from Eq. (2.4) in the text, and are scaled only
to the peak intensity.

output beam of the mode with the highest output power, the EH_{11} mode. The far-field intensity of the EH_{11} mode, coupled out through a hole with $r_1 < r$ can be shown to be

$$I \propto \left\{ \frac{1}{A^2 - (Br_1)^2} \left[AJ_1(A)J_0(Br_1) - Br_1 J_0(A)J_1(Br_1) \right] \right\}^2$$

(2.4)

with $A = u_{01}r_1/r$ and $B = 2\pi\sin\theta/\lambda$. J_0 and J_1 are the first and second Bessel functions, u_{01} is the first zero of J_0 and θ is the angular displacement. The solid dots in Fig. 2.2, the calculated far-field intensities using Eq. (2.4), are in excellent agreement with the data. Equation (2.4) can also be used to calculate the half-angle divergence at the e^{-2} point,

$$\theta_c = f(r_1/r)\lambda/r_1 ,$$

(2.5)

where $f(r_1/r)$ must be evaluated. The two limiting values of f, for a given r_1, are: $f(r \gg r_1) \approx 0.24$, in which case the intensity across the hole is uniform and the divergence is minimized, and $f(r = r_1) \approx 0.54$, in which case the intensity is peaked in the center and the divergence is maximized. In our case, $f(r_1/r = 0.52) \approx 0.43$, so that for $\lambda_{FIR} = 70.5$ μm, the predicted θ_c is 3.0 mr, which is exactly what is measured experimentally.

The mirror quality of the capacitive mesh at λ_p is limited both by diffraction and absorption because the surface is not completely covered with metal. Both of these

problems become less severe as g increases. For example, we measure the specular reflection of the capacitive-mesh coupler with g = 254 μm to be $\sim$ 85% at λ_p. For very small g, the reflectivity at λ_p is improved by the addition of the Al ring. The amount of CO_2 radiation that leaks through the mesh to be absorbed in the quartz substrate sets a limit on the maximum pump power that can be used without breaking the mirror. However, we have had no breakage problems using $\sim$ 15-20 W pump power at the shorter λ_{FIR} (small g) and over 50 W at the longer λ_{FIR} (large g).

2.6 Performance

There are many parameters which must be individually optimized to obtain the best performance from the FIR laser system. Once the CO_2 laser output was optimized, the most important adjustment was found to be the alignment of the pump-beam injection optics, and a simple technique was developed to do this. Using a removable mirror, a HeNe line-up laser beam could be placed in the path of the CO_2 beam. The injection optics were then adjusted so that the line-up laser beam was aligned along the optic axis of the FIR cavity. The axis was defined by the central input coupling hole at one end and a centered diaphragm at the other. This procedure was possible because the FIR output coupler partially trans-mitted the HeNe beam. When the injection optics were properly adjusted, the transmitted HeNe beam, which was diffracted by the mesh, could be used to align the FIR cavity. If the

cavity was misaligned, the transmitted beam looked like a number of overlapping diffraction patterns. When the mirrors were adjusted to align the cavity, only a single diffraction pattern was observed. Using this line-up technique, some laser output was always obtained, and final adjustments could then be made while monitoring the output power.

These experiments required reasonably good amplitude stability of the output. The most critical variable in controlling the stability is the exact frequency of the pump, which is tuned by the PZT-stack translation of the CO_2 output coupler. Figure 2.4 shows the FIR output power as the voltage to the PZT stack is varied, while the laser is operating on the 496 μm line of CH_3F. The exact shape of the output power dependence changes considerably for small changes in the alignment, as shown by the two separate plots. These were made with slightly different adjustments of the injection optics. Each pattern shows two output peaks because the travel range of the PZT traverses two CO_2 cavity modes. The slight differences between the peaks of each mode are caused by the slightly different alignment of the CO_2 cavity at each end of the PZT stack's travel. Figure 2.4 shows that a small change in CO_2 pump frequency can cause a large change in the FIR output power.

Stable FIR output power can be maintained if there is a flat peak in the curves of the type shown in Fig. 2.4. In that case, small changes in the CO_2 pump frequency will not
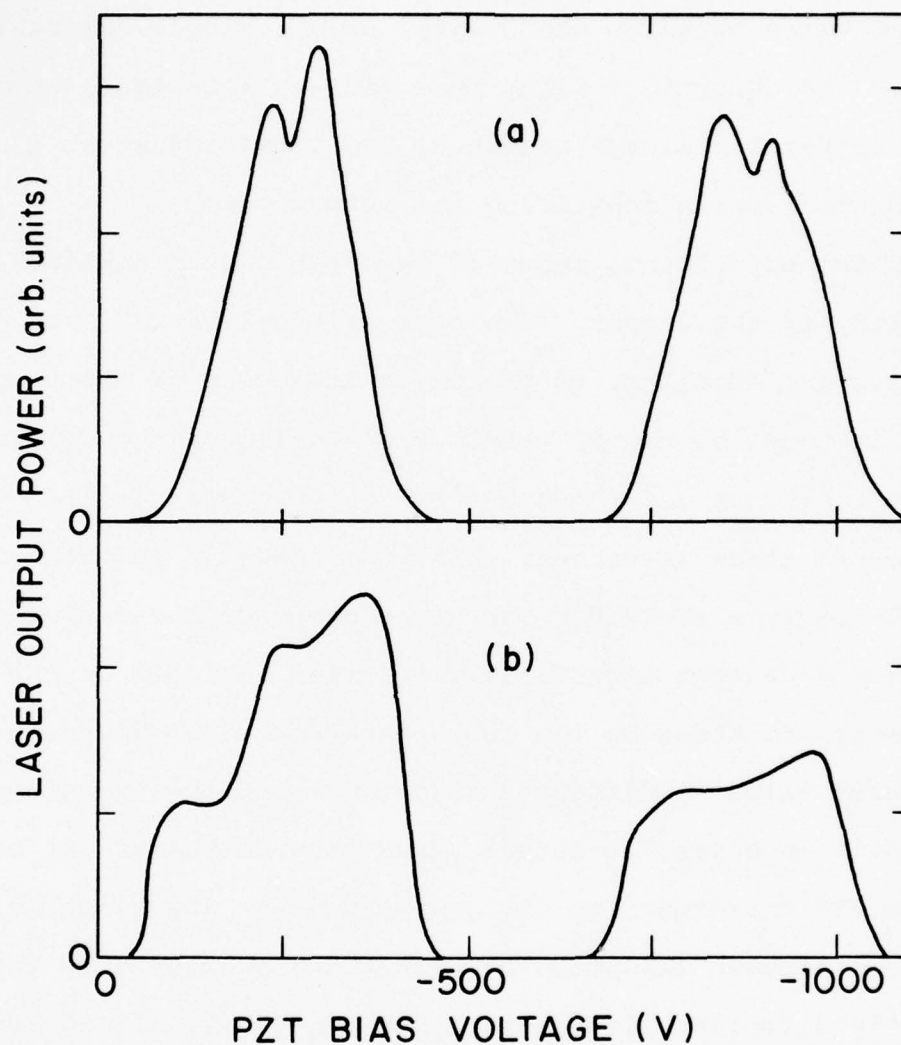
Fig. 2.4   Output power of the 496 μm laser as a
function of CO_2 PZT bias voltage for two slightly
different alignments of the injection optics, (a)
and (b).   The PZT traverses two CO_2 cavity modes
giving the double-peaked structures.   The flattened
peak in (b) will give more stable FIR output.

cause large FIR amplitude fluctuations. The exact dependence of the output power on pump frequency is quite sensitive to alignment, and must be optimized by trial and error. Figure 2.4(b) shows a good adjustment, with a reasonably flat portion on the peak of the curve.

The output power is also dependent on the separation of the FIR cavity mirrors, which defines the cavity frequency. Figure 2.5 shows the output power as the translatable mirror is scanned. The inset shows a large mirror movement. Two different laser modes are operating, and the separation between consecutive peaks of the same mode is $\lambda_{FIR}/2$ or ~ 250 μm. The detailed mode structure is shown on a larger scale in the lower portion of Fig. 2.5. The scan shows that a change in the cavity length of a few microns ($\sim 10^{-6}$ of the total length) can cause substantial variation in the output power. An interesting feature of the scan in Fig. 2.5 are the dips in power that seem to occur with an ~ 5 μm periodicity. This sort of behavior has been seen by others,[35] but has not been fully explained. The 5 μm periodicity suggests that it may be due to some sort of standing wave pattern of the pump radiation, although why this would cause a dip in the FIR output power is not clear.

The long term ($\sim$ minutes) drift in the laser output is caused by FIR-cavity-length variations which must be relatively large to have an effect. Short term ($\sim$ seconds) fluctuations are caused by CO_2-cavity-length variations which are much
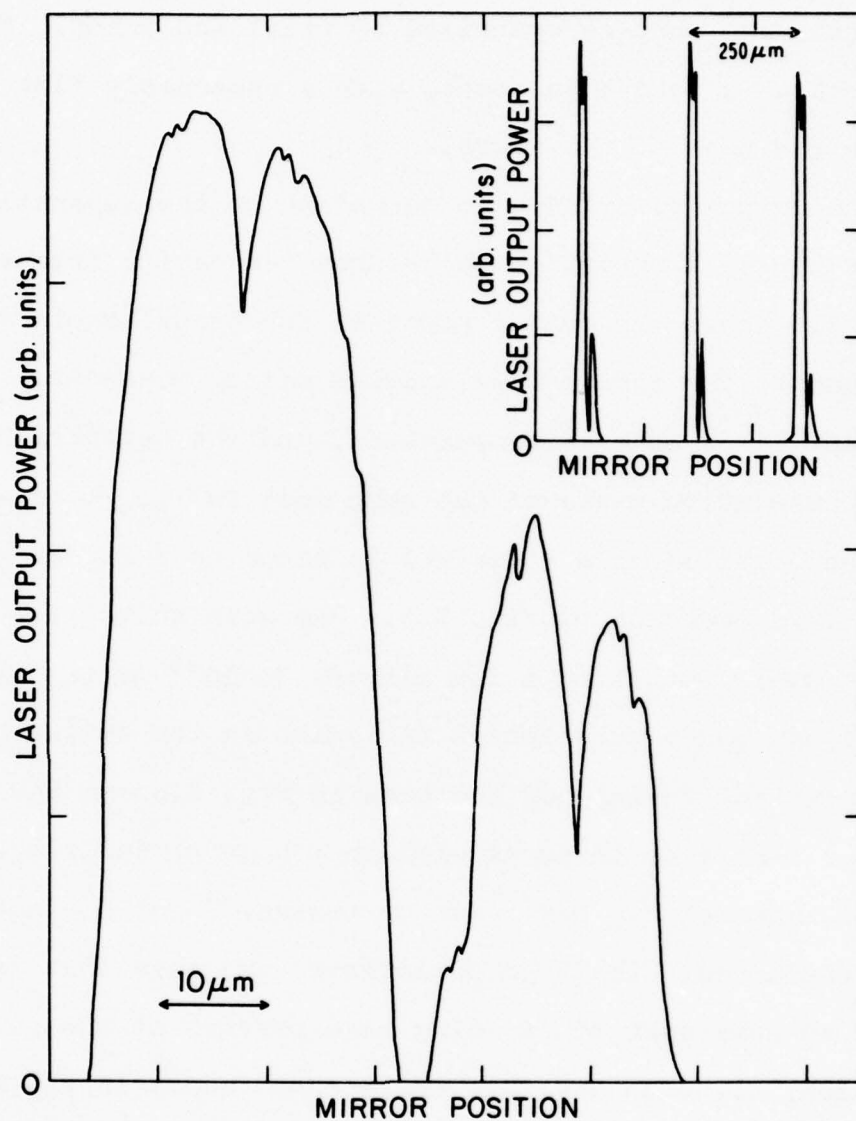
Fig. 2.5   FIR cavity scans for the 496 μm line of
CH$_3$F. The inset shows two modes lasing, with a
repeat distance for each mode of ~250 μm. The
lower figure shows the two modes in detail.

smaller absolute changes. Temperature variations are the major cause of these cavity-length changes. It is thus quite important to maintain a constant temperature in the laser room. This is shown dramatically by Fig. 2.6, which shows the increase in short-term amplitude fluctuations that results from opening a window. This curve was taken during the summer, so there was no major temperature change, only a light breeze blowing through the window. Nevertheless, this had a major effect.

The most stable performance was obtained if the CO_2 laser was allowed to warm up for at least three hours and the room temperature was maintained at a constant and somewhat elevated level ($\sim 80^{\circ}$F). Figure 2.7 shows a running scan of the output power over ~ 30 min. Long term drift was only $\sim 10\%$, while short term fluctuations, measured with a 300 msec time constant, were $\lesssim 2\%$. Thus good free-running stability can be obtained without the use of an active stabilization scheme.

Finally, it is interesting to compare the experimentally achieved conversion efficiencies with the theoretical maxima. At 119 μm, we estimate that we obtained ~ 80 mW, with ~ 15 W pump actually coupled into the cavity. This gives $\eta \approx 5 \times 10^{-3}$, which is about 11% of η_{max}. Similarly, the ~ 10 mW at 496 μm gives $\eta \approx 7 \times 10^{-4}$, or about 7% of η_{max}; and ~ 6mW at 1.22 mm with ~ 12 W pump gives $\eta \approx 5 \times 10^{-4}$, or about 10% of η_{max}. These values are comparable to the best performance reported[26] with optically pumped FIR lasers.
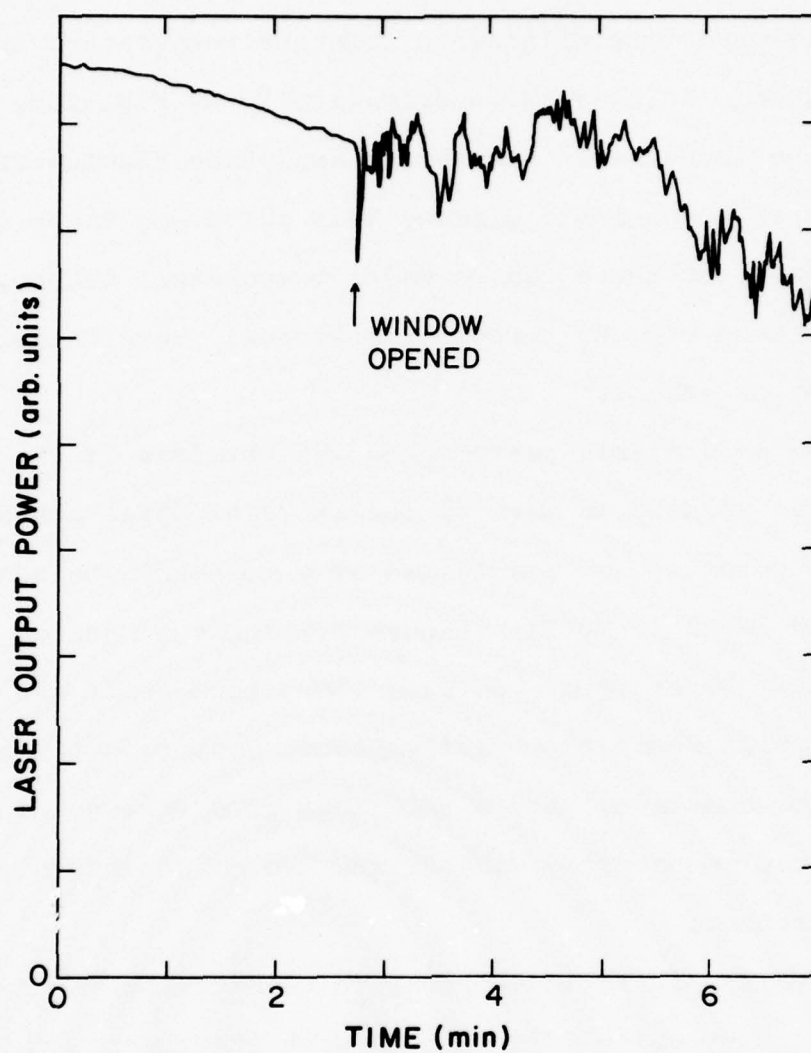
Fig. 2.6   Laser stability before and after a room
window is opened.
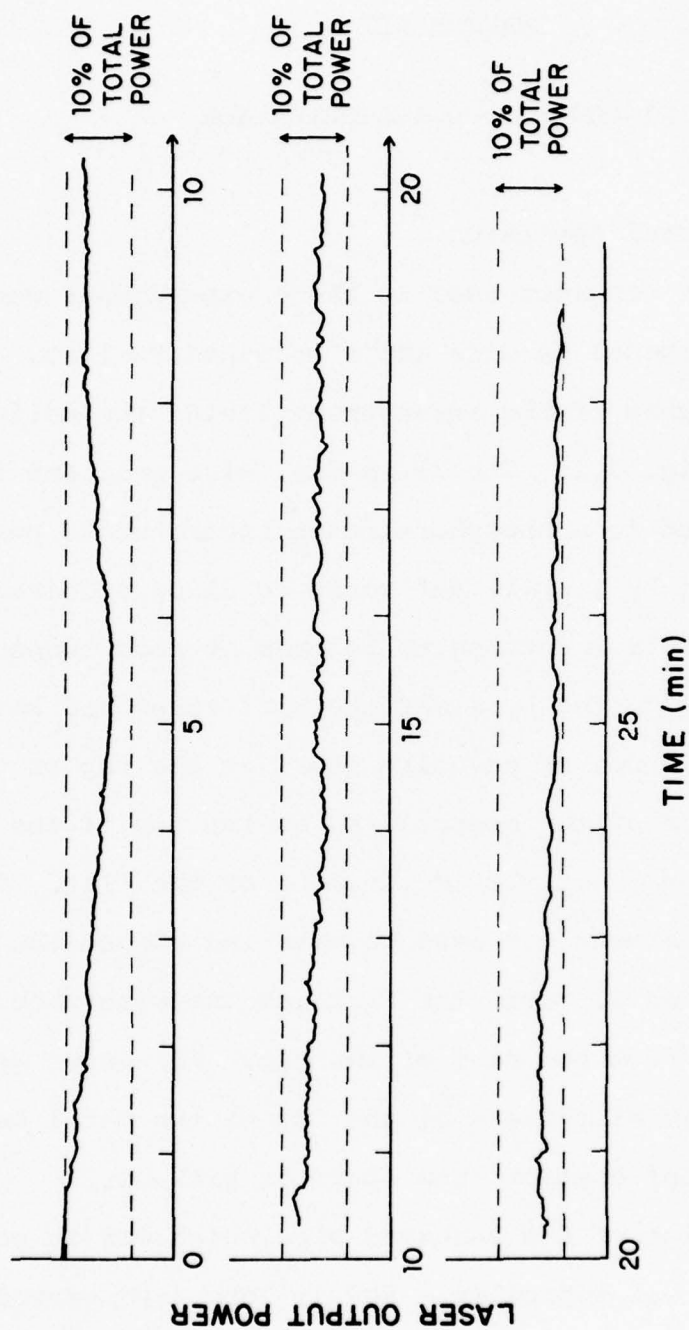
Fig. 2.7 A running scan of the amplitude of the 496 μm line of CH_3F, showing the excellent long- and short-term stability.

CHAPTER III

POINT-CONTACT CHARACTERIZATION

3.1 Experimental Apparatus

The point contacts used in these experiments were formed
between a sharpened Nb wire and a polished Nb flat. A
schematic diagram of the arrangement inside the helium Dewar
is shown in Fig. 3.1. The 75-μm-dia. wire was bent in a L
shape and glued to a phosphor-bronze spring whose position
could be fixed by a small set screw to allow a coarse adjust-
ment of the contact setting to be made at room temperature.
The flat was adjusted by a differential screw and lever sys-
tem driven by a set of reducing gears at the top of the rig.
A complete turn of the control rod at the top of the Dewar
corresponded to about 0.6 μm movement of the flat. This
very fine adjustment was used to make and adjust the point
contact while cold. Both the flat and the wire were electric-
ally isolated from the rest of the rig. All leads were
brought through rf filters at the top of the metal Dewar to
shield the point contact from spurious pick-up.

The portion of the L-shaped wire which was in contact
with the flat was typically ~ 500 μm long, and served as an
antenna to couple the laser radiation into the junction.[42]
The whole lower structure of the Dewar insert could be

34
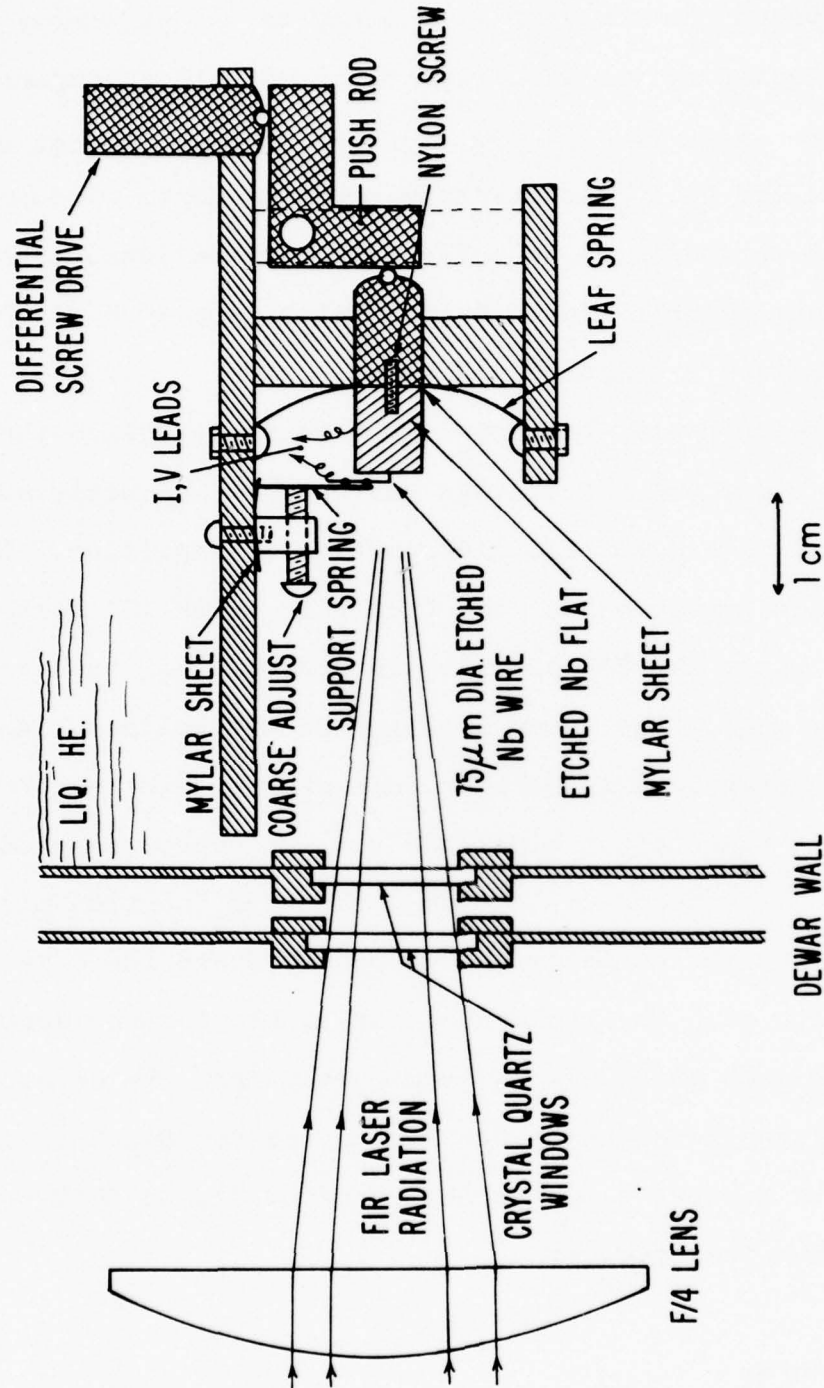
Fig. 3.1 Schematic of Dewar insert showing the point-contact arrangement.

rotated to change the angle between the antenna and the laser beam to improve the coupling efficiency to the antenna. The laser radiation was linearly polarized with a component of its $\vec{E}$ vector along the antenna, and was focused through room-temperature and helium-temperature crystal-quartz windows in the side of the Dewar by an $\sim$ f/4 polyethylene lens. The cooled crystal-quartz window helped filter out much of the room-temperature background radiation.

A high-impedance, battery-driven source supplied the dc current bias, and the voltage was measured directly across the junction with a PAR 113 differential preamplifier. Low-level voltage measurements were made with a PAR 124 lock-in amplifier, using the PAR 116 plug-in preamplifier in its transformer mode. The power spectrum of the voltage fluctuations was measured using the ac voltmeter mode of the PAR 124 with its tuned input amplifier set for narrow bandwidth ($Q = 100$). The frequency-dependent transfer function of the filter-transformer combination was measured and the data were corrected for it. The background noise, as measured across a 100 Ω resistor at 4.2 K, was subtracted from the data. This background noise was $\sim$ 0.8 nV/$\sqrt{\text{Hz}}$ at 450 Hz, but was considerably higher at odd harmonics of 60 Hz, so that we avoided these frequencies.

3.2   Procedure

The method of preparation of the point contacts was

found to be quite critical in obtaining I-V curves that had high I_cR products and showed strong Josephson effects at high frequencies. The Nb wire was sharpened with standard electroetching techniques[43] using about 4-6 V dc in a 5:4:1 solution of HNO_3, HF, and CH_3COOH. The radius of curvature of the points used was always less than ~ 1 μm as observed with an optical microscope. The flat was polished to an optical finish using 0.3 μm Alumina powder on a wax lap, and was etched slightly with HF, then rinsed with CH_3OH. Both sides of the junction were exposed to atmosphere for as short a time as possible after the final etching, to produce as "clean" a point contact as possible.

Contact was always made in liquid He. The position of the flat was first adjusted to make a very high-resistance, wholly Ohmic contact, then the resistance was lowered and the desired I-V curve produced with a "burn-in"[44] process using about 2 V_{P-P} at 35 Hz. During the course of a run, it was possible to make a wide variety of I-V curves using a combination of mechanical adjustment and burn-in. The adjustment became more difficult and the I-V curves were more likely to be hysteretic as the run progressed and the point became blunted. The blunting was visible with an optical microscope following the run if the point had undergone numerous adjustments.

Some sort of mechanical "scratching" seemed to be necessary in order to break through the surface oxide and produce

high-quality, high-$I_c R$ point contacts. Attempts to make high-quality junctions with different diameter wires were less successful: thinner, 50-μm-dia. wire seemed too pliable and appeared to bend back when pushed by the flat, making it extremely difficult to produce high-quality point contacts; thicker, 175 μm-dia. wire had no give at all and became blunted too easily. However, using the 75 μm-dia. wire, it was usually possible during the course of a run to make a number of high-quality junctions that remained stable for as long as was necessary to do the experiments.

3.3 Coupling

One measure of the coupling of the radiation to the point contact is the laser power required to produce the maximum current-width of the first step, which ought to occur at a particular value of the induced ac voltage, independent of the junction resistance. The lower part of Fig. 3.2 is a plot of the square root of the required 496-μm-laser power as a function of junction resistance. The large rise at low R suggests that the low-resistance junctions are effectively current-biased. This is borne out by the plot in the upper half of Fig. 3.2, which shows the product of the square root of the required laser power times the junction resistance; the line through the points represents the coupling from an ac source resistance of ~ 200 Ω, which presumably reflects the antenna resistance. Thus the high-
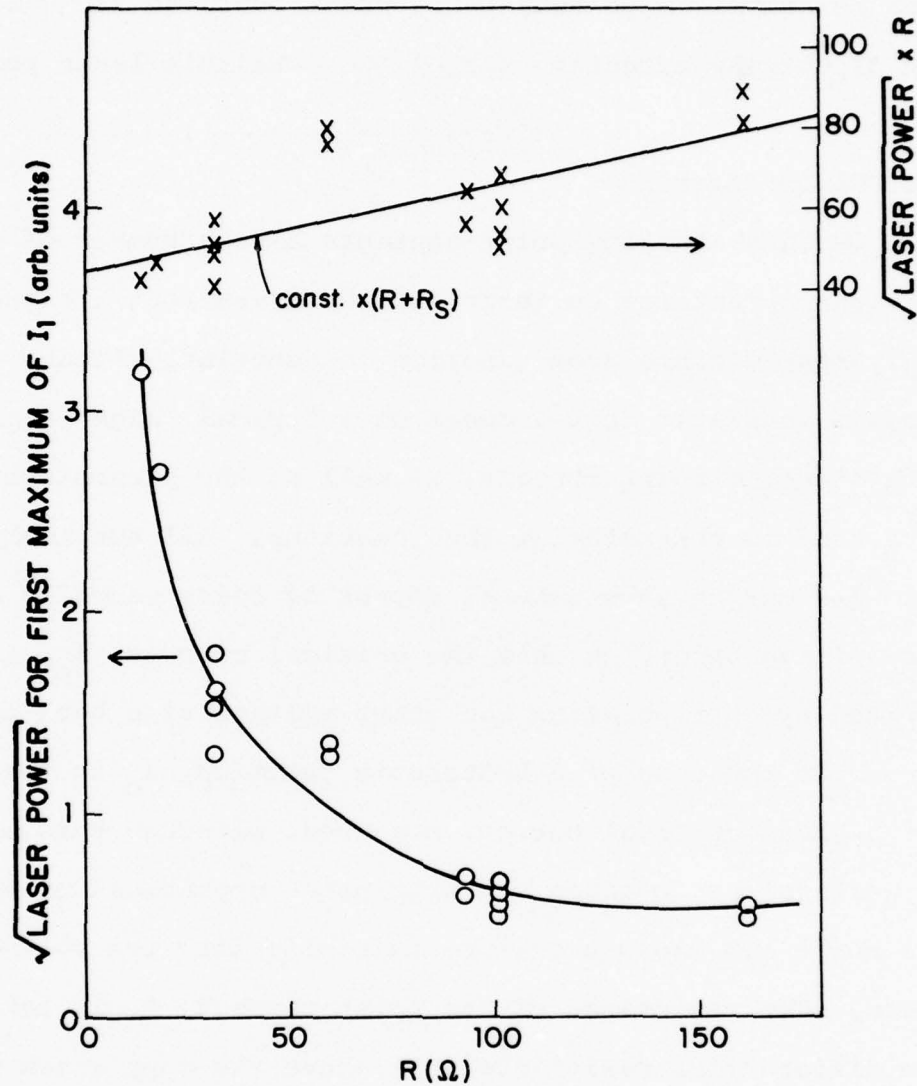
Fig. 3.2 Coupling effects. Lower curve is the square root of the laser power required to produce the maximum width of the first step as a function of junction resistance. Upper curve is the product of this times the resistance, with the *solid line* consistent with coupling from a source resistance, R_s, of ~200 Ω.

resistance junctions are very well matched both to the antenna and to free space. All of our experiments are performed with relatively high-resistance point contacts ($10 \ \Omega \lesssim R \lesssim 200 \ \Omega$) to make effective use of the available laser power.

3.4 Classification

Our high-quality point contacts have a number of distinguishing features on their dc I-V curves that are surprisingly reproducible from junction to junction. Figure 3.3 shows a schematic dc I-V curve of a typical "high"-quality, nonhysteretic point contact, as well as the parameters we have used to characterize the junctions. All our nonhysteretic I-V curves show a small amount of noise rounding at the voltage onset, so that the critical current, I_c, is defined by extrapolating the sharp voltage rise back to zero. In the case of a hysteretic junction, I_c is taken as the highest critical current measured, although this may not be well defined because any extraneous mechanical or electrical noise can cause premature switching into the voltage state. The resistance of the point contact, R, is taken as the differential resistance just above the gap, which we find to be the same as the resistance measured when we can couple in enough laser power to drive the junction Ohmic. The extrapolation of this differential resistance line back to the current axis defines the excess current, I_{ex}. The height of the voltage jump, V_j, is taken as the voltage at which the I-V curve bends over after the first steep,
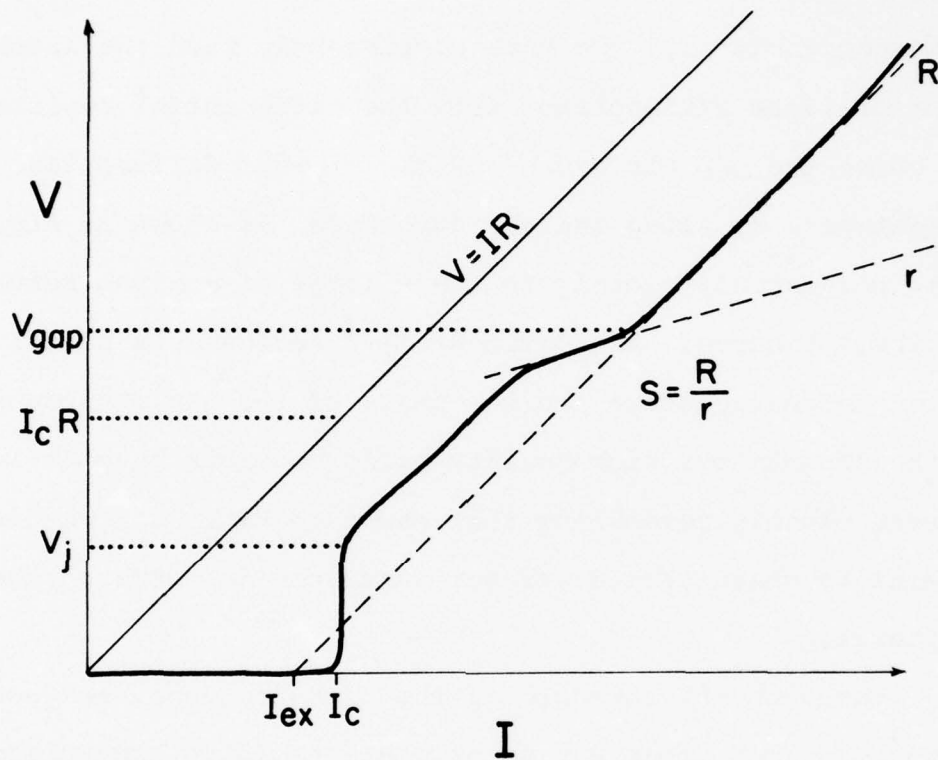
Fig. 3.3 Schematic of a high-quality dc I-V curve
showing the parameters used for characterization.

straight rise. The gap-related structure is quite pronounced and always has the form of a decrease in the differential resistance below the gap voltage followed by an increase just above, as shown in Fig. 3.3. The identification of an appropriate feature for defining the gap voltage, V_{gap}, is somewhat arbitrary. We have consistently used the intersection of lines extrapolated from the differential resistance, R, above the gap structure and the minimum differential resistance, r, along the gap structure, as shown in Fig. 3.3. This corresponds closely to the voltage of maximum curvature on the I-V curve. The ratio $R/r \equiv S$ serves as a useful parameter to characterize the sharpness of the gap structure. Although only our high-quality point contacts have dc I-V curves closely resembling that shown in Fig. 3.3, we find it useful to characterize all our junctions in terms of these features.

Based on the strength of the high-frequency ac Josephson effect, we can group our point contacts into three classes. In the first of these are our high-quality junctions, which show a strong ac Josephson effect well above the gap, as evidenced by a readily visible first step induced by 119 μm radiation at 5.22 mV, or seven or more harmonics of the 1.25 mV step induced by 496 μm radiation. The second class contains our "marginal" junctions, which show no evidence of a first step with 119 μm radiation. However, their dc I-V curves have many qualitative similarities to those of Class I, and this type of junction usually shows two or three steps

when irradiated with 496 μm radiation. Finally, those junctions showing no steps with either FIR wavelength are grouped in the third class. We now discuss these classes in more detail.

Class I

An example of a high-quality, nonhysteretic I-V curve is shown in Fig. 3.4(a). Such I-V curves are distinguished by the following features: a) an I_cR product that is always very close to the theoretical value of ~2.2 mV -- typically within 20%, b) a very steep but nonhysteretic voltage onset, with $V_j \sim 0.5 \ I_cR$, c) V_{gap} between ~2.8 and 3.1 mV, d) very pronounced gap-related structure with $S \gtrsim 2.0$, and e) an excess current that extends to bias voltages far above the gap (to ~30-50 mV) and has a value of $I_{ex} \sim 0.8 \ I_c$ just above the gap. These features are quite reproducible in point contacts of this type, as shown in Table 3.1(a), which lists data for a number of these junctions of varying resistances. As in Fig. 3.4(b), the first step was always easily visible with the 119 μm radiation. The fourth and higher harmonics of 496 μm radiation were also always seen. This class of point contacts is the only one whose I-V curves have such a reproducible characteristic shape.

The differential resistance of the initial, steep voltage rise was very large for high-quality junctions, and, for some junctions, it was impossible to maintain a stable dc bias on the rise with the current bias used. In fact some

44
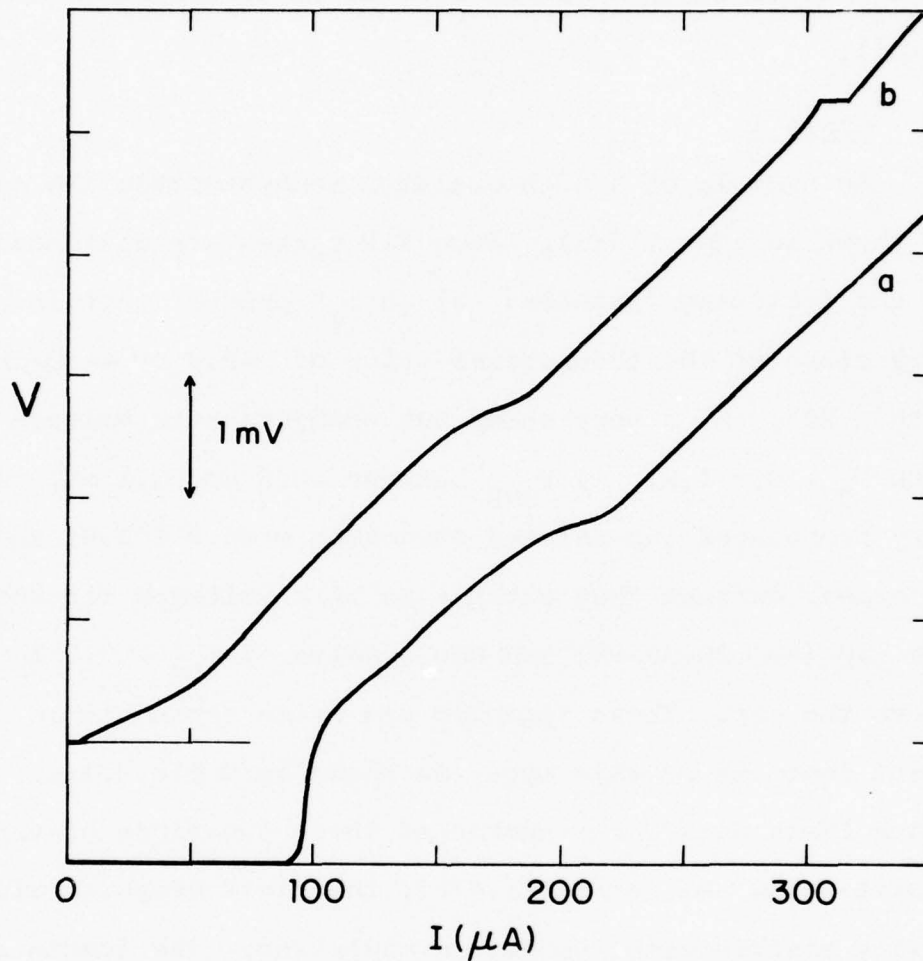
Fig. 3.4   Typical high-quality (Class I) non-hysteretic dc I-V curves, (a) without incident radiation, and (b) with 119 μm radiation which induces a step at 5.22 mV. This junction has R = 23 Ω and $I_c R$ = 2.2 mV.

Table 3.1(a)

Class I Nonhysteretic Contacts

$R(\Omega)$	$I_c(\mu A)$	$I_cR(mV)$	V_j/I_cR	I_{ex}/I_c	$V_{gap}(mV)$	S
161	11.2	1.8	0.50	0.75	3.0	3.1
136	11.8	1.6	0.57	0.82	3.0	2.2
110	18.2	2.0	0.47	0.84	3.0	2.5
101	20.1	2.0	0.50	0.73	2.9	3.1
93	22.5	2.1	0.48	0.84	2.9	2.5
91	21.2	1.9	0.49	0.83	2.7	2.2
80	22.5	1.8	0.57	0.74	2.9	2.5
77	28.6	2.2	0.43	0.78	2.8	2.5
71	26.9	1.9	0.47	0.87	2.7	2.1
60	42.0	2.5	0.47	0.82	3.0	2.4
49	38.8	1.9	0.55	0.83	3.0	2.6
43	53.3	2.3	0.43	0.70	2.8	3.2
43	51.2	2.2	0.45	0.76	2.8	2.7
28	60.7	1.7	0.54	0.78	3.0	2.3
23	95.7	2.2	0.46	0.75	3.0	2.6

of our high-quality junctions were clearly hysteretic, as illustrated by the example in Fig. 3.5(a). Except for the hysteretic voltage onset, this I-V curve is quite similar to that shown in Fig. 3.4, with the same sort of excess current, similar gap structure and a high value of S. This similarity is further shown by Table 3.1(b), which lists the same parameters as Table 3.1(a) for a number of high-quality hysteretic junctions. There is not the same consistency in the values of I_cR and I_{ex}/I_c as there is in Table 3.1(a). However, those junctions that have low I_cR products tend to have $I_{ex}/I_c > 0.8$, consistent with an erroneously low measurement of I_c due to premature voltage switching induced by extraneous noise. As shown in Fig. 3.5(b), these curves also exhibit a strong high-frequency ac Josephson current, since the 119-μm-laser-induced step is readily visible.

Class II

The I-V curve in Fig. 3.6(a) is an example of a marginal-quality point contact, and Table 3.2 lists the characteristics of a number of these junctions. The I_cR products of these junctions are generally lower than those of the high-quality junctions, typically between 1.0 and 1.8 mV. They have the same sharp voltage onset, which is also occasionally hysteretic, and again have $V_j \sim 0.5\ I_cR$. However, the gap-related structure is somewhat less pronounced than that of the high-quality junctions, with $S \lesssim 2.0$, while the energy-gap voltages are somewhat lower than Class I junctions, with
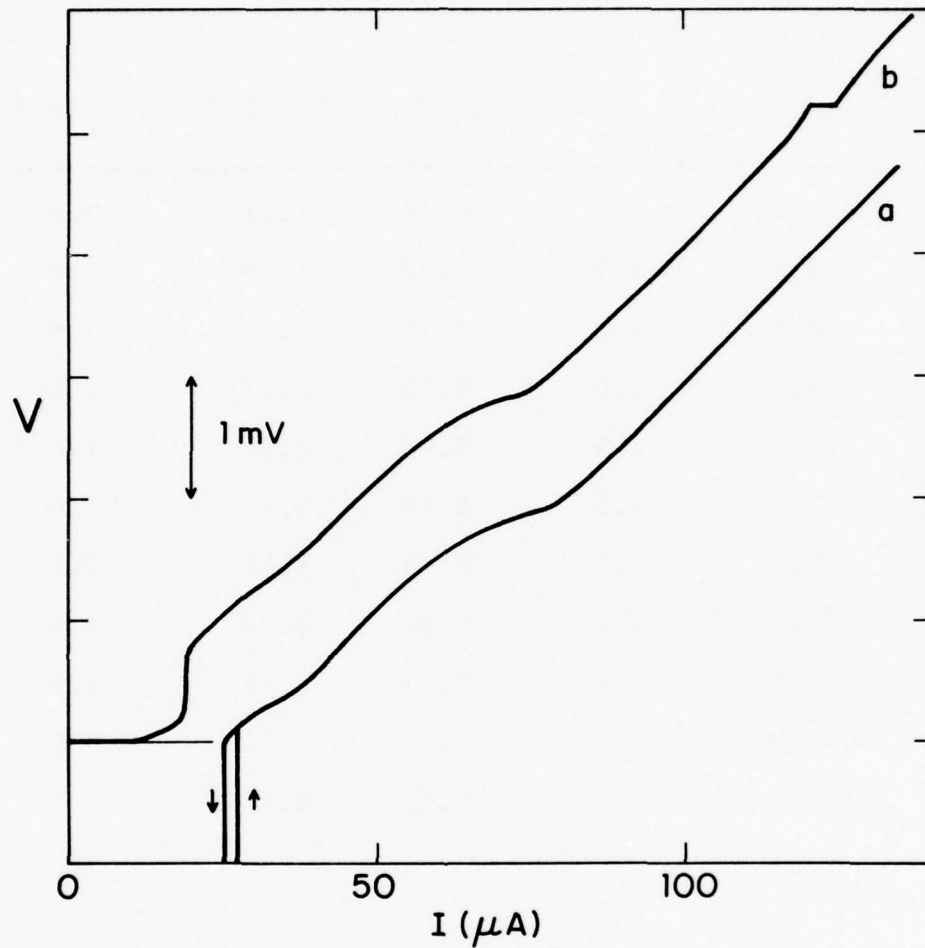
Fig. 3.5   Typical high-quality (Class I) hysteretic dc I-V curves, (a) without incident radiation, and (b) with 119 μm radiation which induces a step at 5.22 mV.   This junction has R = 54 Ω and $I_c R$ = 1.5 mV.

Table 3.1(b)

Class I Hysteretic Contacts

$R(\Omega)$	$I_c(\mu A)$	$I_c R(mV)$	$V_j/I_c R$	I_{ex}/I_c	$V_{gap}(mV)$	S
162	6.8	1.1	0.39	1.17	3.0	2.6
136	9.5	1.3	0.49	1.19	3.0	2.4
125	8.8	1.1	0.50	1.45	2.9	2.0
104	9.6	1.0	0.62	1.23	3.1	2.8
88	21.6	1.9	0.65	0.60	3.0	3.5
86	17.4	1.5	0.59	1.0	2.9	4.2
66	25.8	1.7	0.47	1.18	2.9	2.6
54	27.8	1.5	0.69	0.79	2.9	3.9
50	36.6	1.8	0.61	0.50	3.0	2.6
30	73.9	2.2	0.49	0.71	2.8	4.5
14	157.0	2.2	0.49	0.77	2.7	2.3
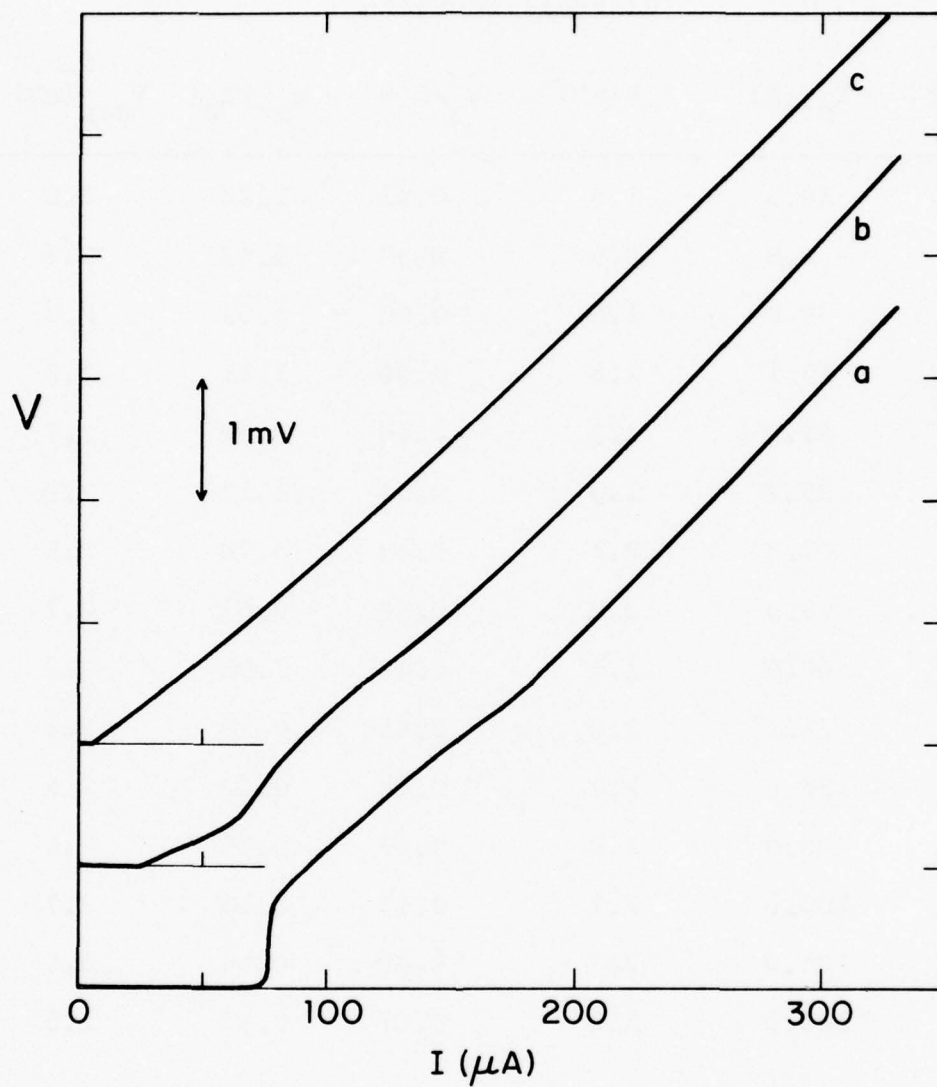
Fig. 3.6   Typical marginal-quality (Class II) dc
I-V curves, (a) without incident radiation, and
(b) and (c) with increasing 119 μm radiation showing
no step. This junction has R = 21 Ω and $I_c R$ = 1.6 mV.

Table 3.2

Class II Contacts

$R(\Omega)$	$I_c(\mu A)$	$I_cR(mV)$	V_j/I_cR	I_{ex}/I_c	$V_{gap}(mV)$	S
145	10.3	1.5	0.41	1.22	2.8	2.0
132	6.8	0.9	0.52	1.43	2.7	1.7
111	9.0	1.0	0.50	1.33	2.8	1.6
86	15.1	1.3	0.46	1.11	2.7	1.4
41	31.0	1.2	0.49	0.86	2.7	1.4
37	35.2	1.3	0.54	1.12	.6	1.6
31	67.7	2.1	0.43	0.78	2.5	1.6
3?	75.0	2.3	0.50	0.63	2.7	1.4
?5	60.0	1.5	0.49	1.02	2.7	1.6
21	76.2	1.6	0.41	0.78	2.5	1.3
19	126.0	2.4	0.42	0.82	2.5	1.7
18	100.0	1.8	0.49	0.75	2.5	1.3
17	100.0	1.7	0.47	0.88	2.7	1.4
17	135.0	2.3	0.40	0.64	2.5	1.9
13	126.0	1.6	0.61	0.83	2.5	1.5

V_{gap} between ~2.5 and 2.8 mV. Again there is a large excess current above the gap, although the values of I_{ex}/I_c are not as consistent from junction to junction as they are for those in Class I. These junctions do not exhibit a step at 5.22 mV when irradiated by _any_ amount of power at the 119-μm-laser line, as shown, for example, by the I-V curves in Figs. 3.6(b) and 3.6(c) for increasing laser powers. Here, the reduction in the critical current with increasing laser power serves both as a confirmation that laser power is in fact coupled into the junction, and as a guide to the amount of power coupled in. The 496 μm radiation usually produces two or three steps in these junctions, but the high harmonics seen with Class I point contacts are not seen with these.

Class III

The type of point contact represented by the I-V curve shown in Fig. 3.7(a) is typical of the poorest class of junctions we see. The I_cR products of these junctions are quite low ($\lesssim$ 1.0 mV) and the initial voltage jump is not as sharp as it is on the better quality junctions, with V_j not as well defined. There is practically no gap structure at all, with S very close to 1.0. V_{gap} is also not as well defined as for the higher-quality junctions, but is generally considerably lower than the typical values for Class I and II contacts. There is, however, always an excess current above the gap, and the I-V curves are frequently hysteretic. Table 3.3 lists the parameters for a number of these junctions,
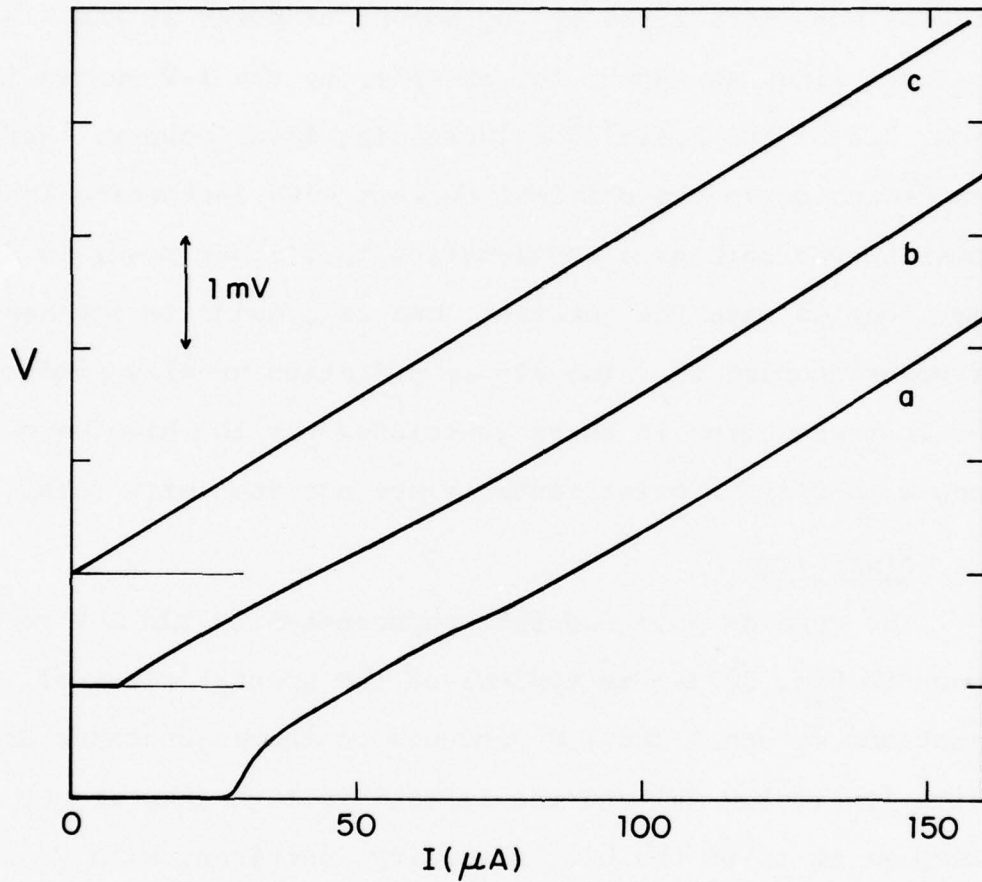
Fig. 3.7 Typical poor-quality (Class III) dc I-V
curves, (a) without incident radiation, and (b) and
(c) with increasing 119 μm radiation. There is no
step, even though enough laser power could be coupled
into the junction to drive it Ohmic, (c). This junc-
tion has R = 33 Ω and $I_c R = 0.9$ mV.

Table 3.3

Class III Contacts

$R(\Omega)$	$I_c(\mu A)$	$I_cR(mV)$	V_j/I_cR	I_{ex}/I_c	$V_{gap}(mV)$	S
80	5	0.40	0.5	1.1	1.6	1.1
50	10	0.50	0.7	1.0	2.8	1.1
50	3	0.15	0.6	0.43	2.0	1.05
48	11	0.50	0.5	1.6	2.3	1.3
30	10	0.30	0.8	1.4	1.8	1.2
28	21	0.59	0.3	1.2	2.2	1.1
26	10	0.26	0.7	1.1	2.3	1.1
15	30	0.45	0.4	0.8	1.1	1.1
12	80	0.96	0.7	0.72	2.0	1.1
5	140	0.70	0.4	1.3	2.3	1.1

for comparison with the other classes. This class of junc-
tions shows no high-frequency ac Josephson effect at all,
as is illustrated by the example in Figs. 3.7(b) and 3.7(c),
which shows no step at 5.22 mV for increasing power from
the 119-μm-laser line. These junctions are again clearly
coupling to the radiation and for this particular junction
there was enough laser power to drive it completely Ohmic.
The I-V curves of this class sometimes show a step at 1.25
mV when irradiated with 496 μm radiation, but the second
harmonic is rarely seen. This sort of junction is never
used in any of our laser work, and the contact is always
remade when one is obtained.

3.5 High-Voltage Behavior

We find a very strong correlation between the existence
of the high-frequency ac Josephson effect and the sharpness
of the structure at the energy gap. In Fig. 3.8 we plot
N_{max}, the highest observed harmonic of the 1.25 mV step
induced by 496 μm radiation, against S for those junctions
for which sufficient laser power was available to establish
a definite maximum. There is an approximately linear
dependence of N_{max} on S. This strong correlation tends to
support, but does not prove, a causal link between the
Josephson effect and the gap-related structure.[45]

An alternate way of showing the correlation of the
sharpness of the gap structure with the high-frequency ac
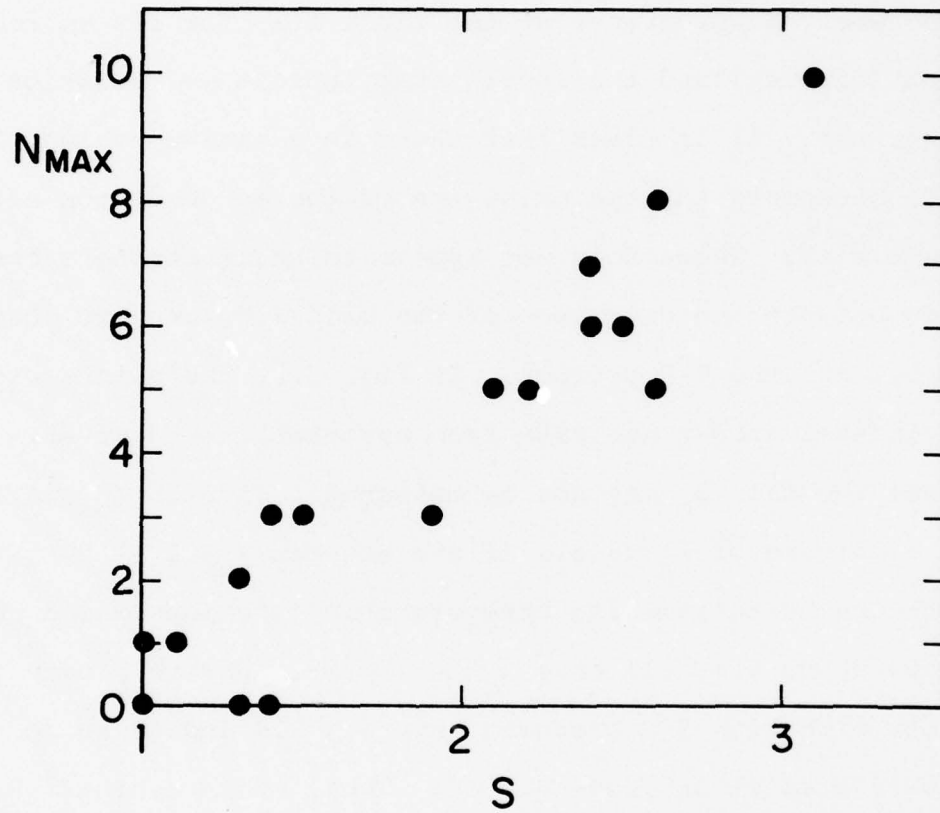
Fig. 3.8 N_{max}, the highest harmonic of the 1.25 mV step induced by 496 μm radiation, plotted against the gap sharpness parameter, S, for those junctions for which there was enough laser power to determine a definite N_{max}.

Josephson effect is to look for the minimum value of S
required to see a step at a given voltage. In Fig. 3.9, we
have plotted S versus I_cR, using open points for junctions
that showed an ac Josephson effect at voltages higher than
5 mV, and solid points for those that did not. The criterion
used was the appearance of the first step for 119 μm radia-
tion (circles) and the fourth step for 496 μm radiation
(squares). It is clear that there is a minimum value, $S \approx$
2.0, necessary for the existence of the ac Josephson effect
above 5 mV. There does not appear to be as strong a correla-
tion between the existence of the high-frequency ac Josephson
effect and the I_cR product. In Fig. 3.9, the points with
horizontal arrows are data from hysteretic I-V curves,
where the full I_c may not be measured. If 1.25 I_{ex} is used
as a measure of I_c (i.e., if one assumes $I_{ex}/I_c = 0.8$), then
both the hysteretic and nonhysteretic junctions which show
steps above 5 mV all have $I_cR \gtrsim 1.6$ mV. However, many junc-
tions with high I_cR products have $S \lesssim 2.0$ and these do not
show a step at or above 5.0 mV. Thus, while a high I_cR
product is a necessary condition, the best indication of the
existence of a strong high-frequency ac Josephson effect is
a large value of S. This gives a useful prescription for
recognizing point contacts with good high-frequency perform-
ance from the shape of their dc I-V curves.

All of our point contacts exhibit an excess current, I_{ex},
which falls off slowly with voltage above the gap, but per-
sists to voltage levels of ~35-50 mV. Akimenko et al.[46]
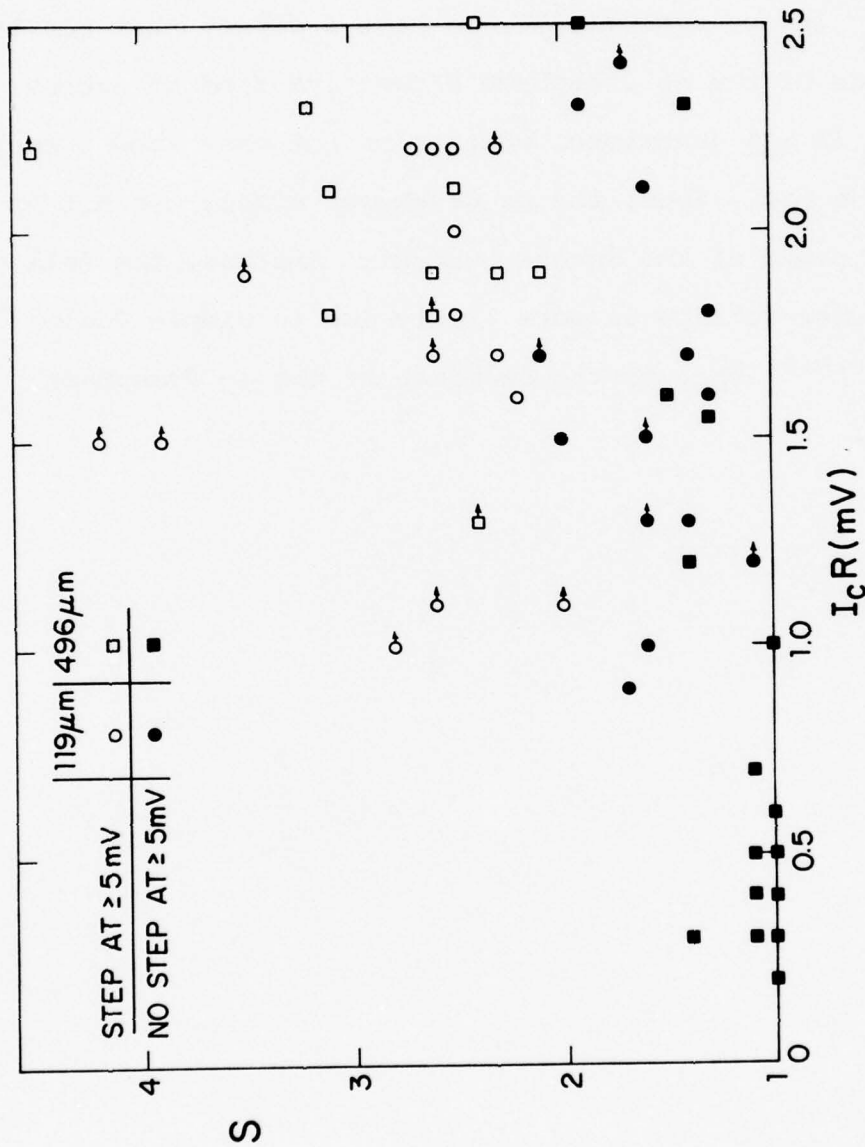
Fig. 3.9 S versus $I_C R$. The points with horizontal arrows are data from hysteretic junctions where the full I_C may not be measured, so their $I_C R$ products may be erroneously low. Note that FIR steps are seen (open symbols) only for $S \gtrsim 2$.

have measured I_{ex} as a function of voltage in Nb point con-
tacts, and make the unsubstantiated claim that the excess
current is proportional to the strength of the ac Josephson
effect. In our experiments, we have a direct test for the
existence of the ac Josephson effect and find an excess
current in all junctions, whether or not they show a step
above the gap. Thus, the ac Josephson effect can not be the
primary cause of the excess current. Instead, the fall off
of I_{ex} with voltage is more likely due to simple Joule
heating[3,6,47] than to the decrease of the ac Josephson
current.

CHAPTER IV

THEORY

4.1 I-V Curves

The reproducibility and consistency of our high-quality
point contacts provide hope for an eventual theoretical
description of the dc I-V curves. Since the physical charac-
teristics of the minute active region are not known in
detail, it is difficult to decide a priori the best way to
model the junction theoretically. In this section we com-
pare some of the theoretical calculations with the I-V curves
of our high-quality point contacts, and attempt to identify
the more promising physical models.

It is particularly interesting to examine our measure-
ments to see what light they shed on the longstanding issue
of whether point contacts are best modelled as tunnel junc-
tions or as metallic constrictions. Models have been developed
to describe Josephson-effect devices with each of these types
of weak links. However, as the somewhat ill-defined struc-
ture of a point contact is approached, the distinctions
between the predictions of the two models become less apparent.
For example, if the characteristic size of a constriction, a,
is less than the electron mean free path, ℓ, so that an
electron can pass through it without scattering, the metallic
constriction is expected to become more "tunnelling-like" in

its behavior.[48,49] On the other hand, the I-V curves of small-area, high current-density (low RC) tunnel junctions are predicted to become similar in many respects to those of metallic constrictions.[49,50] Thus, the more fundamental conceptual issue is whether there are, indeed, significant differences between the two types of barriers which persist even in the limit of very small cross-sectional areas.

Our high-quality (Class I) point contacts show striking reproducibility from junction to junction, both in their dc I-V curves and in their high-frequency performance, suggesting that their behavior is converging on that of the "ideal", clean, low-capacitance point contact. We thus have a set of reproducible features on the dc I-V curves which can be compared with theoretical predictions and with experimental results from Josephson-effect devices having more clearly defined geometries, in an attempt to determine the physical structure of the minute contact region.

Of all the features on the dc I-V curves, the energy-gap structure and voltage seem to correlate most strongly with the existence of the ac Josephson effect and the high-frequency performance of the junction. The values of V_{gap} of our high-quality junctions generally tend to be slightly greater than the 2.8 mV commonly quoted for other Nb point contacts,[5,46] and are comparable to the V_{gap} measured for Nb/Nb tunnel junctions.[51] However, they are still slightly lower than the 3.12 mV energy gap of pure, bulk Nb.[52]

It is possible that the pressures exerted on the extremely small area of the point while the contact is made work-harden the metal in the vicinity of the contact, causing a reduction in the energy gap. There is also some evidence[53] for the existence of suboxides on the surface of niobium with a lower T_c of ~ 7.2 K, implying $2\Delta/e \approx 2.5$ mV. It is thus possible to speculate that the cause of the lowered V_{gap} of our Class II and III junctions is a remaining layer of niobium suboxide at the contact region. This implies that a clean surface, giving as high a V_{gap} as possible, is necessary to obtain high-quality junctions, and suggests that our Class I point contacts may be entirely free of any oxide layer.

In Fig. 4.1, we show the shape of the gap structure from a series of I-V curves, scaled to have the same slope. Their high-frequency performance, as characterized by their N_{max} (496 μm), improves from left to right. As shown by the curve with $N_{max} = 9$, the shape of the gap structure of our high-quality junctions consists of a relative decrease in the current below the gap voltage. This is typical of the shape observed in very "clean" Nb point contacts and in the Nb junctions used for high-frequency mixing experiments.[5] However, this shape contrasts with that observed in low-impedance microbridges, for which a relative decrease in the current just above the gap voltage is typical.[54,55] Such a shape is illustrated by the left-most structure in Fig. 4.2, which is taken from the I-V curve of a very low-impedance
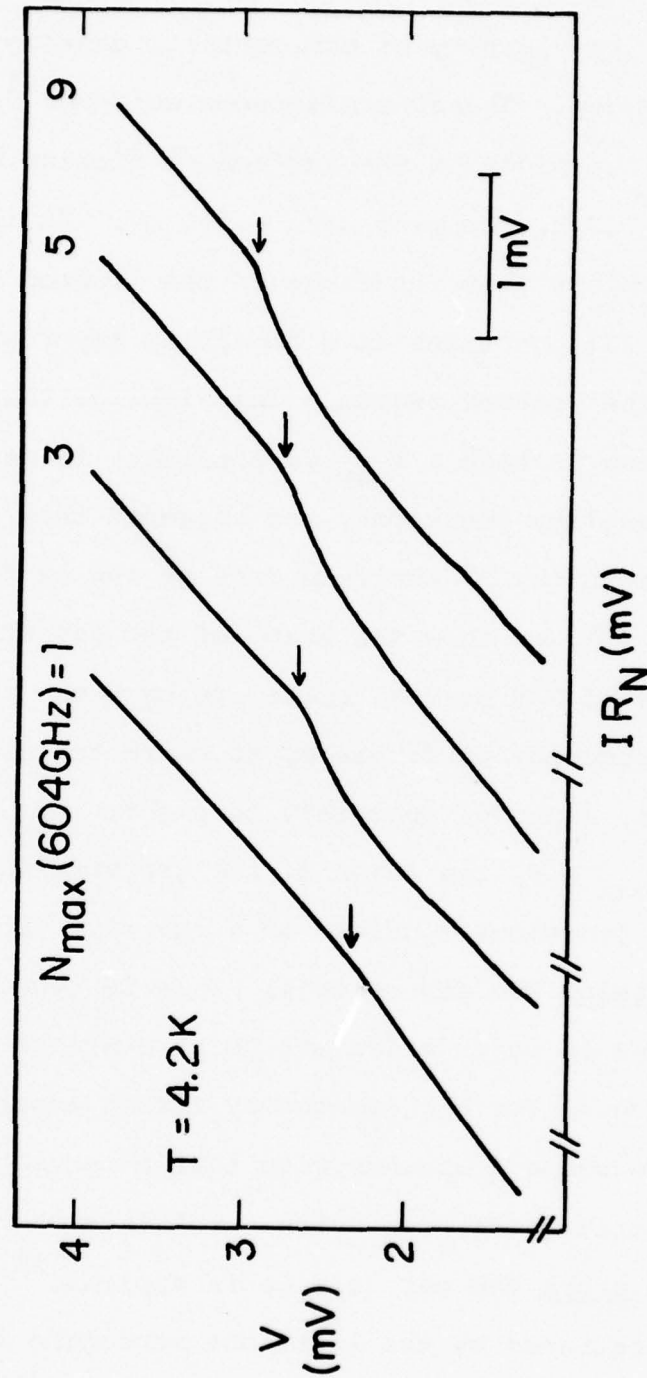
Fig. 4.1 Gap structure in point contacts of different N_{max}. The high-frequency performance improves as N_{max} increases. The curves are all scaled to have the same slope.
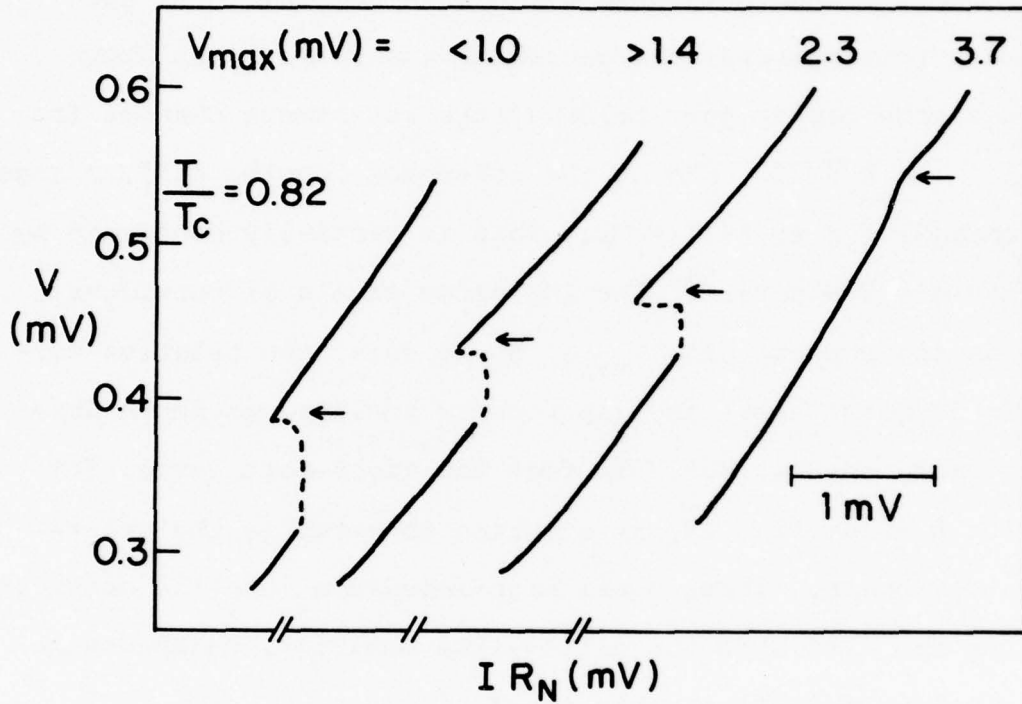
Fig. 4.2   Gap structure in tin VTB's taken from Ref. 55.
The impedance tends to increase as V_{max} increases. The
higher impedance VTB's have gap structure that is
approaching the point-contact shape. The curves are all
scaled to have the same slope.

VTB of Octavio.[55] The similarity of the point-contact gap-
structure shape we observe to that seen in oxide tunnel
junctions suggests labelling this shape "tunnelling-like."
In fact, however, Yanson has observed both types of shapes
in metallic constrictions in his studies of the I-V curves
of metallic shorts through dielectric layers.[48] He sees
the current decrease change continuously from just above
the energy gap to just below as the resistance changes from
$R \lesssim 1\Omega$ to $R \gtrsim 20\Omega$, and as the coherence length, $\xi(T)$, changes
from $\xi(T) \gtrsim a$ to $\xi(T) \ll a$. This is partially confirmed by
Octavio's VTB data.[55] The impedance of his microbridges
tends to increase with V_{max}. As it does, the relative cur-
rent decrease above the gap becomes smaller, as shown dra-
matically in Fig. 4.2. In fact the right-most curve, for
which R is still $\lesssim 2\Omega$, is starting to resemble the point-
contact shape. Thus, small high-impedance metallic constric-
tions can also show tunnelling-like behavior, undercutting
the meaningfulness of this label.

Explanations of the gap and subharmonic gap structures
have drawn a distinction between "multiparticle tunnelling"
and "Josephson self-coupling" as possible causes.[45,56,57]
This distinction is meaningful only for subharmonic gap
structure, since multiparticle tunnelling reduces to single
particle tunnelling for the structure at the energy gap, and
is included within the self-coupling theory.[58] Because of
the very steep voltage rise to $V_j \approx 0.5 \, I_c R$, the only sub-

harmonic gap structure we are able to see is that at half the energy gap. This structure is similar in shape to the structure at the gap, but is much less pronounced. Thus, although we observe a strong correlation between the ac Josephson effect and the structure at the energy gap, we can not draw firm conclusions about the causes of the subharmonic gap structure.

Werthamer's frequency-dependent self-coupling (FDSC) theory[58] has been used to calculate the I-V curve of a current-biased, zero-capacitance (high current-density) tunnel junction.[49,50] As shown in Fig. 4.3, the calculated I-V curve has large currents below the gap voltage (unlike the more usual tunnel-junction I-V curves) as well as a decrease in the current just below V_{gap}, in qualitative agreement with the I-V curves of our high-quality point contacts. However, the calculation assumes a singular BCS density of states in the electrodes and does not account for the effects of noise or current-induced disequilibrium, all of which must be included in a realistic manner if quantitative comparison with our data is to be made.

A feature of the I-V curves which is more likely to provide the basis for a conceptual distinction between tunnel-junction and metallic-constriction behavior of point contacts is the measured excess current at high voltages which is quite consistently about 0.8 I_c in our junctions, and which we have shown is not related to the strength of
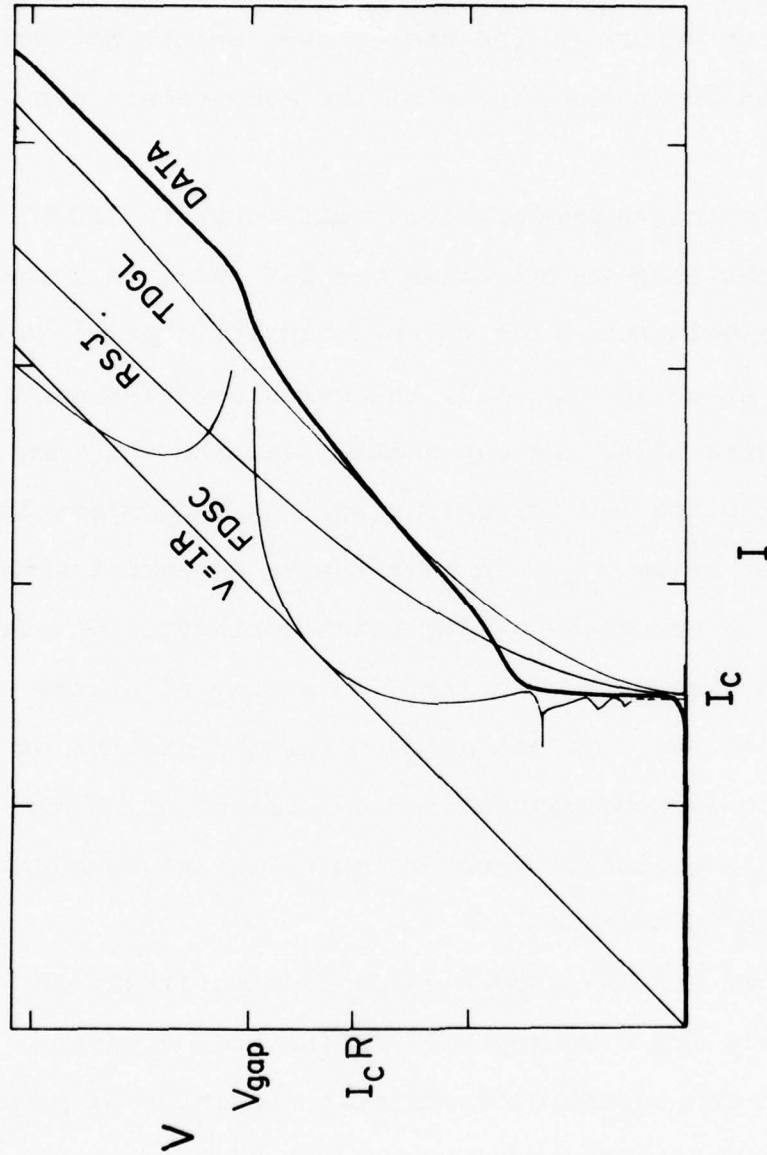
Fig. 4.3 Comparison of an "ideal" I-V curve with the results of the calculations based on three theoretical models. All three theoretical curves are scaled to have the same normal resistance as the data. The RSJ and TDGL curves are scaled to have the same critical current while the FDSC curve is scaled to have the same gap voltage as the data. The TDGL curve is calculated for a constriction one coherence length long and for an order-parameter relaxation time as given by microscopic theory for the dirty limit.

the Josephson effect at high frequencies. Such an excess
current is observed in all the various forms of metallic
microbridges, but not thus far in tunnel junctions. As
shown in Fig. 4.3, it is not predicted by the FDSC theory,
nor by the qualitative description provided by the resistively-
shunted-junction (RSJ) model. The only theories which have
provided a possible explanation for this feature consider
the dynamics of the superconducting order parameter inside
a continuous metallic link. Calculations of I-V curves using
time-dependent Ginzburg-Landau (TDGL) theory show that the
finite relaxation time of the order parameter inside the
metallic constriction of a VTB can cause an apparent excess
current.[60,61] In this description, the strongly supercon-
ducting banks hold up the magnitude of the order parameter
at the ends of the constriction, and effectively decrease
the voltage drop across the bridge required to drive a given
current. The magnitude of this insufficient voltage is
asymptotically voltage independent, and is equivalent to an
excess current. However, the exact shape of the calculated
I-V curve depends both on the length, L, of the constriction
and on the value of the order parameter relaxation time, τ.
Since this model assumes that the superconducting banks have
an undepressed order parameter ("rigid" boundary conditions)
the choice of an appropriate L is problematic for the point-
contact geometry, where the boundaries are not well defined.
The TDGL curve[61] shown in Fig. 4.3 is for $L = \xi$, and for

the value of τ predicted by microscopic theory for a super-
conductor in the dirty limit, and has an excess current of
$\sim 0.70\ I_c$, in reasonable agreement with our experimental
I_{ex}. However, other calculations[62] have indicated that the
behavior of the order parameter in the banks near the con-
striction may also play an important role in determining the
properties of the bridge, making the assumption of rigid
boundary conditions inadequate. Clearly more theoretical
work is required before a more quantitative comparison with
our data can be attempted.

Other explanations of the excess current seem less
likely to apply here. Deaver and Pierce[63] considered a
relaxation-oscillation model that is essentially an equiva-
lent circuit model with an additional inductance in series
with the Josephson element of the RSJ circuit. This model
predicts a smaller excess current of $0.5\ I_c$, and requires a
large series inductance, which seems unlikely in junctions
where ac Josephson currents flow well above the gap fre-
quency. The phase-slip models of Rieger et al.[64] and Skocpol
et al.[65] estimate an excess current of $0.5\ I_c$ and $0.67\ I_c$
respectively, but were created to describe slow variations
on the scale of the Ginzburg-Landau relaxation time, and
therefore are not suitable for point contacts at high voltages.

Thus, as a whole, the experimental evidence seems to
suggest that our point contacts are best modelled as extremely
small metallic constrictions, although the distinction between
metallic-constriction and tunnel-junction behavior is perhaps

somewhat blurred. It will be interesting to see whether
the new generation of very small-area, high current-density
tunnel junctions which can now be fabricated show Ohmic or
excess-current type behavior above the gap. Ohmic behavior
would tend to establish that there are some irreducible
differences between metallic constrictions and tunnel junc-
tions, despite the obvious generality of the Josephson phen-
omena in weak links.

4.2 Josephson Steps

We would like to use our high-quality point contacts to
measure the strength and frequency dependence of the Joseph-
son effect. Our ability to do this depends on a study of the
laser-induced constant-voltage steps on the dc I-V curves.
Thus, we need a theoretical model to relate the behavior of
the steps to that of the Josephson effect itself. In this
section, we discuss the theoretical predictions that we fit
to our measurements of the power dependence of the laser-
induced steps.

As has been discussed in the previous section, none
of the theories currently available adequately describes the
characteristic shape of the dc I-V curves of our junctions.
Thus, they are unlikely to predict accurately the shape of
the constant-voltage steps. This may have an adverse effect
on the calculated power dependence, since the step's width
may be quite sensitive to its shape.

In order to make them more tractable, all of the theories make simplifying approximations for the source impedance. They assume either a low-resistance, constant-voltage source, or a high-resistance, constant-current source. Experimentally, the bias impedance lies somewhere in between, and probably has a rather complicated frequency dependence as well. The dc source impedance is defined by the bias network used. In these experiments, it was always very high compared to the junction resistance R. However, we have shown that the rf source impedance seems to be that of the antenna, and is $\sim$200 Ω at 604 GHz. This is not much larger than the resistance of a typical junction (R $\sim$ 100 Ω). The type of bias network assumed can have a significant effect on the theoretical predictions. Unfortunately, a tractable model with a more realistic bias impedance does not exist.

The only theories that have been extended to calculate the power dependence of the Josephson steps are based on a tunnel-junction model of the weak link. As shown in the previous section, the experimental evidence seems to suggest that our point contacts are better described as extremely small metallic constrictions. Nevertheless, tunnel-junction models often seem to work quite well for point contacts, and give good qualitative agreement with much of the data. The reproducibility of our measurements allows us to test the theories more quantitatively.

The current I through a small-area tunnel junction at

temperature T and bias voltage V can be written as[1]

$$I = I_p(V,T)\sin\varphi + I_{qp}(V,T) + I_{qpp}(V,T)\cos\varphi \qquad (4.1)$$

where $\qquad \dfrac{d\varphi}{dt} = \dfrac{2eV}{\hbar} \qquad\qquad\qquad\qquad (4.2)$

and φ is the phase difference across the tunnel junction. The first term is the supercurrent or Josephson pair current, and at low frequencies (voltages), $I_p \approx I_c$. The second term is the quasiparticle or normal current, which is highly non-linear in the case of a tunnel junction. The linear approximation of a constant resistance R leads to the resistively-shunted junction (RSJ) model, with $I_{qp} = V/R$. The final term is the "cosine" term, and has no effect on the magnitude of the steps for a voltage-biased junction.[66] It is usually omitted in the RSJ approximation.

The simplest approximation for the power dependence of the step current-widths is obtained for low frequencies (so that $I_p = I_c$) and for a junction voltage-biased with both a dc voltage V_0 and a laser-induced ac voltage of angular frequency ω_L, $V_{ac}\cos\omega_L t$. This results in the familiar Bessel-function power dependence of the steps,[67]

$$\frac{I_n}{I_c} = |J_n(2\alpha)| \qquad\qquad\qquad\qquad (4.3)$$

where $\qquad 2\alpha = 2eV_{ac}/\hbar\omega_L \quad . \qquad\qquad\qquad (4.4)$

Here, J_n is the nth Bessel function and I_n is the current

half-width of the nth step, at the dc voltage

$$V_0 = n\ \frac{\hbar\omega_L}{2e}\ .$$ (4.5)

Werthamer[58] has calculated the voltage (frequency) dependence of Eq. (4.1) at T=0, assuming a perfect BCS density of states for the superconductors on either side of the barrier. The results for the supercurrent, I_p, can be written as[68]

$$\frac{I_p(\omega_J)}{I_c} = \frac{2}{\pi}
\begin{cases}
K(\hbar\omega_J/4\Delta) & \hbar\omega_J/4\Delta \leq 1 \\[2mm]
\dfrac{4\Delta}{\hbar\omega_J}\ K(4\Delta/\hbar\omega_J) & \hbar\omega_J/4\Delta \leq 1
\end{cases}$$ (4.6)

where ω_J is the Josephson frequency (or voltage $V = \frac{\hbar}{2e}\ \omega_J$), 2Δ is the superconducting energy gap and K is the complete elliptical integral of the first kind. According to Eq. (4.6), the Josephson current is approximately constant at voltages below the gap, has a logarithmic singularity (the Riedel peak[69]) at the gap, and falls off approximately as $1/\omega_J$ above the gap. When this frequency dependence of I_p is included, Eq. (4.3) is generalized to[68]

$$\frac{I_n}{I_c} = \frac{1}{I_c}\left| \sum_{k=-\infty}^{\infty} J_k(\alpha)J_{n-k}(\alpha)I_p(|2k-n|\omega_L) \right|\ .$$ (4.7)

If the summation converges before $|2k-n|\omega_L$ becomes comparable

to $4\Delta/\hbar$, Eq. (4.7) reduces to the simple Bessel-function dependence of Eq. (4.3). Thus at low ac frequencies, the effect of the frequency dependence of I_p is not seen until α becomes quite large, requiring large rf drive powers. However, for the relatively high laser frequencies used in this experiment, Eq. (4.7) must be used for all laser powers (α).

If one of the $|2k-n|\omega_L$ harmonics of the laser frequency is equal to $4\Delta/\hbar$, that term in the summation in Eq. (4.7) becomes singular. This has a pronounced effect on the power dependence of the step and has been used to experimentally study the Riedel singularity in both tunnel junctions[68,70] and point contacts.[71] The maximum step-width enhancement due to the singularity is generally found to be about a factor of three. To obtain quantitative agreement with the data, the theory must be modified to account for mechanisms such as quasiparticle damping,[72] which round off the singularity. This adds a complex component to the energy-gap parameter $\Delta(\omega)$, which must be included in a modified version of Eq. (4.7). This has been done by Buckner and Langenberg,[70] who find good agreement between their theoretical calculations and their tunnel-junction data.

All the experimental investigations to date have measured the frequency dependence of I_p only in the vicinity of the singularity. Thus they have been restricted to a frequency range within ~5% of the Josephson frequency at the gap,

$\omega_J = 4\Delta/\hbar$. Our experiment is not designed to probe the singularity. In fact, we have not found it necessary to use the singularity-modified version of Eq. (4.7) to account for any of our data. Instead, we wish to extend the frequency range of the measurement, particularly above the gap.

Examination of Eq. (4.7) shows clearly why the fundamental laser-induced steps are the most direct probe of the strength of the Josephson effect above the energy-gap frequency. For n=1, the leading term in the summation is

$$\frac{2}{I_c} J_0(\alpha) J_1(\alpha) I_p(\omega_L) \; ,$$

which is proportional to the Josephson current at the laser frequency. The additional terms are contributions from I_p at higher harmonics of ω_L, where the Josephson current has rolled off even further. However, for a step at a harmonic of a lower frequency, there is always a contribution to the summation from $I_p(0)$ for n even and from $I_p(\omega_L)$ for n odd. These terms add a lower frequency component of the Josephson current where I_p is larger. Thus, a harmonic step is a less direct measure of $I_p(n\omega_L)$ than the fundamental step at the same voltage. In our experiments, we vary the laser wavelength and use only the fundamental step to study the frequency dependence of the Josephson effect.

The theories resulting in Eqs. (4.3) and (4.7) both make the approximation of a purely voltage bias at all frequencies. Other models make the opposite approximation for

the source impedance, treating the junction as current-biased. The simplest of these is the RSJ model[59] in which $I_p(\omega) = I_c$, $I_{qp} = V/R$, and $I_{qpp} = 0$. Russer[73] has used an analogue computer to calculate the RSJ predictions of the power dependences of the steps for various normalized frequencies.

$$\Omega = \frac{\hbar\omega_L}{2eI_cR} \quad . \tag{4.8}$$

He finds the Bessel-function behavior predicted by Eq. (4.3) for $\Omega > 1$, but finds substantial changes due to the current bias when $\Omega < 1$. At low temperatures, I_cR is theoretically expected[74] to be related to the gap voltage,

$$I_cR = \frac{\pi}{4}\frac{2\Delta}{e} \quad . \tag{4.9}$$

Thus, we expect a current bias to cause significant changes in the power dependence when the fundamental step is below the gap voltage.

While the RSJ model gives a qualitative account of the influence of a current bias, it does not include any effects due to the frequency dependence of the Josephson current. To do this, we must use the full frequency-dependent theory[58] itself, inverting Eq. (4.1) to solve for the voltage, with the assumption of a current bias.[49,50] This is simplified by the use of a reformulation of the theory in the time domain.[75] It includes the full frequency dependence of the Josephson current, as well as any effects the "cosine" term

may have for the current-biased case. However, unlike the RSJ model, the quasiparticle term includes the nonlinear resistance characteristic of a tunnel junction.

We have performed computer calculations using a technique similar to that suggested by Harris[76] to determine the step widths for the case of both dc and ac current sources. The current and voltage across the junction are assumed to be zero until time t=0, when the current drives are switched on. Then the Werthamer theory in the time domain is used to calculate the voltage across the junction. This is done at successively increasing small time intervals, with the results at each time depending on the voltage at all previous times. The calculation is carried on until the transient effects, due to the initial change in drive currents, die out. Figure 4.4 shows an example for $\hbar\omega_L/4\Delta \approx 0.45$, the normalized energy of the 496-μm-laser line (assuming a superconducting gap energy of 2.8 mV). Both the instantaneous voltage (solid line) and the average voltage (dashed line) are plotted as functions of time. Figure 4.4(a) is for a junction biased on the first laser-induced step, so that the current is periodic at the laser frequency, and the average voltage is approaching the constant value of 1.25 mV (0.45 $\times$ 2Δ/e). Figure 4.4(b) shows similar results for a dc bias not on a step. In this case the voltage is not periodic and the average voltage is approaching $\sim$ 0.65 2Δ/e, intermediate between the first and second steps. By monitoring quantities
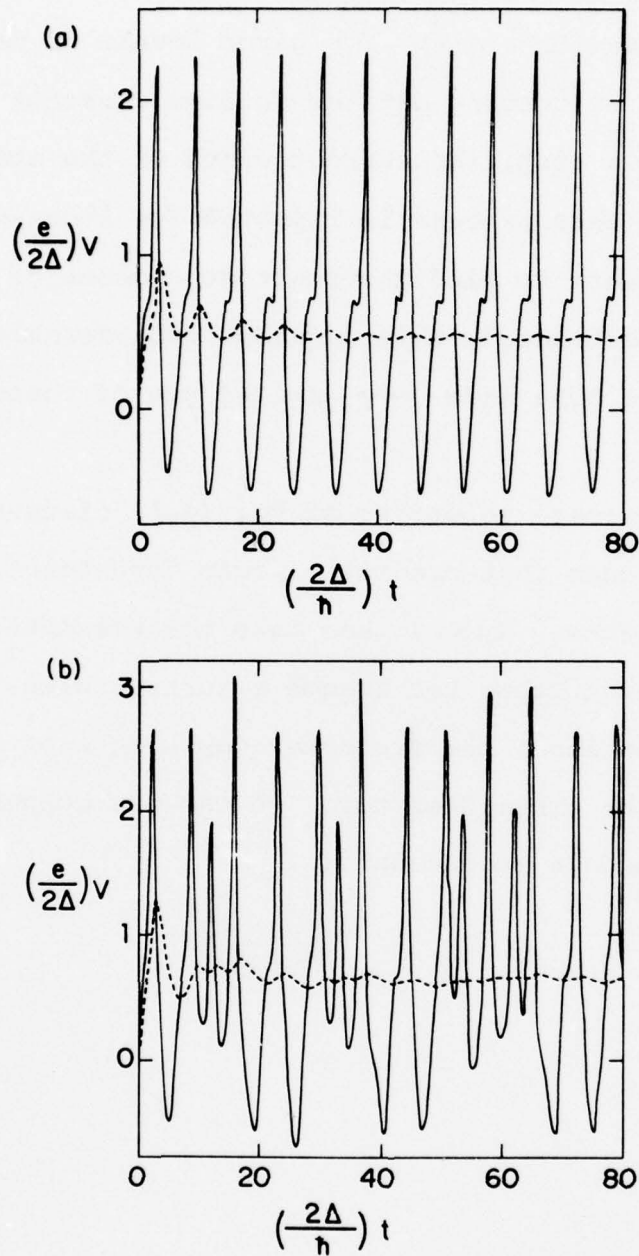
Fig. 4.4 Computer calculations using the frequency-dependent theory for a junction with ac and dc current biases. The ac source has a magnitude of $0.5(2\Delta/eR)$ and a frequency of $0.90(2\Delta/h)$. Both the instantaneous (solid lines) and the time-average (dashed lines) voltages are shown. The dc bias level is (a) on the step so the average voltage is approaching $0.45(2\Delta/e)$, and (b) between the first and second steps so the average voltage is approaching $0.65(2\Delta/e)$.

such as these, it is possible to determine whether or not the junction is biased on a step, for given levels of dc and ac currents. Then, by tracing out the dc bias currents that put the junction on a step, the current width of the step can be determined. This process is repeated for successively increasing laser powers to find the power dependence of the current width. Unfortunately this requires considerable computer time, so we have made only limited use of these calculations.

The four approximate solutions of Eq. (4.1) discussed above are the only ones that predict a power dependence for the step current-widths. Two of them make the assumption of a voltage bias, the other two assume a current bias. One of each bias type includes the frequency dependence of the Josephson effect, the other does not. We can now compare these theoretical models to our data.

CHAPTER V

FREQUENCY DEPENDENCE OF THE JOSEPHSON EFFECT

5.1 Josephson-Step Power Dependence

In order to obtain I_1^{max}/I_c, we need to measure the
power dependence of the steps induced by each laser line.
For this, our raw data consists of a series of traces of dc
I-V curves, each taken with a different incident laser power.
A typical example is shown in Fig. 5.1 for an I-V curve with
no incident power, and with increasing amounts of 496 μm radi-
ation, which induces constant-voltage steps at 1.25 mV
intervals. We always used high-quality junctions for these
experiments, and were always able to see seven or more steps
with the 496-μm-laser line. In fact, we have been able to
see steps up to the 10th harmonic at 12.5 mV using only this
rather insensitive dc detection technique.

A composite plot of the power dependence of the critical
current and eight steps induced by 496 μm radiation is shown
in Fig. 5.2, with data from five different point contacts
having resistances between 50 and 170 Ω. The half-widths of
the experimentally measured steps are normalized to the criti-
cal current at zero power, and are plotted as functions of
the square root of the laser power. The power measurements
are scaled once for each junction to account for its coupling
efficiency. The data plotted in Fig. 5.2 show that our high-

79
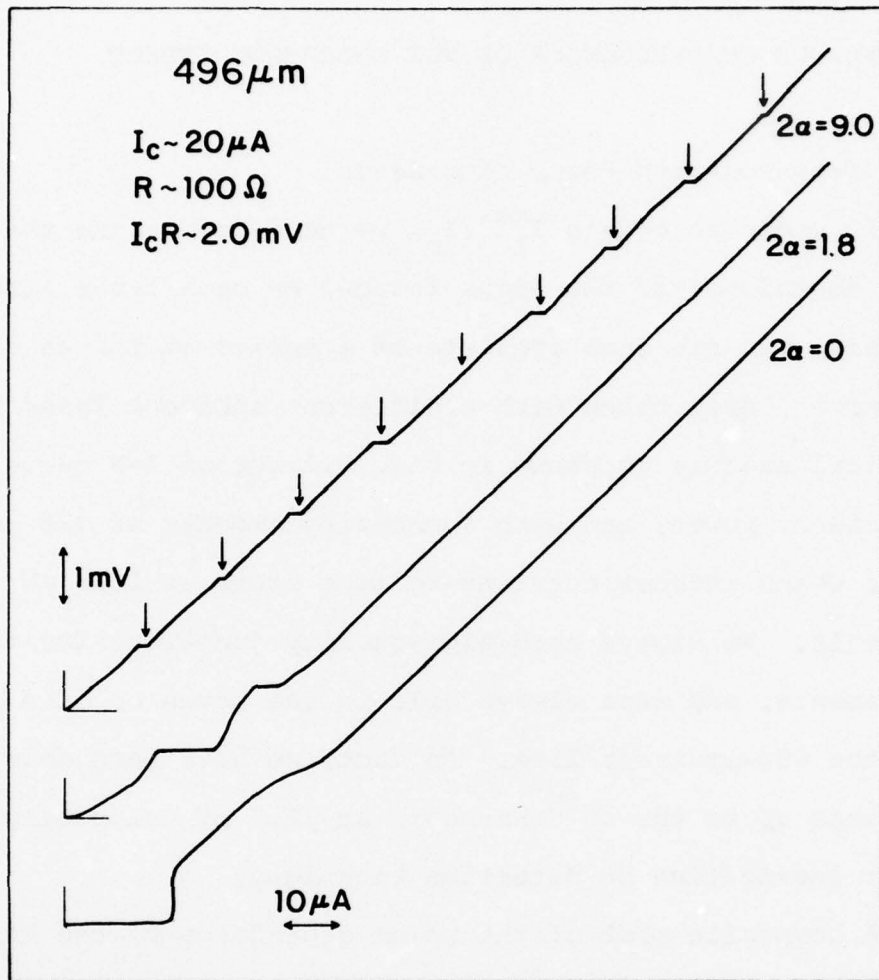
Fig. 5.1   Typical dc I-V curves at increasing laser powers.
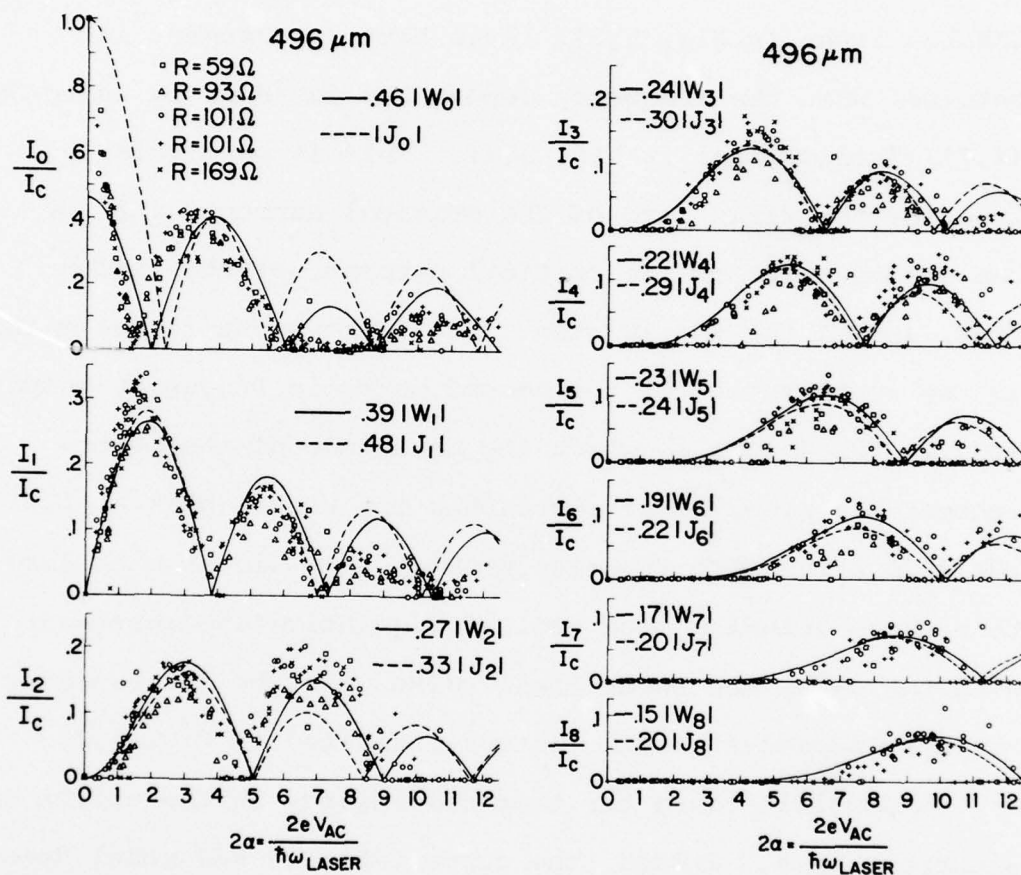
Fig. 5.2 Normalized step-width behavior as a function of induced 496-μm-laser voltage, compared to the Bessel functions (J), and the frequency-dependent Werthamer theory (W). This is a composite plot made from the data of five different junctions.

quality point contacts are <u>very</u> consistent from junction to junction in their high-frequency behavior, as they were in the shape of their dc I-V curves.

The shape of the power-dependence data is reasonably well described by the Bessel-function behavior of Eq. (4.3), (dashed lines in Fig. 5.2). Even better agreement is obtained when the frequency dependence is added by using Eq. (4.7), (solid lines in Fig. 5.2). This is particularly true for the first zero of the critical current, and for the second humps of the critical current, of the second step, and of the fourth step. The improvement is due mainly to the contribution of the second harmonic frequency component at 1.21 THz (2.5 mV), where the magnitude of the super-current has risen as it approaches the Riedel peak at 1.35 THz (2.8 mV). Both theories predict step widths much larger than those actually observed. For quantitative agreement with the data, the theoretical values must be decreased by the step-dependent scale factors indicated in Fig. 5.2.

A possible cause for this discrepancy is the effect of a current bias. Indeed, the current-biased RSJ model does predict a reduction in the step size in approximate agree-ment with that observed. However, Ω is large enough (~ 0.6 for a typical $I_c R$ of 2.0 mV) that the <u>shape</u> of the current-biased RSJ curves does not differ significantly from the voltage-biased Bessel-function behavior of Eq. (4.3). Thus we can not convincingly distinguish between the two models using the shape of the data.

If the data were better described by a current-bias model, the improvement should become more pronounced at lower Ω.[73] To check this, we went to a lower frequency, using the 1.22 mm line, which induces a fundamental step at 0.51 mV, so that $\Omega \approx 0.25$. Figure 5.3 shows the power dependence of I_n/I_c for the critical current and the first six steps. The normalized voltage amplitudes on the horizontal axis again have been obtained by scaling all of the data for a given point contact by a single factor which depends on its coupling efficiency. The shape predicted by Eq. (4.7) is shown by the solid lines in Fig. 5.3, and is in reasonably good agreement with the data. Again the theoretical step size must be scaled down by the factors indicated in the figure to obtain quantitative agreement. However, in this case the current-biased RSJ prediction does not do as well. It predicts a step size even smaller than observed. More importantly, its prediction of the shape of the power dependence, shown by the dotted lines in Fig. 5.3, is quite different from that observed. Thus it appears that the well-matched source impedance of the antenna is better described by a voltage-bias model in predicting the shape of the power dependence.

In Figure 5.3, the poorest agreement between the data and the voltage-bias theory is obtained for the critical current. In particular, the measured initial decrease and the subsequent first increase seem to be somewhat faster
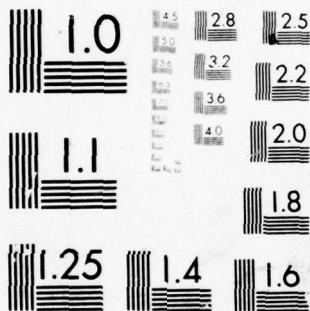
MICROCOPY RESOLUTION TEST CHART

NATIONAL BUREAU OF STANDARDS-1963-A

Fig. 5.3 Normalized step-width behavior as a function of 1.22-mm-laser-induced voltage, compared to the frequency-dependent, voltage-bias Werthamer theory (W) and RSJ model. This is a composite plot with data from three different junctions.

than predicted. Similar poor agreement is found for the power-dependence of I_0/I_c measured with 496 um radiation as shown in Fig. 5.2. The reason for this poor agreement is not known, although it is possibly related to the peculiar behavior of the I-V curves in the vicinity of the critical current that is always seen when these junctions are irradiated by low levels of laser radiation.[77] The effect of the radiation is not only to decrease I_0, but also to substantially decrease the initial dynamic resistance of the voltage onset, changing it from the very steep onset seen without incident radiation to a much more gradual one. This behavior is seen for all the laser frequencies we have investigated.

Comprehensive data such as that obtained at 1.22 mm and 496 μm could not be obtained at the other FIR wavelengths used (233 μm, 202 μm, 170 μm, and 119 μm). The fundamental steps of these laser lines are all at voltages near, or well above, the energy gap. Thus there are fewer observed harmonics to fit to the theory. In fact, for the remaining frequencies, the second step was generally very small, and the higher harmonics were usually not seen at all. Furthermore, at these frequencies we were unable to couple in enough power to reach the same high values of $2\alpha = \dfrac{2e\ V_{ac}}{\hbar\omega_L}$ that were reached at the lower frequencies. Operating at 496 μm, the laser power (measured at the laser output coupler) was ~10 mW, sufficient to obtain $2\alpha \approx 12$. However, 2α scales

as V_{ac}/ω_L, so that the power ($\sim V_{ac}^2$) required to reach the same 2α scales as ω_L^2. Thus, even though the output power at 119 μm was $\sim$80 mW, we would expect to reach values of 2α of only $\sim$5.5. In fact, our optics were considerably more lossy at 119 μm than at 496 μm, and the coupling to the antenna may not have been as good, so that we were only able to reach $2\alpha \sim 3$.

As a result of the low values of 2α attained and the associated lack of harmonics, there was insufficient structure in the power-dependence data to obtain a convincing fit to the theory. Figure 5.4 shows the power dependence of I_0/I_c and I_1/I_c for a typical junction exposed to 119 μm radiation, and fitted to the scaled shape of the voltage-bias theory of Eq. (4.7). As with the lower frequencies, the low laser-power behavior of I_0 resulted in a poor fit to the theory. Thus, the only reliable structure in the data useful for a fit to the theory is the first hump of I_1.

We also attempted similar measurements using the 71 μm line of CH_3OH. However, there was not enough laser power available to see the first step at 8.75 mV. The ω_L^2 dependence of the power required means that a factor of $\sim$3 increase in power over that available at 119 μm is necessary to reach comparable values of 2α for equal coupling efficiencies. However, both the losses in the optics and even the attenuation in atmosphere are quite severe at 71 μm. Thus, although we estimate that we had at least several mW power at 71 μm, this was not sufficient with the coupling scheme used.

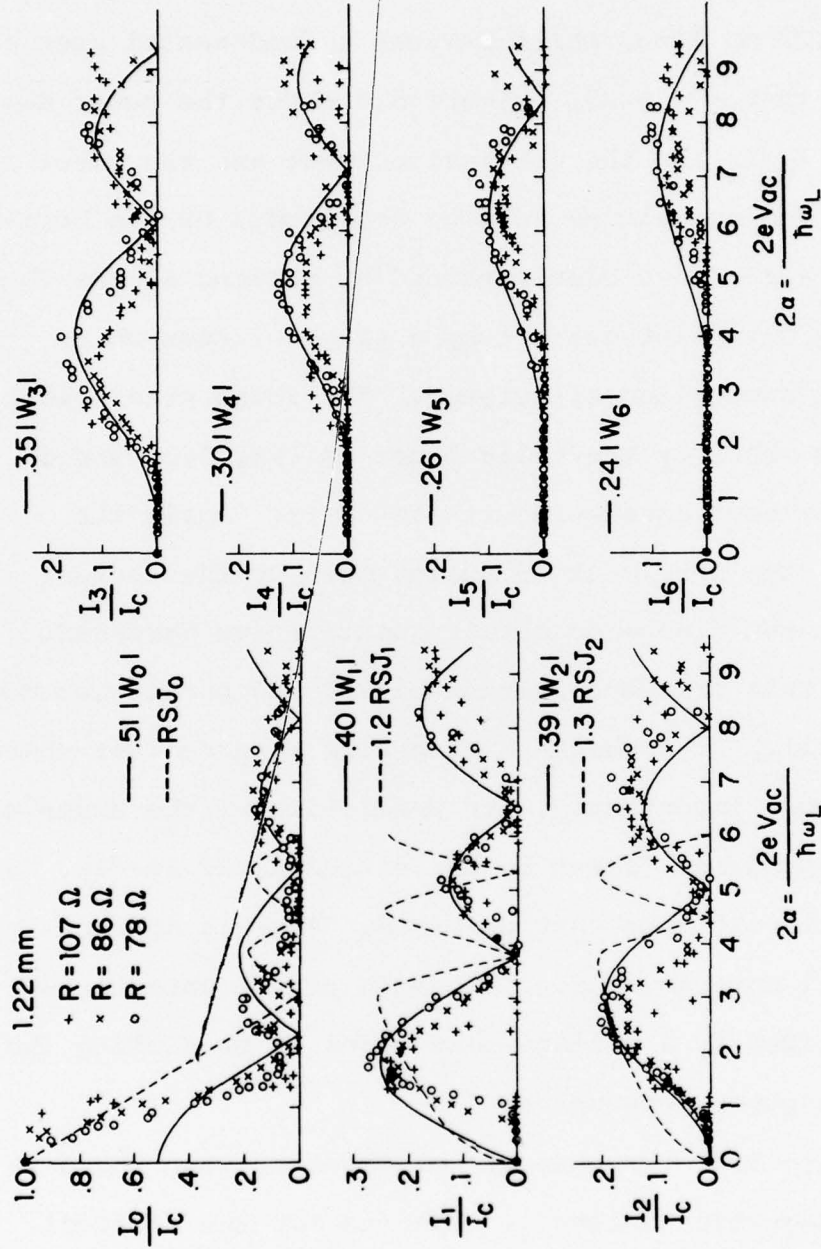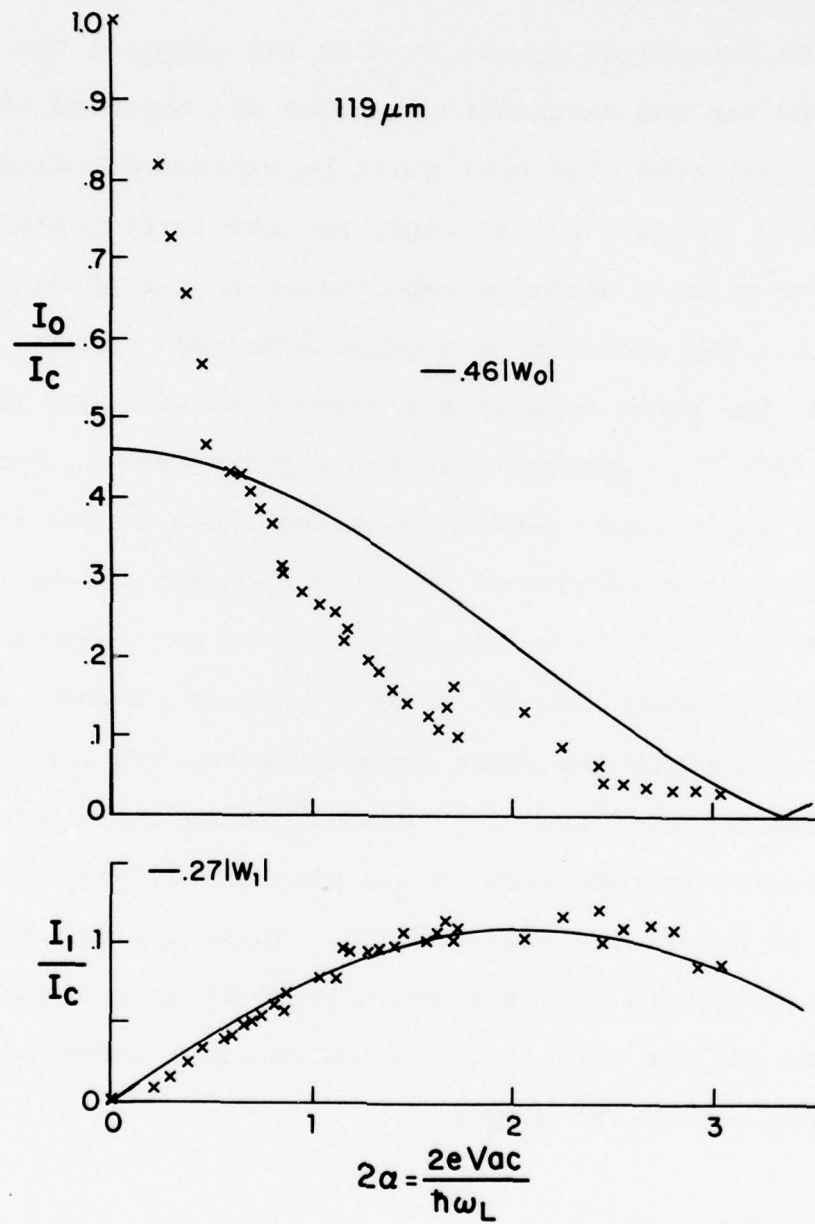Fig. 5.4   Normalized step-width behavior as a function of 119-μm-laser-induced voltage, compared to the frequency-dependent, voltage-bias Werthamer theory.

When the data at all the wavelengths is considered as a whole, the voltage-bias theory of Eq. (4.7) appears to give quite reasonable agreement with the _shape_ of the data. The reason for the discrepancy between the observed step _size_ and that predicted must still be explained. Since the frequencies involved are so high, we have investigated the effects of a small shunting capacitance on the predicted step size. The addition of a capacitive roll off has little effect on the power dependences calculated with Eq. (4.7) so long as $(RC)^{-1}$ is greater than the gap frequency. Larger values of capacitance remove the effects due to the inclusion of the frequency dependence and give a poorer fit to the 496 μm data. Smaller values do not cause any reduction in the predicted step widths. We have used an analogue simulator[78] to calculate the power dependences within the RSJ model with the addition of a small shunting capacitance.[79] We again find no reduction in the step sizes, although the effects of noise were not included. Thus, the evidence available suggests that the capacitance is indeed small enough to neglect entirely. We now consider other effects that might reduce the step size.

5.2 Heating

Heating has been proposed as a mechanism which reduces the critical current, and hence the step widths. Tinkham et al.[6] have treated in detail the case of a metallic junction

of the point-contact geometry. They find an exponential decrease in the step widths as the total dissipated power P is increased, with

$$I_n \propto e^{-P/P_0} \qquad (5.1)$$

where P_0 is predicted to be ~ 10 μW for a typical metallic Nb point contact. We can calculate P for a given laser power using the good fit of the power dependences of the step widths to the voltage-bias model to obtain the normalized laser-induced voltage in the junction, 2α. Combining this with the power dissipated by the dc bias current

$$P = P_{dc} + P_{ac}$$

$$= \frac{V^2}{R} + \left(\frac{\hbar\omega_L}{2e}\right)^2 \frac{(2\alpha)^2}{2R} \qquad . \qquad (5.2)$$

For a typical 100 Ω junction, biased at the 5.22 mV step induced by 119 μm radiation, Eq. (5.2) gives $P \approx 1.5$ μW for $2\alpha = 3$, the maximum value reached in these experiments. For the eighth harmonic induced by 496 μm radiation at 10 mV, $P \approx 2$ μW for $2\alpha = 12$. These values of P suggest that heating will have only a small effect, mainly on the high-voltage steps, at higher laser-induced powers. It should cause a maximum reduction in the step size of only $\sim 20\%$. We now present further evidence supporting this.

The very pronounced gap structure on the I-V curves can be used as a local thermometer to measure the temperature, T, roughly a coherence length, ξ, away from the center of

the active region of the point contact.[4] The laser-induced
Josephson steps can obscure this structure unless the
voltage of the first step is above the gap voltage. It is
then possible to measure the rise in temperature over the
bath, $T-T_b$, due to the laser-induced power which is determined
using Eq. (5.2) and the power-dependence fit of the step
widths. Figure 5.5 shows $T-T_b$ due to the total dissipated
power for increasing levels of 170 μm radiation. The width
of the gap structure makes it difficult to determine an exact
gap voltage, especially at higher laser powers where the
shape becomes somewhat less pronounced. This leads to con-
siderable scatter in the data of Fig. 5.5. The gap voltage
was taken as the voltage of the minimum R_D in the gap struc-
ture. The corresponding temperatures T were obtained from
the measured temperature dependence of the energy gap of
Nb/Nb tunnel junctions,[51] which have low-temperature gap
voltages in good agreement with those of our point contacts.

Using Fig. 5.5, we can obtain a measure of some of the
experimental parameters important in the heating theory. In
the low heating limit, Tinkham et al.[6] find that

$$T - T_b = \frac{P}{\Omega K \xi} \tag{5.3}$$

where K is the thermal conductivity and Ω is the effective
solid angle for the three-dimensional cooling of the active
region of the contact. From the slope of the solid line in
Fig. 5.5, $\Omega K \xi \approx 1 \mu W/^o K$. These are the only unknown quantities
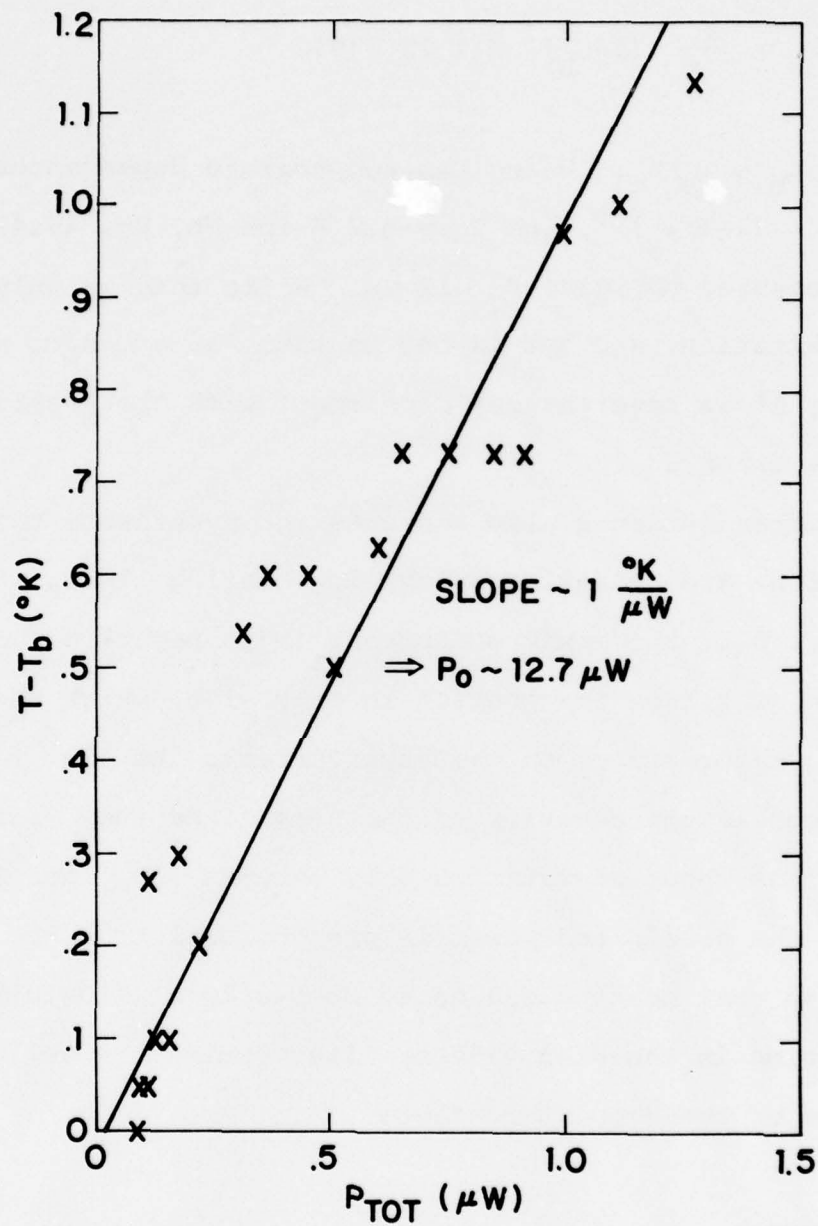
Fig. 5.5   Temperature rise in the vicinity of the contact as the dissipated power is increased with 170-μm-laser radiation. The gap voltage is used as a local thermometer.

in the expression for P_0,

$$P_0 = \frac{1}{\sqrt{2}} \ (1-t_b^2)^{\frac{1}{2}} \ K(T_c)T_c\xi(0)\Omega \qquad (5.4)$$

where $t_b = T_b/T_c$. Using the temperature dependences $K \propto T$ and $\xi \propto (1-T/T_c)^{-\frac{1}{2}}$, and $T_c \approx 9.2$ K for Nb, Eq. (5.4) and the measured $K\Omega\xi$ give $P_0 \sim 12$ μW. While this is only an approximation, and should not be taken as an exact measure of P_0, it is nevertheless consistent with the predictions of the theory.

Other evidence also supports the hypothesis that these junctions are operating in the low heating limit. As shown in Fig. 5.5, the maximum increase in temperature a coherence length away from the contact is only ~ 1 K, which should not have a major effect on the supercurrent. We also find very consistent behavior of the normalized step widths for junctions whose resistances vary between ~ 30 Ω and 200 Ω, while the dissipated power is proportional to $1/R$. Thus we believe that heating causes at most only a $\sim(10\text{-}20)\%$ reduction in the step widths, illustrating the well-cooled nature of these point contacts.

5.3 Noise

Fluctuations in the phase due to noise can have an important effect on the shape of the step, causing the edges to be rounded and the dynamic resistance of the step center to be greater than zero.[80] This can have a significant

effect on the measured current width of the step. The only available detailed theoretical treatment of the effects of noise on the shape of the step is within the RSJ model. Within this approximation, the unrounded step has the same characteristic hyperbolic shape of the dc I-V curve.

Since the dc I-V curve of our junctions is so highly structured, it is quite likely that the unrounded step shape is also more complicated than the relatively structureless RSJ prediction. In fact, the measured step shape seems to depend on where it is on the I-V curve. Figure 5.6 shows the shape of the fundamental step induced by a number of different FIR laser wavelengths at various voltages. The steps are superimposed on a typical dc I-V curve with no incident radiation. Although each step is from a different junction, all the dc I-V curves had the same characteristic shape and the current width of each step shown is normalized to its own I_c. The figure shows how the step shape seems in some sense to mimic the underlying structure on the dc I-V curve at that voltage. The 0.5 mV step (1.22 mm radiation) occurs on the very steep initial voltage rise, and the sides of the step also show this high dynamic resistance R_D. The steps at 1.25 mV (496 μm), 3.65 mV (170 μm), and 5.22 mV (119 μm) all occur on portions of the I-V curve that do not have a lot of extra structure or high R_D, and these steps all have shapes somewhat closer to that of the RSJ model. The step at 2.64 mV occurs on the gap structure and is
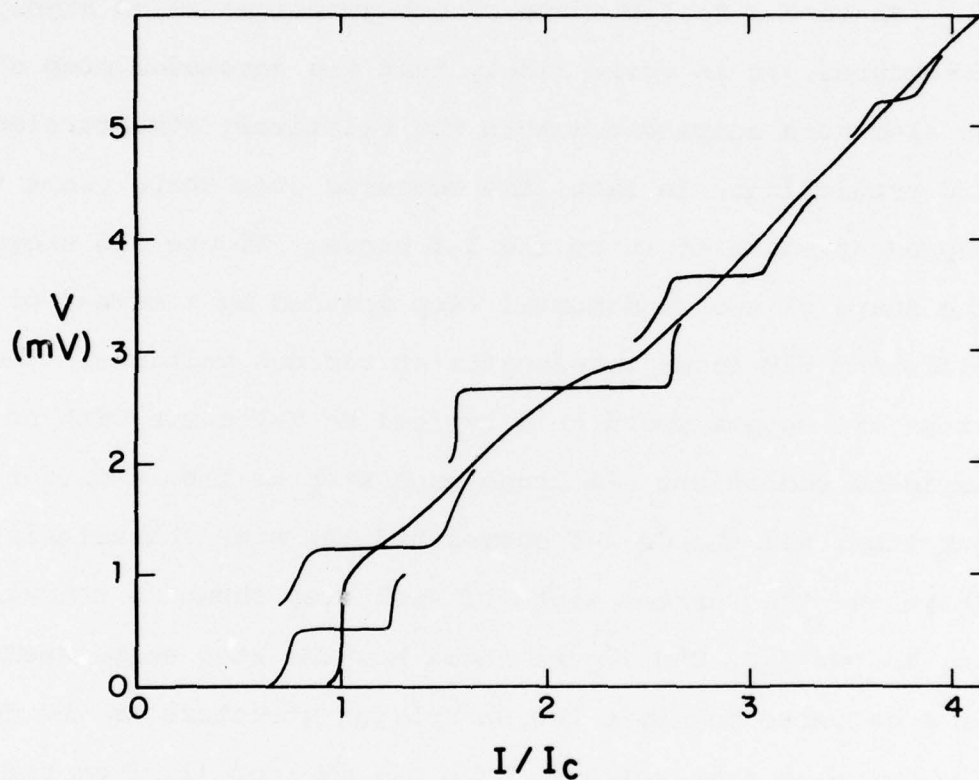
Fig. 5.6   The variation in the shape of the step with its voltage. Each step is taken from a separate high-quality I-V curve and is normalized to its own I_c.

They are superimposed on a typical I-V curve to show the underlying shape.

enhanced due to the effects of the Riedel peak. Its shape is quite different from the other steps and has a very large dynamic resistance on either side. Thus, the adequacy of the RSJ model in describing the shape of the step depends somewhat on the voltage of the step.

Despite the highly structured shapes of the experimentally observed steps, the RSJ model is still a reasonable first approximation, especially for a description of the effects of noise rounding. We have fitted the shape predicted theoretically to that measured in an attempt to correct for the effects of noise rounding. The predicted shape of the nth step can be written as[81]

$$v_1 = \frac{\frac{1}{2} R_D i_0 \ \sinh\left(\frac{\pi i_1}{i_0}\right)}{\int_0^{\pi/2} \cosh\left(\frac{2y i_1}{i_0}\right) I_0\left[\left(\frac{2I_n}{i_0}\right) \cos y\right] \ dy} \tag{5.5}$$

where $\quad i_0 = \dfrac{2e k_B T_{eff} R_D I}{\hbar V}$.

Here I, V, and R_D are respectively the current, voltage, and dynamic resistance at the step center in the absence of radiation, while i_1 and v_1 are respectively the current and voltage along the induced step, measured from its center. I_0 is the modified Bessel function, and e, k_B, and $\hbar$ have their usual meanings. The effective noise temperature, T_{eff}, is not the bath temperature, because of the heating in the point contact.[6] Thus, we must use a two parameter fit in T_{eff} and I_n, the current half-width of the step in the absence of noise rounding.

The value of the parameter $R_D I/V$ in Eq. (5.5) depends on the position of the step on the I-V curve. Within the RSJ model, this accounts for the underlying shape of the dc I-V curve. At low step voltages, where the underlying R_D is larger, the effects of noise are more pronounced. On our I-V curves, $\frac{R_D I}{V}$ ~1 for all the steps except the one induced by 1.22 mm radiation. We do not see an enhancement of the effects of noise at the 0.51 mV step. Instead, the fit to the RSJ model is the poorest at this voltage.

An example of the type of fit we obtain is shown in Fig. 5.7. The data, shown as the crosses, are the fourth harmonic of the 496-μm-laser-induced step at 5.0 mV, and the experimentally measured current half-width of the step was 2.1 μA. The solid lines are the calculated step shapes using Eq. (5.5). The fits shown in each figure use the value of I_n indicated, and are calculated for various values of T_{eff}. The best fit is for I_n ~ 3.5 $\pm$ 0.5 μA and T_{eff} ~ 15 $\pm$ 5 K. The accuracy of the fit is sufficient to obtain a reasonable correction to the step widths to account for the effects of noise rounding. As shown by the example in Figure 5.7, these corrections can be quite substantial.

5.4 Frequency Dependence of the Josephson Effect

We are now in a position to measure the frequency dependence of the Josephson effect. As discussed in Section 4.2, we use only the results from the fundamental step, which
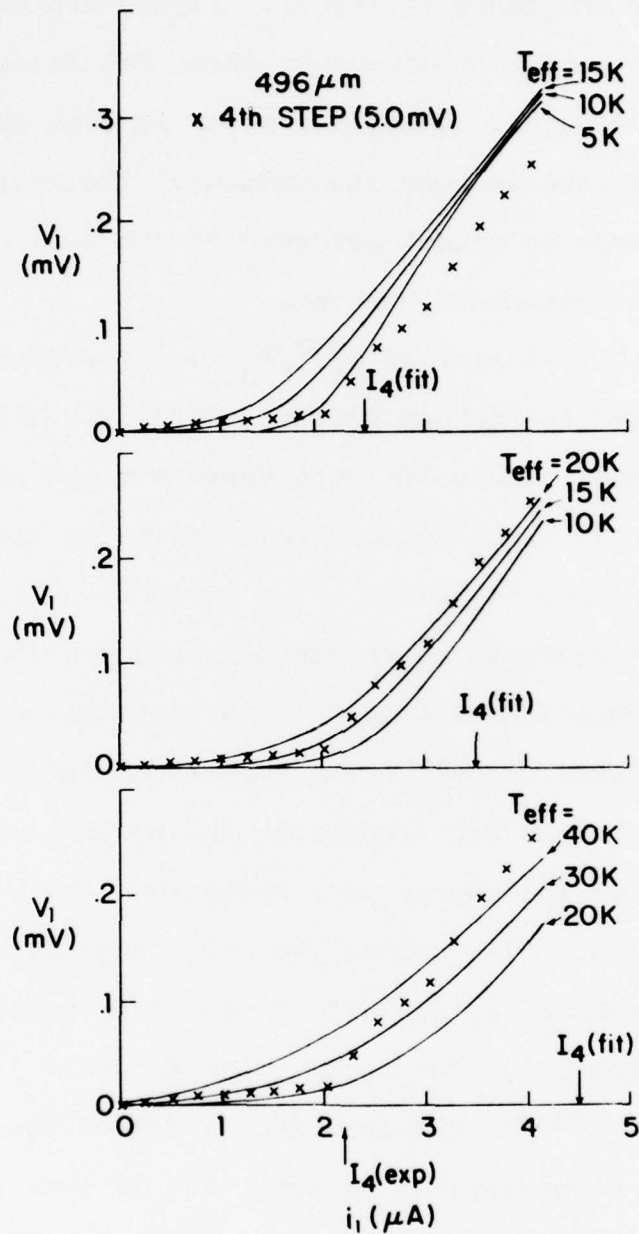
Fig. 5.7   Two parameter fit for the effects of noise rounding. The crosses are data showing the 4th step, at 5.0 mV, induced by 496 μm radiation. The solid lines are the calculated noise-rounded RSJ shape using Eq. 5.5 in the text. Each figure is for a different fitting value of I_n, the unrounded step width, and shows the shape for three effective noise temperatures.

is most closely related to the strength of the Josephson effect at that frequency (voltage). Figure 5.8 shows a typical dc I-V curve irradiated by three FIR laser lines of decreasing wavelength. The laser power in each case is such that step size is near its maximum. The decreasing size of the steps is direct evidence of the roll off of the strength of the Josephson current.

Figure 5.9 is a plot of I_1^{max}/I_c as a function of voltage, normalized to the gap voltage, $2\Delta/e$, for all of the laser lines used. The solid dots represent the largest value of I_1^{max}/I_c actually measured, while the error bars represent the range of values after corrections have been made for the effects of noise rounding and heating as described in the previous sections. The vertical error bars represent the uncertainty in the noise-rounding fit, while the horizontal error bars represent the uncertainty in the exact voltage of the energy gap, reflecting the width of the structure on the dc I-V curve. We had enough laser power to reach the maximum of I_1 for all of the steps except the one at $\frac{eV}{2\Delta} \approx 1.1$ (202 μm). The datum shown for this frequency is an estimate of I_1^{max}/I_c obtained from a fit of Eq. (4.7) to the available power-dependence data, and is thus a somewhat less accurate result (hence the larger error bars on the corrected value).

The solid line in Fig. 5.9 is the prediction of the voltage-bias, frequency-dependent theory calculated with
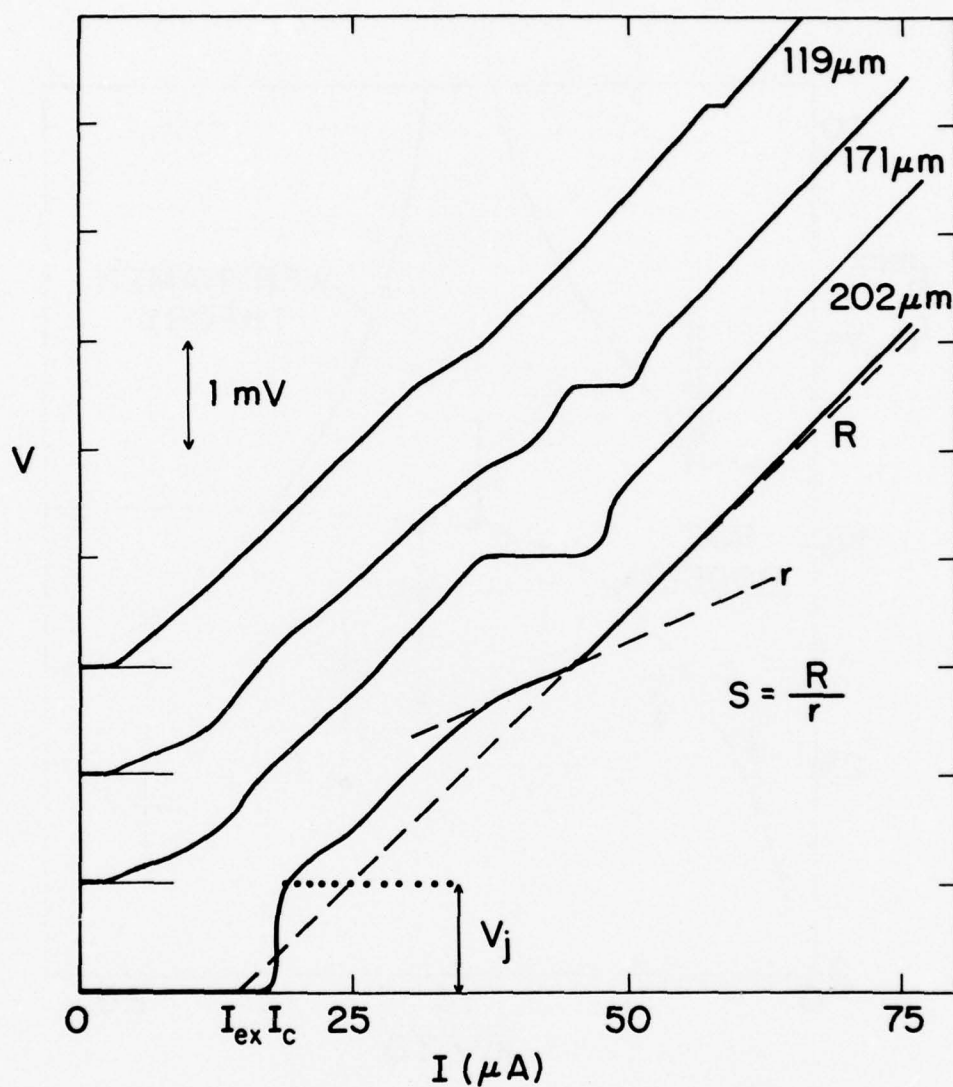
Fig. 5.8 Dc I-V curves of a typical high-quality junction. The lowest curve is with no incident radiation, while the remaining curves show the Josephson steps induced by radiation at three different FIR wavelengths.
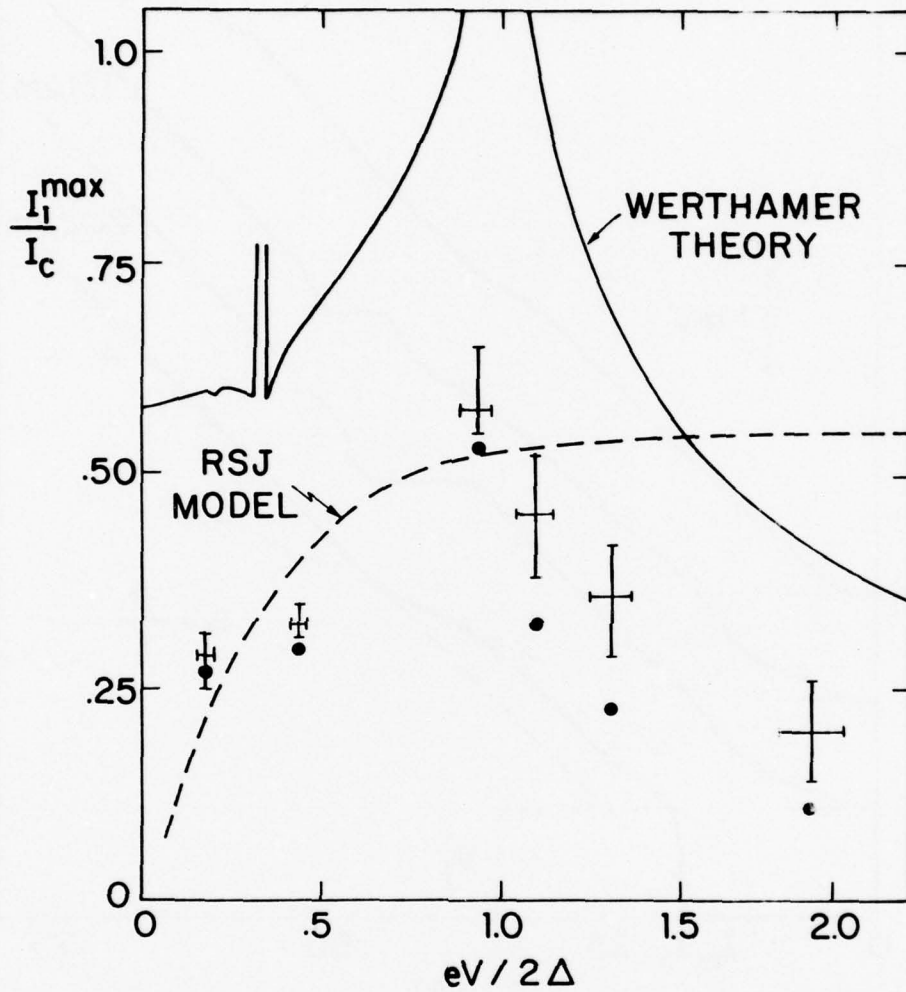
Fig. 5.9   The voltage dependence of the ac Josephson effect.
The maximum width of the fundamental Josephson step normalized
to the critical current is plotted against the step voltage
normalized to the energy gap.   The dots represent the measured
data, while the error bars represent the range of values
after they are corrected for the reductions due to noise and
heating.   The horizontal error bars reflect the uncertainty
in the energy-gap voltage.   The solid curve is the voltage-
bias FDSC (Werthamer) theory result; the dashed curve is the
current-bias RSJ result.

Eq. (4.7). The singularities at the gap and at one third
of the gap would be rounded off, but the details of this
would depend on the experimental conditions. The data follow
the shape of the theory, peaking near the gap and rolling
off above the gap. However, the magnitude of the data is
consistently below that of the theory, even after the adjust-
ments for noise rounding and heating are made.

Below the energy gap, a reduction in I_1^{max}/I_c is
expected if the junction is current-biased rather than voltage-
biased. The dotted line in Fig. 5.9 shows the reduction
expected within the RSJ model. We have also investigated
the effects of a current bias on the prediction of the
frequency-dependent theory at a voltage $\frac{eV}{2\Delta} \approx 0.45$, correspond-
ing to the 496-μm-laser-induced step. Using the computer
calculations described in Section 4.2, we obtain I_1^{max}/I_c
≈ 0.35, in good agreement with the experimental value. Thus
it is tempting to attribute the decrease simply to current-
bias effects. However, as shown previously, this is not
really accurate. At $\frac{eV}{2\Delta} \approx 0.18$ (1.22 mm line), where the
effect of a current bias should be more pronounced, the
measured I_1^{max}/I_c is larger than predicted by the RSJ model,
and the shape of the step power-dependences are better
described with a voltage-bias approximation. It might be
possible that the step width is reduced because of a current-
like biasing condition, even though the power dependence
is better described by a voltage bias. In fact, neither a

simple voltage- nor current-bias approximation is a completely
accurate description of the experiment, and a more realis-
tic theoretical handling of the source impedance would be
desirable.

Although a current-bias approximation predicts a de-
crease in I_1^{max}/I_c below the gap, the values above the gap
rapidly approach those of a voltage-bias approximation.
This is shown by the RSJ curve in Fig. 5.9, which rapidly
converges above the gap on the simple voltage-bias prediction
of Eq. (4.3), $I_1^{max}/I_c \approx 0.58$. Thus the effects of a current-
bias approximation can not explain the discrepancy between
the data and the theory above the gap, although a more
realistic handling of the source impedance might improve the
agreement.

It is also possible that there could be a more rapid
roll off than predicted by the Werthamer theory. At these
high frequencies, the Josephson period is shorter than the
characteristic times of the superconductor (e.g. the Ginzburg-
Landau time, $\tau_{GL} \approx \frac{\pi \hbar}{8k_B(T_c-T)}$). This may affect the dynamics
of the currents in the junction and cause the smaller steps.
The effects of the finite relaxation time of the order para-
meter have been examined[60,82] using time-dependent Ginzburg-
Landau (TDGL) theory, and have been shown to offer a possible
explanation of the excess current characteristic of our dc
I-V curves. Finite relaxation times have been included
phenomenologically within an analogue simulation of the

RSJ model to calculate the high-frequency roll off of the Josephson effect.[83] However, to fit the data on indium microbridges, this RSJτ model required a relaxation time two orders of magnitude larger than τ_{GL}, and the internal consistency of this model has been questioned.[82] It would seem desirable to extend the more fundamental type of TDGL calculations to include an rf source and to investigate more thoroughly the effects of a finite relaxation time, which may play a role in explaining our experimental data.

CHAPTER VI

POTENTIAL APPLICATIONS

6.1 Low-Power Laser Measurements

Josephson point-contact devices may hold great promise
for use as detectors and mixers in the FIR region of the
spectrum. While our work has focused on the more fundamen-
tal characteristics of our high-quality junctions, their
potential for use as practical devices should also be
examined. In order to characterize further the high-frequency
performance of our junctions, we have investigated their
voltage response to low-level laser radiation, when the dc
bias is in the vicinity of the incipient first step.
Frequency-selective, incoherent detectors operated in this
mode have been proposed,[84-86] although much better
sensitivity has been attained with Josephson-effect mixers
using external local oscillators.[87,88]

We have been primarily interested in the intrinsic
response of the junction itself, and have not addressed
the very important practical issue of optimizing the coup-
ling efficiency of the point contact to the laser radiation.
All of our measurements are referred to the power actually
coupled into the junction. This was done as follows.
Initial measurements on each junction were made at high

104

enough laser powers to induce constant-voltage steps on the dc I-V curves. In Section 5.1, we have shown that the power dependence of the current half-widths of these steps are reasonably well described by the simple voltage-bias approximation of Werthamer's frequency-dependent theory.[58] By fitting the data for each junction to the theory, we were able to calibrate our external power meter in terms of $2\alpha = 2eV_{ac}/\hbar\omega_L$, the normalized, laser-induced voltage in each junction. From this we calculated the induced power in the junction,

$$P = \frac{V_{rms}^2}{R} = \frac{V_{ac}^2}{2R}$$

$$= \left(\frac{\hbar\omega_L\alpha}{e}\right)^2 \frac{1}{2R} \quad .$$

(6.1)

In this way, we could refer all measurements to the power actually coupled into the junction.

In the limit of very small laser power, the noise-rounded RSJ model predicts[84] the voltage response of the junction in the vicinity of the incipient step to be

$$v = \frac{- i_1}{i_1^2 + i_0^2} \ P \ ,$$

(6.2)

with the characteristic noise current

$$i_0 = \frac{2ek_B T_{eff} R_D I}{\hbar V} \quad .$$

(6.3)

Here, I, V, and R_D are respectively the dc current, dc voltage, and dynamic resistance at the step center in the absence of radiation, while i_1 is the dc bias current measured from the step center. Equation (6.2) predicts a resonant response that changes sign at the step center and peaks at a bias current i_0 on either side. The magnitude of the peak response is also predicted to be linear in the laser power coupled into the junction.

To make these measurements, the output of the CO_2 laser was chopped at 450 Hz with a 50% duty cycle and the voltage response to the FIR laser was detected synchronously. A typical measured response is shown in the inset of Fig. 6.1 for $\sim 3.7 \times 10^{-11}$ W of 604 GHz (496 μm) laser radiation coupled into the junction. This particular junction had R_D = 70 Ω and I = 21 μA at the 1.25 mV step. The voltage separation between the two peaks implies $i_0 \approx 0.36$ μA, in reasonable agreement with the 0.25 μA predicted by Eq. (6.3) for T_{eff} = 5 K, the effective noise temperature obtained from a step-shape fit. In the inset of Fig. 6.1, the solid points show the response calculated using Eq. (6.2) with the height and width adjusted to fit the data. Good agreement with the theory is obtained for the shape of the response.

As the laser power is varied, the shape of the response and the value of i_0 remain the same, while, as shown in Fig. 6.1, the magnitude of the peak response, v_m, decreases linearly with decreasing laser power as predicted by the

Fig. 6.1   The peak voltage response, measured near the first step, as a function of the 496-μm-laser power coupled into the junction, for a 110 Ω high-quality point contact.   The inset shows the voltage response as a function of bias voltage for ~ 3.7 x 10^{-11} W coupled power.   The solid dots are the shape predicted by Eq. (6.2) in the text.

theory. However, the measured responsivity, S , is $\sim 8 \times 10^4$ V/W which is substantially less than the value predicted by the theory, $S = 1/2i_0 \approx 1.4 \times 10^6$ V/W. Our best measured responsivity at 600 GHz was $\sim 2 \times 10^5$ V/W, but was still less than the predicted value. The reason for this discrepancy is not understood. However, it is likely that the RSJ model cannot be used to make <u>quantitative</u> predictions at these high frequencies, where other frequency-dependent effects become important.

We have also tried to make these sorts of measurements at different FIR frequencies. Attempts to measure the responsivity using 245 GHz (1.2 mm) laser radiation were not successful. The laser-induced step at 0.51 mV occurs at the middle of the very steep voltage onset. The dynamic resistance was too large to maintain a stable enough dc bias with the current-bias network used, and we were unable to measure the resonant response at low laser-power levels and small step sizes. We were able to measure the resonant response around the 5.22 mV step induced by 2.52 THz (119 μm) laser radiation. As shown in Fig. 6.2, its shape was again well described by the RSJ prediction of Eq. (6.2). For a junction that had $R = R_D = 60\ \Omega$ and $I = 113\ \mu A$ at the step, the measured i_0 was 0.91 μA, compared to the 0.62 μA predicted by Eq. (6.3), using $T_{eff} = 15$ K, the noise temperature obtained from a step-shape fit. The response was also linear in laser power but the measured responsivity was only $S \sim 4 \times 10^2$ V/W, far below the value predicted for this i_0,
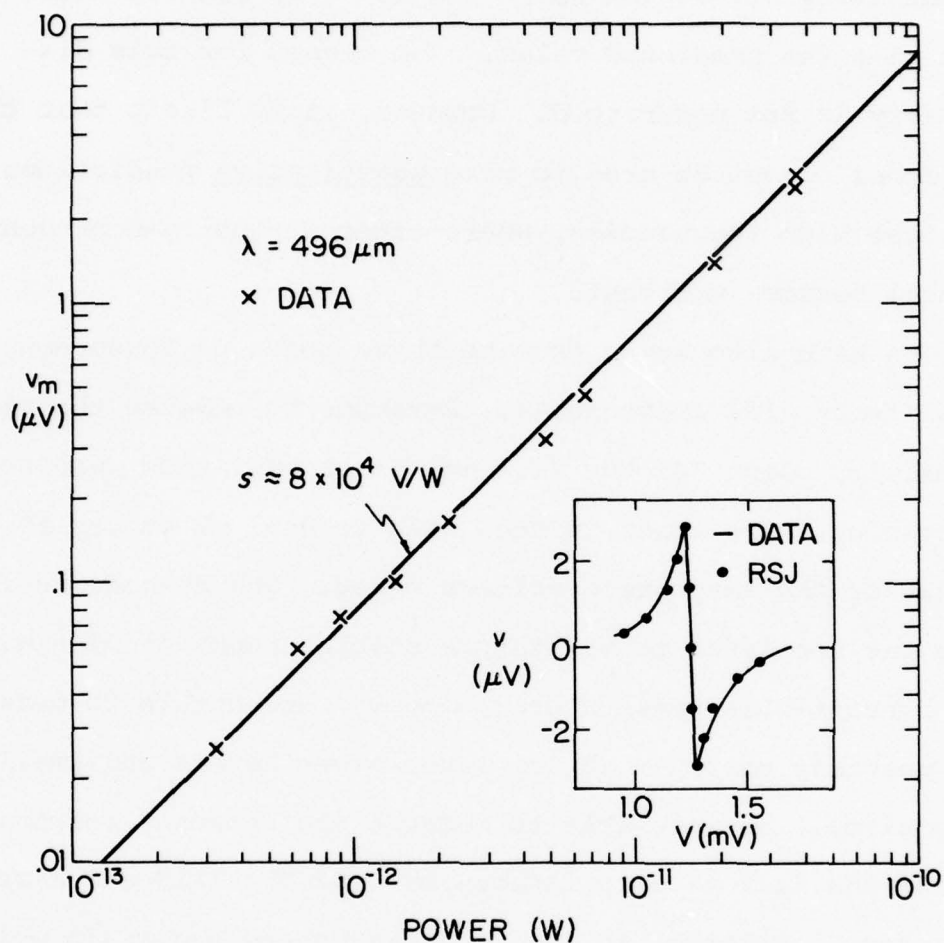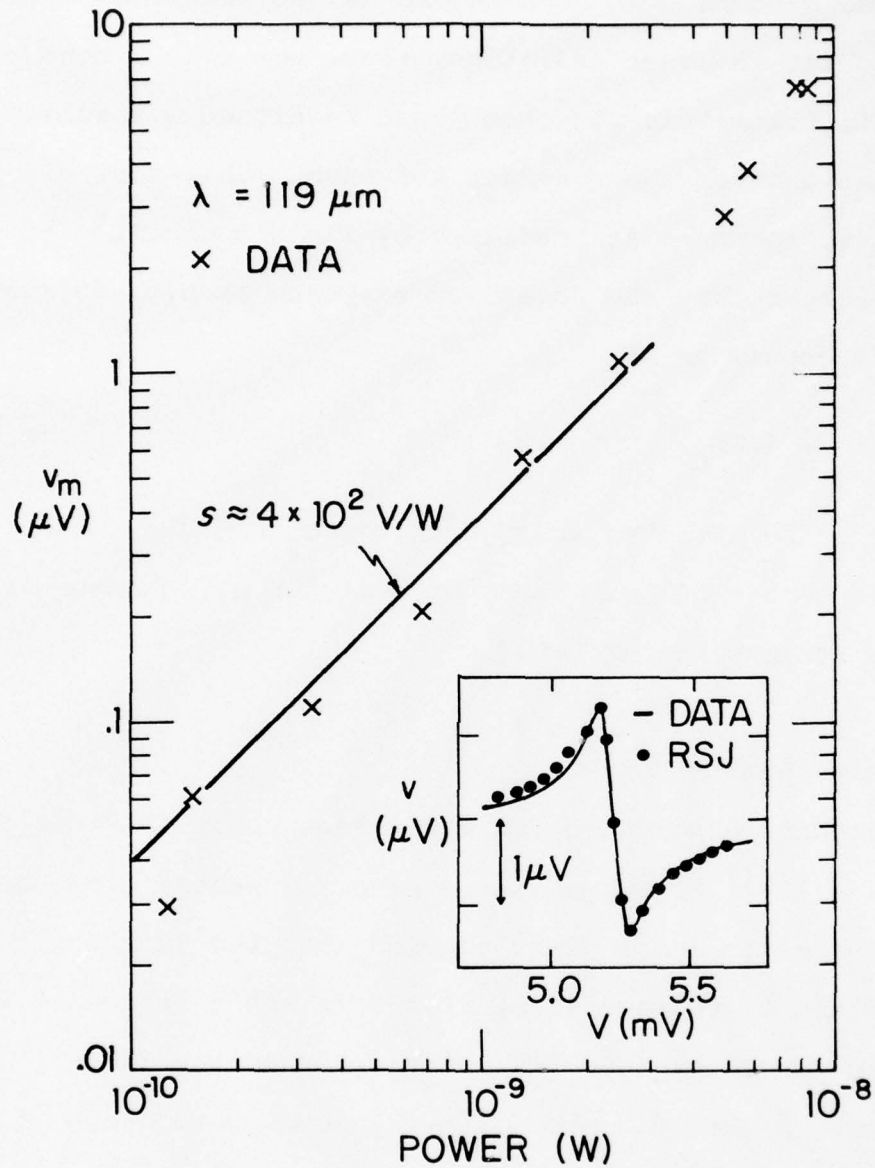
Fig. 6.2 The peak voltage response, measured near the first step, as a function of the 119-μm-laser power coupled into the junction, for a 60 Ω high-quality point contact. The inset shows a typical measurement of the voltage response as a function of bias voltage. The solid dots are the shape predicted by Eq. (6.2).

which is $S \approx 6 \times 10^5$ V/W. Thus the disagreement with the
RSJ model becomes even more severe as the frequency increases.
With the 119-μm-laser radiation, there was also a non-
resonant, bolometric response whose magnitude was somewhat
less than that of the resonant response. This sort of
bolometric response is predicted by Tinkham et al.[6] to
become larger than the Josephson response at high frequencies,
with the crossover at

$$f_c = \frac{e}{h} \; (2RP_0)^{\frac{1}{2}} \tag{6.4}$$

where $P_0 \approx 10$ μW. For this junction, $f_c \approx 6$ THz, which cor-
responds to $\lambda = 50$ μm. Thus, even at 119 μm, observable
heating effects are expected.

6.2   Noise Limitations

Our best observed noise equivalent power (NEP) at 604
GHz was $\sim 10^{-13}$ W/$\sqrt{Hz}$, measured with a 1 second time constant,
and referred to laser power coupled into the junction. It
was limited by voltage fluctuations in the junction at the
chopping frequency (450 Hz) which obscured the laser
response. Figure 6.3 shows the frequency dependence of the
voltage noise power spectrum, $S_V(f)$, for a 92 Ω junction.
It was measured at three different bias levels, and cor-
rected for the background noise level. Although there is
considerable scatter   in the data, the frequency dependence
appears to be approximately $1/f^2$. Data from other junctions
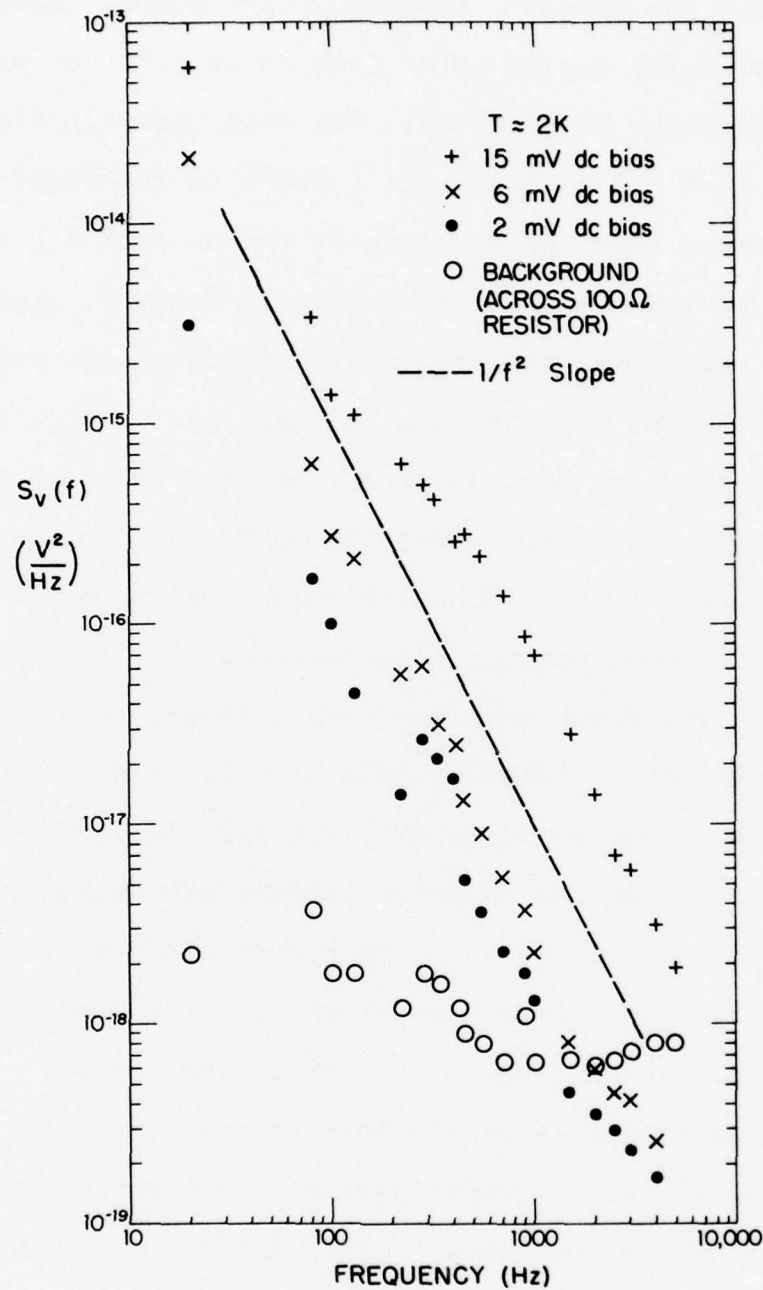
Fig. 6.3 The spectral density of the voltage fluctuations for a 92 Ω junction measured at three different bias-voltage levels. The data have been corrected for the background noise (circles), measured across a 100 Ω resistor. The dashed line shows a $1/f^2$ frequency dependence.

had similar amounts of scatter, but all seemed to have approximately the same f^{-2} frequency dependence. However, the level of $S_V(f)$ varied by as much as an order of magnitude from junction to junction. The data shown in Fig. 6.3 were taken at $T \sim 2$ K, below the λ-point of the liquid He bath, to ensure that the bubbling of the He bath did not contribute to the measured noise power. However, approximately the same level and frequency dependence was found at 4.2 K. At 450 Hz, we have also measured the voltage noise, V_N, as a function of bias voltage. We find that for bias voltages up to $\sim$ 3-5 mV, it depends on the dynamic resistance, with V_N/R_D approximately constant which corresponds to a voltage-independent <u>current</u> noise source. At higher bias voltages, V_N increases with the bias voltage, perhaps due to heating effects. Although this high level of fluctuations severely limits our measured NEP, the $1/f^2$ dependence of $S_V(f)$ suggests that the detector performance could be improved considerably by going to higher chopping frequencies.

The origin of both the magnitude and the frequency dependence of the observed $S_V(f)$ is not understood. The $1/f^2$ frequency dependence is unlike that observed for thin metallic films[89] or resistively-shunted Josephson tunnel junctions,[90] which both show a $1/f$ behavior of $S_V(f)$. More experimental measurements, over a wider frequency range, will probably be required for a complete understanding of the nature of these fluctuations.

Despite the large spectral density of the low-frequency voltage noise, its contribution to the linewidth of the Josephson radiation is relatively small. The linewidth, which determines the voltage separation between the two peaks of the resonant response in the RSJ model,[84] corresponds to ~25 μV for the 496 μm data described in the previous section. According to standard FM theory,[91] narrow-band, low-frequency noise contributes its full root-mean-square voltage deviation, $\overline{V^2}^{1/2}$, to the linewidth, while broad-band noise contributes less than its total $\overline{V^2}^{1/2}$ because of "motional narrowing." Nevertheless, the broad-band noise is still the major cause of the measured linewidth. The contribution from the low-frequency noise can be estimated by assuming a $1/f^2$ frequency dependence and a typical value of $S_v(f) \approx 10^{-16}$ V^2/Hz at 100 Hz (from Fig. 6.3). Integrating the spectral density, including frequencies down to 10^{-4} Hz, gives a contribution to the linewidth of less than 1 μV.

Other noise sources can become important at the relatively high levels of dissipated power that are achieved when the device is operating at FIR frequencies. The most important of these is heating.[6] As discussed in Section 5.3, a fit of the shape of the laser-induced step to the prediction of the noise-rounded RSJ model[80] yields T_{eff} at the step voltage. Using the 496-μm-laser-induced steps, we have measured T_{eff} as a function of bias voltage, and plot the results in Fig. 6.4. These data demonstrate a result that
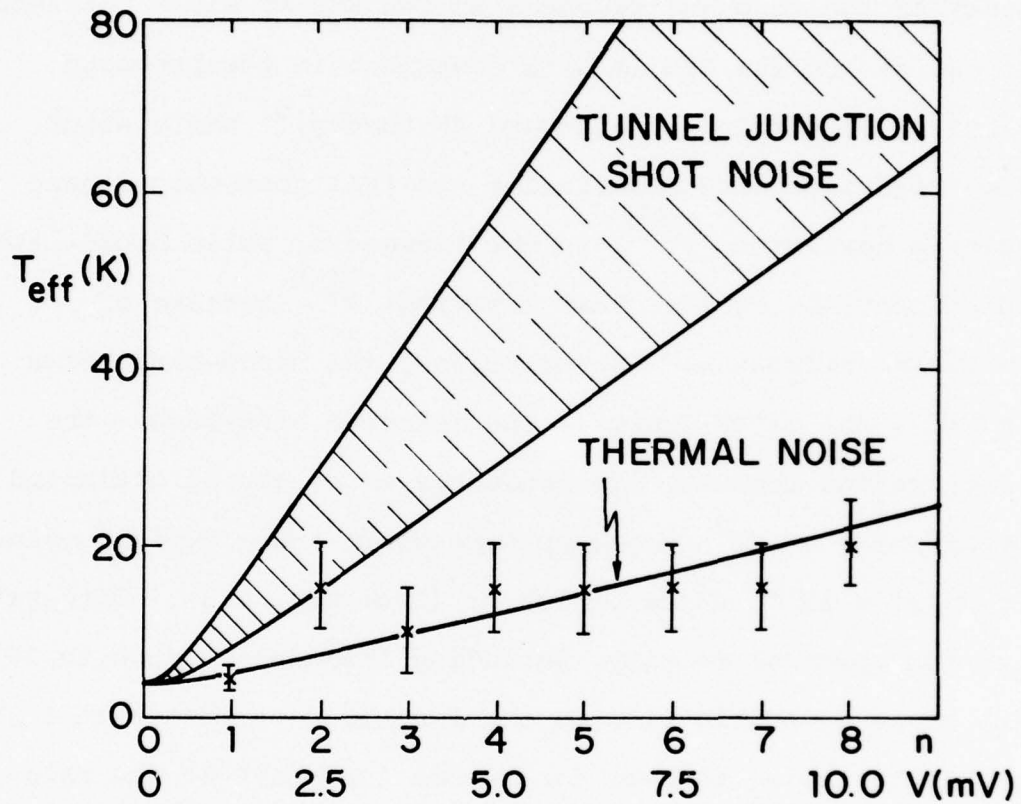
Fig. 6.4 The effective noise temperatures, from a fit of the shape of the 496-μm-laser-induced steps. The data is in good agreement with the calculated T_{eff} due to the heating-enhanced Johnson noise of a metallic constriction, but is substantially less than the shot noise predicted for a tunnelling-type contact.

could be important for practical devices: even at power
dissipation levels well below P_0, where the reduction in
the supercurrent due to heating is small, the effective
noise temperature can still be significantly larger than the
bath temperature.

As shown in Fig. 6.4, the measured T_{eff} are in good
agreement with the noise temperatures predicted by the heat-
ing theory of Tinkham et al.[6] In this theory, it is assumed
that the junction is a metallic constriction, and the local
temperature distribution due to power dissipation from both
the dc and the laser-induced currents is calculated. An
average of this local temperature weighted by the contribu-
tion of each element of the constriction to the resistance
of the contact gives an effective Johnson noise temperature,
T_{eff}. As shown in Fig. 6.4, the data seem inconsistent with
the much higher T_{eff} due to shot noise expected for a
tunnelling type of contact[80] at these voltage levels. The
level of shot noise would depend on the relative amounts of
"pair" and quasiparticle currents, but would be expected
to fall within the shaded region in Fig. 6.4. It is possible
that a metallic constriction might also show shot noise, but
only if its dimensions were much less than the electron
mean free path in the vicinity of the constriction,[49] which
appears not to be the case in our point contacts.[6] Neverthe-
less, these noise temperature data support the other experi-
mental evidence which suggests that junctions like ours are
modelled better as small metallic constrictions than as
tunnel junctions.

6.3 Low-Power Behavior of I_c

One of the peculiar features of our high-quality junc-
tions is the behavior of the I-V curves in the vicinity of
the critical current at low laser powers. Examples of dc
I-V curves with no incident laser radiation, and with the
critical current depressed by successively increasing powers
from the 496-μm-laser line, are shown in Fig. 6.5 for two
high-quality junctions with resistances of (a) 50 Ω and (b)
100 Ω. The effect of the low-level laser radiation is to
considerably reduce the dynamic resistance of the lower por-
tion of the voltage rise, so that there appears to be a
gradual voltage onset rather than the very steep onset seen
with no incident radiation. However, the steep upper por-
tion of the initial voltage rise and the excess current at
higher voltages are not reduced nearly as fast as the criti-
cal current. As the laser power is increased further and
the critical current passes through its first zero, this
effect becomes much less pronounced, with the initial voltage
onset not as gradual and the dynamic resistance becoming
somewhat larger again, as shown by the dotted I-V curves
in Fig. 6.5. We see similar low-laser-power behavior in all
our high-quality junctions, and for all the laser frequencies
used. Figure 6.6(a) shows a further example for an 80 Ω
junction irradiated by successively increasing powers of
119-μm-laser radiation. Similar behavior has also been
reported by others[88] using 2.3 mm (130 GHz) radiation, but

Fig. 6.5   A sequence of dc I-V curves of high-quality junctions with the critical currents successively depressed by increasing 496-μm-laser power. The critical currents of the dashed curves have passed through their first zero. Note the decrease in R_D at

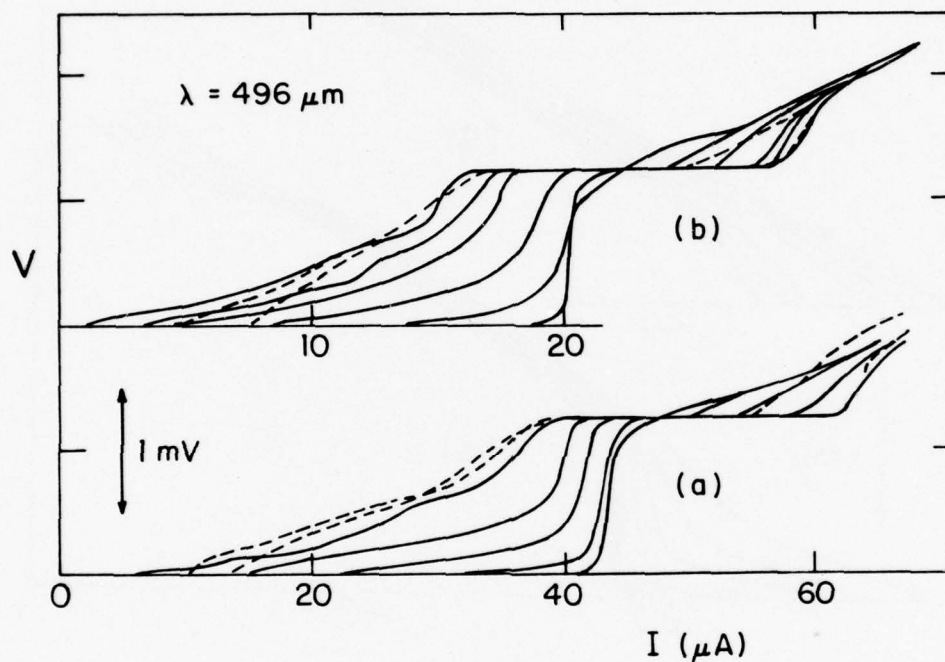the voltage onset as the laser power increases. The resistances of the junctions are (a) 50 Ω and (b) 100 Ω.
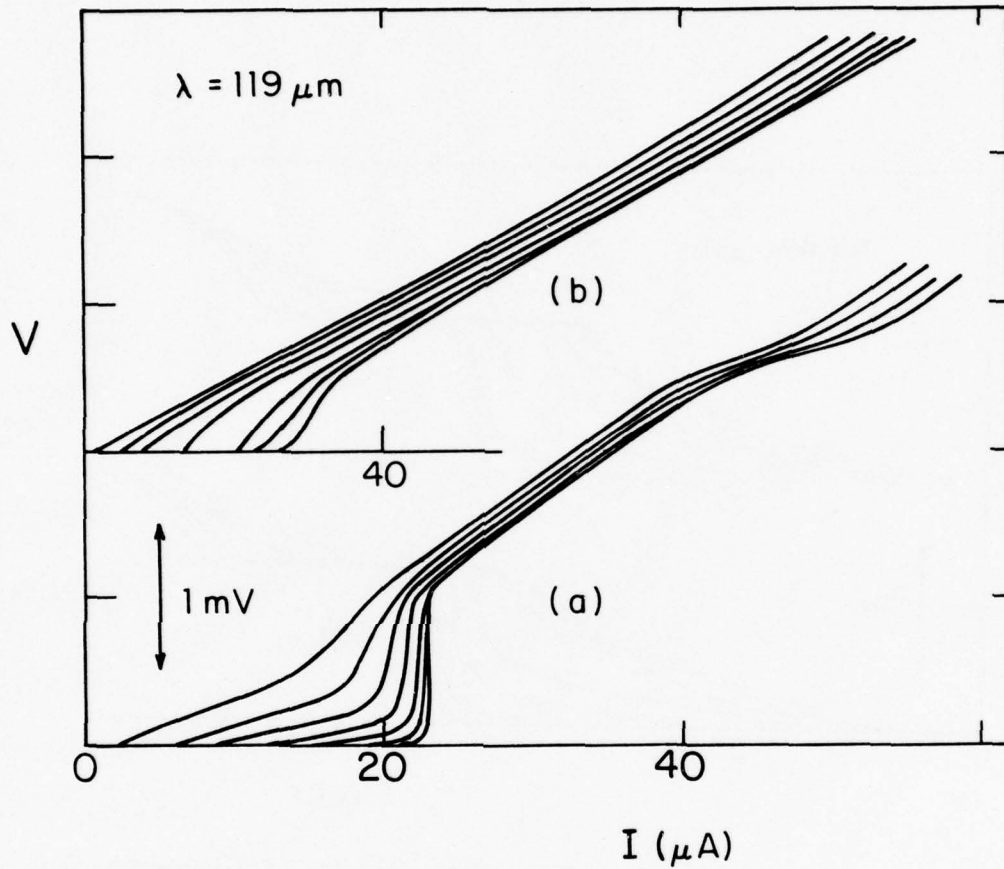
Fig. 6.6   A sequence of dc I-V curves with the critical
currents successively depressed by increasing 119-μm-
laser power. (a) High-quality junction, showing a
large decrease in the initial R_D and (b) poor-quality
junction, which does not show as large a decrease in
the initial R_D.

only for junctions that had $R \gtrsim 60 \; \Omega$ and that would not be labelled as high-quality in our classification scheme. This behavior contrasts with the RSJ prediction and with the reported behavior of point contacts with much lower $I_c R$ products,[92] where there is not such a large decrease in the initial R_D and the whole voltage onset moves to lower current levels as I_c is decreased. The latter behavior is observed in our poor-quality junctions, as shown by the example in Fig. 6.6(b) for 119 μm radiation.

The low-laser-power behavior of our "ideal" junctions may necessitate a reexamination of the optimum operating conditions if these junctions are used as mixers with external local oscillators (LO). Operation in this mode is usually optimized with the critical current reduced to $\sim \frac{1}{2} I_c$ by the LO power, and with the dc bias point set at about half the voltage of the first step.[88,93] However, good performance also requires that R_D be as high as possible. Thus if junctions like these are used as mixers, it may be necessary to operate with less LO power, to maintain a reasonably high R_D. We note that Edrich et al.[87] have reported excellent performance of a Josephson mixer-receiver that used a point contact whose I-V curve had a very large R_D at the voltage onset similar to our high-quality junctions. They obtained the best performance when the 300 GHz LO reduced I_c by only a few percent. Further experimental testing in a mixer configuration is necessary to fully address this issue.

6.4 Practical Devices

In the course of our experiments, we have identified those junctions that have the best high-frequency performance, and have studied their characteristics. However, the primary goal of our work has been a study of the high-frequency Josephson effect, and the main criterion for classifying and optimizing our point contacts was the existence of large Josephson steps well above the energy gap. In fact, our high-quality junctions may not be the optimum ones for some practical device applications, in which the Josephson effect at these very high frequencies might be less important. For example, stability requirements may favor more-oxidized junctions, even though their high-frequency performance is more limited. The difficulty in maintaining a stable dc bias on the very high dynamic resistance of the voltage onset of our high-quality junctions may also limit their use as mixers. However, in cases where excellent high-frequency performance is essential, junctions like these will probably be necessary.

One of the most promising applications of Josephson point contacts is their use as the nonlinear mixing element in heterodyne receivers. In this configuration, the signals from the source and an external local oscillator are mixed in the Josephson device to produce a beat signal at the difference frequency. This intermediate frequency (if) signal is usually in the MHz region, and is detected with conventional electronics. The high-frequency performance

of Josephson point-contact mixer-receivers has recently been reported by three groups.[87,88,94,95] In each case, the results were very encouraging, with mixer noise temperatures that compared favorably with the best non-Josephson devices at similar frequencies. The I-V curves of the junctions used by Claassen and Richards[88] at 130 GHz (2.3 mm) did not resemble those of our high-quality point contacts. However, at 300 GHz (1 mm), Edrich et al.[87] obtained the best performance with junctions whose I-V curves had many features in common with our high-quality I-V curves. At 450 GHz, Blaney[94,95] found that the best performance required the use of point contacts whose I-V curves closely resembled those of our high-quality junctions. Thus, it appears that the successful operation of Josephson point-contact mixers at FIR frequencies will require junctions like ours. Furthermore, these devices appear to be quite promising as low-noise mixers.

Josephson point-contact mixers are already widely used in metrology applications.[5] In this case, it is not their good sensitivity that is important, but rather their extreme nonlinearity, which makes them very effective mixing elements. Because they can generate very high harmonics of incident microwave radiation,[96] they are commonly used in frequency counting chains. The unknown FIR frequency is mixed with a harmonic of a well known microwave frequency. By using counting techniques to measure the if, the FIR frequency can be determined very accurately. Josephson point contacts

have even been used to mix two CO_2 lasers,[97] although the mechanism involved was probably bolometric rather than Josephson.[6] However, the difference frequency (~ 100 GHz) could be further down-converted with harmonics of microwaves, suggesting that the Josephson mixing action had not been completely washed out by heating effects. In these sorts of applications, point contacts similar to our high-quality junctions are always used.

If Josephson point contacts are to achieve wide use as practical devices in high-frequency applications, some technical problems must be overcome. The first of these is coupling. Although sufficient for our pruposes, our coupling scheme is inadequate when signal powers are small, as they are for detector applications. Considerable effort has been devoted to this problem recently. Blaney[94,95] has used microwave waveguide techniques very successfully at 450 GHz, and expects them to be effective up to ~900 GHz. At higher frequencies (1-1.5 THz), quasi-optical techniques have been successful with Schottky diodes,[98] and should be applicable to Josephson point contacts as well.

The second problem is the fragile nature of point contacts, and the fact that they must be adjusted in situ to obtain good performance. To be practical, a point contact should be fairly rugged, permanently adjusted, and able to withstand temperature cycling. Cross and Blaney[99] have had some success encapsulating Nb cat-whisker point contacts in

a glass with the same temperature coefficient of expansion
as the metal, but further improvements are required. If
these technical problems can be solved, Josephson point
contacts have the potential of finding wide use as practical
devices.

CHAPTER VII

CONCLUSIONS

These experiments were undertaken in an attempt to measure the FIR frequency dependence of the Josephson effect. Although a wide variety of superconducting devices show the Josephson effect, the high-frequency behavior of many of these is dominated by such extrinsic limitations as capacitive shunting and Joule heating. These limitations are avoided in niobium cat-whisker point contacts. Their minute size makes their capacitance very small,[5] while their three-dimensional geometry and relatively high impedance reduce Joule-heating effects.[6] Thus, a measurement of the _intrinsic_ frequency dependence of the strength of the Josephson effect seems to require the use of point-contact devices.

We have studied the Josephson effect by monitoring the constant-voltage steps induced on the dc I-V curves by radiation from an optically pumped far-infrared (FIR) laser. A fundamental step at voltage, V, is direct evidence of the existence of the Josephson effect at the frequency f = 2eV/h. By studying the power dependence of the current half-width of this step, we measure the strength of the Josephson effect at that frequency.

Our optically pumped FIR laser was of the high-efficiency, large-diameter, dielectric-waveguide type first suggested by

124

Hodges et al.[26] and now quite widely used. It was pumped by a CO_2 laser and, on strong lines gave ~10 mW in a nearly Gaussian, linearly-polarized output beam. One novel feature was our extension of the use of capacitive-mesh output couplers throughout the FIR spectrum, from 42 μm to 1.22 mm. In addition, we developed a hybrid capacitive-mesh hole coupler that gave improved performance at the shorter wavelengths.

The point contacts used in these experiments were made with a combination of mechanical adjustment and high-current-density burn-in, a technique we found to be quite successful for producing high-quality junctions. Based on the number of steps shown with the FIR radiation, the different types of junctions commonly obtained were classified, and their high-frequency behavior was correlated with the shape of the dc I-V curve.

We were able to identify a class of junctions that gave excellent high-frequency performance. These high-quality junctions were found to have quite reproducible, characteristic features on their dc I-V curves, including an $I_c R$ product near the theoretical maximum (~ 2.2 mV), a very sharp voltage rise of V_j ~ 0.5 $I_c R$, energy-gap voltages between ~2.8 and 3.1 mV, very pronounced gap structure, and an excess current of I_{ex} ~ 0.8 I_c above the gap. This now gives a useful prescription for recognizing high-quality junctions based on their dc I-V curves, without the need for

a high-frequency test.

To describe the sharpness of the structure at the energy gap we introduced the parameter S, defined as the ratio of the differential resistance just above the gap to the differential resistance just below the gap. We find that S is a more sensitive parameter than I_cR in determining the high-frequency behavior, and has a strong correlation with the highest voltage at which the ac Josephson effect still exists. Indeed, N_{max}, the highest harmonic step induced by 496 μm radiation, increases roughly linearly with S. Furthermore, high-quality junctions with $S \gtrsim 2.0$ always showed a step at 5.22 mV with 119 μm radiation. In contrast, we found no evidence to link the excess current to the ac Josephson effect.

We have compared the features of the dc I-V curves of our high-quality junctions with various theoretical predictions. The smooth, structureless RSJ curve provides a qualitative description, but does not contain any of the distinctive features of the data. McDonald et al.[50] have calculated the I-V curve of a current-biased, zero-capacitance tunnel junction using a frequency-dependent theory.[58] This prediction does show large currents below the gap (unlike the more familiar capacitance-dominated tunnel-junction I-V curve), but a more realistic handling of the gap singularity and a treatment of the effect of current-induced disequilibrium in the electrodes is necessary before any more-quantitative

comparisons with the data can be made. The major feature not accounted for by this model is the excess current above the gap. Calculations[60,61] which apply TDGL theory to short metallic constrictions have been shown to contain this feature with approximately the correct magnitude. This complements other experimental evidence which seems to support modelling our point contacts as very small metallic constrictions, rather than tunnel junctions. However, the distinction between the two models becomes somewhat blurred for the point-contact geometry, and a more realistic theoretical treatment seems necessary for a complete description of the data.

We have measured the power dependence of the step widths using FIR frequencies from 245 GHz to 2.52 THz. The data is quite reproducible from junction to junction, showing that high-quality point contacts are as consistent in their high-frequency behavior as in the shape of their dc I-V curves.

Taken as a whole, the power-dependence data seem to be reasonably well described by the shape predicted by a voltage-bias approximation of Werthamer's frequency-dependent theory.[58] The agreement is particularly convincing at the lower frequencies, where the fundamental step occurs at less than half the gap voltage. The many harmonic steps observed with these laser lines increase the amount of available data and provide more opportunities for detailed agreement with the theory.

For all the frequencies measured, the theoretical predictions must be scaled down by a factor of at least two to obtain a quantitative fit to the data. Some of this discrepancy is caused by heating-related effects. Our measurements of the heating parameters of our point contacts suggest that, at high laser powers, the supercurrent and hence the step widths will be reduced by $\sim(10-20)\%$. However, a more important effect of the heating is the increased effective noise temperature which causes additional rounding of the step edges. By using a fit to the noise-rounded RSJ model,[80] we have obtained an estimate of the necessary corrections to the data. Nevertheless, even after the data are adjusted to account for heating-related effects, there remains a significant discrepancy with the magnitude of the theoretical prediction.

We have used the maximum current half-width of the fundamental step normalized to the zero-power critical current, I_1^{max}/I_c, as a measure of the strength of the ac Josephson effect at the step voltage. By taking data with different FIR laser lines, and correcting each experimental value to account for the effects of noise rounding and heating, we obtain a measurement of the _intrinsic_ frequency dependence of the Josephson effect. The data follow the trend predicted by the voltage-bias version of Werthamer's frequency-dependent theory,[58] peaking near the gap and rolling off beyond. However, the measured values are consistently about a factor of two below the theoretical predictions. The cause of this

discrepancy is not known. Below the gap, the effects of a nonzero source impedance might cause a reduction in I_1^{max}/I_c, while above the gap, nonequilibrium relaxation time effects may offer an explanation for the discrepancy. Nevertheless, the data confirm the intrinsic roll off of the strength of the Josephson effect above the gap frequency.

The excellent high-frequency performance of our high-quality junctions makes them potentially useful for more practical applications. To investigate their potential further, we have made measurements of their characteristic noise levels, both with and without incident FIR radiation. Noise temperatures obtained from a fit of the laser-induced step shape[80] increase with bias voltage in agreement with the calculated[6] increase due to the additional Johnson noise caused by Joule heating at the contact. However, they are substantially less than the predicted effective temperatures due to the shot noise expected for a tunnelling type of contact.[80]

For low laser power and a dc bias in the vicinity of the incipient first step, the junction operates as a frequency-selective incoherent detector. Our best observed NEP at 604 GHz was $\sim 10^{-13}$ W$/\sqrt{Hz}$, and was limited by the voltage noise in our point contacts at the chopping frequency (450 Hz). We have measured the power spectrum of these voltage fluctuations from $\sim$10 Hz – 50 kHz, and find an approximately $1/f^2$ frequency dependence, so that we would expect the NEP

to be considerably improved at higher chopping frequencies.
Both the shape and the power dependence of the resonant
response near the first step agree with calculations[84] using
the resistively-shunted junction (RSJ) model when noise
and heating effects are included. Our best responsivity
at 604 GHz is 2×10^5 V/W, but this drops considerably at
higher frequencies. The responsivity predicted within the
RSJ model does not agree with the data, and more work is
necessary to explain the measurements more fully.

Finally, we have studied the behavior of the dc I-V
curves near the critical current when our high-quality
junctions are irradiated with low laser power. The dynamic
resistance of the voltage onset is considerably reduced as
the critical current is depressed. This behavior may be
important in understanding the performance of junctions like
ours when used as mixers with external local oscillators.

The results of our experiments suggest a number of
interesting questions which need further investigation.
The excellent performance of the high-quality point contacts
should now be tested in more practical coupling configura-
tions and in the favorable heterodyne mode of operation.
As a more fundamental question, it would be interesting to
test whether the characteristic shape observed with our
"ideal" junctions is also observed with point contacts made
from other materials. Tantalum would be particularly inter-
esting. It is a hard metal, as is niobium, and should
have the necessary mechanical properties to make good point

contacts. Furthermore, its lower T_c would simplify an investigation of the temperature dependence of the shape of the I-V curves. On the theoretical side, it would be desirable to have an improved agreement with the data for the roll off of the Josephson effect above the gap. This might require a more realistic treatment of the source impedance and the inclusion of nonequilibrium effects. An improved model might also give a better description of the characteristic shape of the I-V curves of our high-quality junctions. It is our hope that the reproducible and consistent behavior of junctions like ours will help stimulate the search for such a model.

REFERENCES

1. B.D. Josephson, Phys. Lett. $\underline{1}$, 251 (1962); Advan. Phys. $\underline{14}$, 419 (1965).

2. e.g. J. Niemeyer and V. Kose, Appl. Phys. Lett. $\underline{29}$, 380 (1976); C.L. Huang and T. Van Duzer, IEEE Trans. Magn. MAG-11, 766 (1975).

3. W.J. Skocpol, M.R. Beasley, and M. Tinkham, J. Appl. Phys. $\underline{45}$, 4054 (1974); S.K. Decker and D.W. Palmer, J. Appl. Phys. $\underline{48}$, 2043 (1977).

4. M. Octavio, W.J. Skocpol, and M. Tinkham, IEEE Trans. Magn. $\underline{MAG-13}$, 739 (1977).

5. J.E. Zimmerman, Proceedings of Appl. Superconductivity Conf., Annapolis, 1972, p. 544 (unpublished).

6. M. Tinkham, M. Octavio, and W.J. Skocpol, J. Appl. Phys. $\underline{48}$, 1311 (1977).

7. D.G. McDonald, V.E. Kose, K.M. Evenson, J.S. Wells, and J.D. Cupp, Appl. Phys. Lett. $\underline{15}$, 121 (1969).

8. D.A. Weitz, W.J. Skocpol, and M. Tinkham, J. Appl. Phy., to appear in Aug. 1978 issue.

9. D.A. Weitz, W.J. Skocpol, and M. Tinkham, Appl. Phys. Lett. $\underline{31}$, 227 (1977).

10. D.A. Weitz, W.J. Skocpol, and M. Tinkham, Phys. Rev. Lett. $\underline{40}$, 253 (1978).

11. D.A. Weitz, W.J. Skocpol, and M. Tinkham, to be published.

12. T.Y. Chang and T.J. Bridges, Opt. Commun. $\underline{1}$, 423 (1970).

13. Some recent compilations are: D.J.E. Knight, NPL Report no Qu 45 (National Physical Laboratory, Teddington, UK); M. Rosenbluh, R.J. Temkin, and K.J. Button, Appl. Opt. $\underline{15}$, 2635 (1976).

14. D.A. Weitz, W.J. Skocpol, and M. Tinkham, Opt. Lett., to appear in July 1978 issue.

15. T.A. DeTemple and E.J. Danielewicz, IEEE J. Quantum Electron. $\underline{QE-12}$, 40 (1976).

16. J.R. Tucker, Conf. Digest, International Conf. on Sub-millimeter Waves and Their Applications, Atlanta, June, 1974, p. 17.

17. J.O. Henningsen and H.G. Jensen, IEEE J. Quantum Electron. QE-11, 248 (1975).

18. D. Seligson, M. Ducloy, J.R.R. Leite, A. Sanchez, and M.S. Feld, IEEE J. Quantum Electron. QE-13, 450 (1977).

19. J.-M. Lourtioz and R. Adde, Conf. Digest, Third International Conf. on Submillimeter Waves and Their Applications, Guildford, 1978, p. 188.

20. J.M. Manley and H.E. Rowe, Proc. IRE 44, 904 (1956).

21. D.T. Hodges, F.B. Foote, and R.D. Reel, IEEE J. Quantum Electron. QE-13, 491 (1977).

22. D.T. Hodges and T.S. Hartwick, Appl. Phys. Lett. 23, 252 (1973).

23. M. Yamanaka, J. Opt. Soc. Am. 67, 952 (1977).

24. C.O. Weiss and G. Kramer, Appl. Phys. 9, 175 (1976).

25. T.Y. Chang and C. Lin, J. Opt. Soc. Am. 66, 362 (1976).

26. D.T. Hodges, F.B. Foote, and R.D. Reel, Appl. Phys. Lett. 29, 663 (1976).

27. Apollo Lasers model 550L.

28. A. Yariv, "Quantum Electronics, 2nd ed.", (John Wiley and Sons, New York, 1975), Chapter 7.

29. T.A. DeTemple, private communication.

30. E.A.J. Marcatili and R.A. Schmeltzer, Bell Syst. Tech. J. 43, 1783 (1964).

31. R.L. Abrams, IEEE J. Quantum Electron. QE-8, 838 (1972).

32. J.J. Degnan, Appl. Opt. 12, 1026 (1973).

33. Molectron model P4-73.

34. e.g. A.R. Chraplyvy, Appl. Opt. 15, 2022 (1976).

35. E.J. Danielewicz, T.K. Plant, and T.A. DeTemple, Opt. Commun. 13, 366 (1975).

36. M.R. Schubert, M.S. Durshlag, and T.A. DeTemple, IEEE J. Quantum Electron. QE-13, 455 (1977).

37. K.M. Evenson, D.A. Jennings, F.R. Peterson, J.A. Mucha, J.J. Jimenez, R.M. Charlton, and C.J. Howard, IEEE J. Quantum Electron. QE-13, 442 (1977).

38. S.M. Wolfe, K.J. Button, J. Waldman, and D.R. Cohn, Appl. Opt. 15, 2645 (1976).

39. R. Ulrich, Infrared Phy. 7, 37 (1967); R. Ulrich, K.F. Renk, and L. Genzel, IEEE Trans. Microwave Theory Tech. MTT-11, 363 (1963).

40. Buckbee Mears Co., St. Paul, Minn.

41. Measurements done by A.D. Smith.

42. L.M. Matarese and K.M. Evenson, Appl. Phys. Lett. 17, 8 (1970).

43. J.W. Dozier and J.D. Rodgers, IEEE Trans. Microwave Theory Tech. MTT-12, 360 (1964); MTT-12, 572 (1964) (E).

44. H. Tolner, J. Appl. Phys. 48, 691 (1977).

45. L.E. Hasselberg, M.T. Levinsen, and M.R. Samuelsen, Phys. Rev. B9, 3757 (1974), and references therein.

46. A.I. Akimenko, V.S. Solov'ev, and I.K. Yanson, Fiz. Nizk. Temp. 2, 480 (1976) [Soviet J. Low Temp. Phys. 2 238 (1976)].

47. O. Iwanyshyn and H.J.T. Smith, Phys. Rev. B6, 120 (1972).

48. I.K. Yanson, Fiz. Nizk. Temp. 1, 141 (1975) [Sov. J. Low Temp. Phys. 1, 67 (1975)].

49. A.B. Zorin and K.K. Likharev, Fiz. Nizk. Temp. 3, 148 (1977) [Sov. J. Low Temp. Phys. 3, 70 (1977)].

50. D.G. McDonald, E.G. Johnson, and R.E. Harris, Phys. Rev. B13, 1028 (1976).

51. R.F. Broom, J. Appl. Phys. 47, 5432 (1976).

52. J. Bostock, K. Agyeman, M.H. Frommer, and M.L.A. MacVicar, J. Appl. Phys. 44, 5567 (1973).

53. W. Schwarz and J. Halbritter, J. Appl. Phys. 48, 4618 (1977).

54. P.E. Gregers-Hansen and G.R. Pickett, Rev. Phys. Appl. 9, 145 (1974).

55. M. Octavio, Technical Report No. 13 (Tinkham Series) Division of Applied Sciences, Harvard University, 1978.

56. O. Hoffmann Soerensen, B. Kofoed, N.F. Pedersen and S. Shapiro, Rev. Phys. Appl. 9, 153 (1974).

57. O. Hoffmann Soerensen, B. Kofoed, N.F. Pedersen, and S. Shapiro, Phys. Rev. B9, 3746 (1974).

58. N.R. Werthamer, Phys. Rev. 147, 255 (1966).

59. D.E. McCumber, J. Appl. Phys. 39, 3113 (1968); W.C. Stewart, App. Phys. Lett. 12, 277 (1968).

60. K.K. Likharev and L.A. Yakobsen, Zh. Eksp. Teor. Fiz. 68, 1150 (1975) [Sov. Phys.-JETP 41, 570 (1976)].

61. A. Baratoff and L. Kramer, preprint.

62. J.E. Mooij and P. Decker, preprint.

63. B.S. Deaver and J.M. Pierce, Phys. Lett. 38A, 81 (1972).

64. T.J. Rieger, D.J. Scalapino, and J.E. Mercereau, Phys. Rev. B6, 1734 (1974).

65. W.J. Skocpol, M.R. Beasley, and M. Tinkham, J. Low Temp. Phys. 16, 145 (1974).

66. R.E. Harris, Phys. Rev. B10, 84 (1974).

67. S. Shapiro, A.R. Janus, and S. Holly, Rev. Mod. Phys. 36, 223 (1964).

68. C.A. Hamilton, Phys. Rev. B5, 912 (1972).

69. E. Riedel, Z. Naturforsch. A19, 1634 (1964).

70. S.A. Buckner and D.N. Langenberg, J. Low Temp Phys. 22, 569 (1976).

71. G. Vernet and R. Adde, Appl. Phys. Lett. 28, 559 (1976).

72. D.J. Scalapino and T.M. Wu, Phys. Rev. Lett. 17, 315 (1966).

73. P. Russer, J. Appl. Phys. 43, 2008 (1977).

74. V. Ambegaokar and A. Baratoff, Phys. Rev. Lett. 10, 486 (1963); 11, 104 (1963); L.G. Aslamasov and A.I. Larkin, JETP Lett. 9, 87 (1969).

75. R.E. Harris, Phys. Rev. B13, 3818 (1976).

76. R.E. Harris, J. Appl. Phys. 48, 5188 (1977).

77. D.A. Weitz, W.J. Skocpol, and M. Tinkham, Paper presented at the Third International Conference on Submillimeter Waves and Their Applications, Guildford, England (1978); Conf. Digest p. 211; and to be published in Infrared Phys.

78. C.A. Hamilton, Rev. Sci. Instr. 43, 445 (1972).

79. Calculations done by R. Tobin (unpublished).

80. M.J. Stephen, Phys. Rev. 182, 531 (1969); 186, 393 (1969); P.A. Lee, J. Appl Phys. 42, 325 (1971).

81. W.H. Henkels and W.W. Webb, Phys. Rev. Lett. 26, 1164 (1971).

82. L. Kramer and A. Baratoff, Phys. Rev. Lett. 38, 518 (1977).

83. T.D. Clark and P.E. Lindelof, Phys. Rev. Lett. 37, 368 (1976).

84. H. Ohta, M.J. Feldman, P.T. Parrish, and R.Y. Chiao, Rev. Phys. Appl. 9, 61 (1974).

85. C.C. Grimes, P.L. Richards, and S. Shapiro, J. Appl. Phys. 19, 3905 (1968).

86. H. Kanter and F.L. Vernon, Jr., J. Appl. Phys. 43, 3174 (1972).

87. J. Edrich, D.B. Sullivan, and D.G. McDonald, IEEE Trans. Microwave Theory Tech. MTT-25, 476 (1977).

88. J.H. Claassen and P.L. Richards, "Point Contact Josephson Mixers at 130 GHz," preprint.

89. R.F. Voss and J. Clarke, Phys. Rev. B13, 556 (1976).

90. J. Clarke and G. Hawkins, Phys. Rev. B14, 2826 (1976).

91. J.L. Stewart, Proc, IRE 42, 1539 (1954).

92. Y. Taur, P.L. Richards, and F. Auracher, "Low Temperature Physics-LT-13, Vol. 3, Superconductivity," edited by K.D. Timmerhaus, W.J. O'Sullivan, and E.F. Hammel (Plenum, New York, 1974) p. 276.

93. J.H. Claassen and P.L. Richards, "Performance Limits of a Josephson Junction Mixer," preprint.

94. T.G. Blaney, N.R. Cross, and R.G. Jones, Conf. Digest, Third International Conference on Submillimeter Waves and Their Applications, Guildford, England (1978), p. 258.

95. T.G. Blaney, National Physical Laboratory Report S.I. No. 89/0382 (Teddington, England, 1978).

96. D.G. McDonald, A.S. Risley, J.D. Cupp, K.M. Evenson, and J.R. Ashley, Appl. Phys. Lett. 20, 296 (1972).

97. D.G. McDonald, F.R. Petersen, J.D. Cupp, B.L. Danielson, and E.G. Johnson, Appl. Phys. Lett. 24, 335 (1974).

98. H.R. Fetterman, P.E. Tannenwald, B.J. Clifton, R.A. Murphy, and C.D. Parker, Conf. Digest, Third International Conference on Submillimeter Waves and Their Applications, Guildford, England (1978), p. 241; and preprint.

99. N.R. Cross and T.G. Blaney, private communication (1978).

ACKNOWLEDGEMENTS

138

Director
Advanced Research Projects Agency
Attn: Technical Library
1400 Wilson Boulevard
Arlington, Virginia 22209

Office of Naval Research
Electronics Program Office (Code 427)
800 North Quincy Street
Arlington, Virginia 22217

Office of Naval Research
Code 105
800 North Quincy Street
Arlington, Virginia 22217

Director
Naval Research Laboratory
4555 Overlook Avenua, S.W.
Washington, D.C. 20375
Attn: Technical Library (6 cps)
      Code 5200 (1 copy)
           5210 (1 copy)
           5270 (1 copy)
           6400 (1 copy)

Office of the Director of Defense
Research and Engineering
Office of the Assistant Director
Electronics & Physical Sciences
The Pentagon, Room 3D1079
Washington, DC 20301

Defense Documentation Center (12 cps)
Cameron Station
Alexandria, Virginia 22314

Commanding Officer
Office of Naval Research Branch Office
536 South Clark Street
Chicago, Illinois 60605

San Francisco Area Office
Office of Naval Research
50 Fell Street
San Francisco, California 94102

Commanding Officer
Office of Naval Research Branch Office
1030 East Green Street
Pasadena, California 91101

Commanding Officer
Office of Naval Research Branch Office
495 Summer Street
Boston, Massachusetts 02210

New York Area Office
Office of Naval Research
115 Broadway 5th Floor
New York, New York 10003

ODDR&E Advisory Group on Electron Devices
201 Varick Street
New York, New York 10014

Naval Air Development Center
Attn: Technical Library
Johnsville
Warminster, Pennsylvania 18974

Naval Weapons Center
China Lake, Califronia 93555
Attn: Technical Library (1 copy)
      Code 6010 (1 copy)

Naval Research Laboratory
Underwater Sound Reference Division
Technical Library
P.O. Box 8337
Orlando, Florida 32806

Navy Underwater Sound Laboratory
Technical Library
Fort Trumbull
New London, Connecticut 06320

Commandant, Marine Corps
Scientific Advisor (Code AX)
Washington, D.C. 20380

Naval Ordnance Station
Technical Library
Indian Head, Maryland 20640

Naval Postgraduate School
Monterey, California 93940
Attn: Technical Library (1 copy)
      Elect. Engin. Depart. (1 copy)

Naval Missile Center
Technical Library (Code 5632.2)
Point Mugu, California 93010

Naval Electronics Laboratory Center
San Diego, California
Attn: Technical Library (1 copy)
      Code 2300 (1 copy)
           2600 (1 copy)
           4800 (1 copy)

Naval Undersea Center
Technical Library
San Diego, California 92132

Naval Weapons Laboratory
Technical Library
Dahlgren, Virginia 22448

Naval Ship Research and Development Center
Central Library (Codes L42 and L43)
Washington, D.C. 20007

Naval Surface Weapons Center
White Oak Laboratory
Silver Spring, Maryland 20910
Attn: Technical Library (1 copy)
      Code 200 (1 copy)
           212 (1 copy)

Deputy Chief of Naval Operations
(Development)
Technical Analysis and Advisory Group
(Code NOP-077D)
Washington, D.C. 20350

Commander
Naval Air Systems Command
Washington, D.C.
ATTN: Code 310 (1 copy)
           360 (1 copy)

Commander
Naval Electronics Systems Command
Washington, D.C. 20360
Attn: Code 304 (1 copy)
           310 (1 copy)

Commander
Naval Sea Systems Command
Washington, D.C. 20360

Naval Surface Weapons Center
Attn: Library
Dahlgren, Virginia 22448

Air Force Office of Scientific Research
Attn: Electronic and Solid State
      Sciences Division
Department of the Air Force
Washington, D.C. 20333

Air Force Weapon Laboratory
Technical Library
Kirtland Air Force Base
Albuquerque, New Mexico 87117

Air Force Avionics Laboratory
Air Force Systems Command
Technical Library
Wright-Patterson Air Force Base
Dayton, Ohio 45433

Air Force Cambridge Research Laboratory
L.G. Hanscom Field
Technical Library
Cambridge, Massachusetts 02138

Harry Diamond Laboratories
Technical Library
Connecticut Avenue at Van Ness, N.W.
Washington, D.C. 20438

U.S. Army Research Office
Box CM, Duke Station
Durham, North Carolina 27706

Director
U.S. Army Engineering Research
and Development Laboratories
Fort Belvoir, Virginia 22060
Attn: Technical Documents Center

Director National Bureau of Standards
Attn: Technical Library
Washington, D.C. 20234

Naval Research Laboratory
4555 Overlook Avenue, S.W.
Washington, D.C. 20375
Attn: Code 5300 (1 copy)
           7100 (1 copy)
           7900 (1 copy)

Naval Electronics Laboratory Center
San Diego, California 92152
Attn: Code 2100 (1 copy)
           2200 (1 copy)

C.C. Klick
Superintendent
Materials Sciences Division
Naval Research Laboratory
4555 Overlook Avenue, S.W.
Washington, D.C. 20375

Naval Research Laboratory
4555 Oberlook Avenua, S.W.
Washington, D.C. 20375
Attn: Code 5220 (1 copy)
           5230 (1 copy)
           5250 (1 copy)
           5260 (1 copy)
           5270 (1 copy)
           5500 (1 copy)

Naval Electronics Laboratory Center
San Diego, California 92152
Attn: Code 2500 (1 copy)
           4000 (1 copy)

Office of Naval Research (2 cps)
800 N. Quincy Street
Arlington, Virginia 22217
Attn: Code 430 (2 copies)

Naval Research Laboratory
4555 Overlook Avenue, S.W.
Washington, D.C. 20375
Attn: Code 5400

Naval Electronics Laboratory Center
San Diego, California 92152
Attn: Code 3000 (1 copy)
           5000 (1 copy)
           5600 (1 copy)

Air Force Office of Scientific Research
Mathematical and Information Sciences
Directorate
1400 Wilson Blvd.
Washington, D.C. 20333

JSEP REPORTS DISTRIBUTION LIST

Director
National Security Agency
ATTN: Dr. T. J. Beahn
Fort George G. Meade, MD 20755

Defense Documentation Center
ATTN: DDC-TCA (Mrs. V. Caponio)
Cameron Station
Alexandria, VA 22314

Asst. Dir.
Office of Director of Defense
Research and Engineering
The Pentagon
Washington, DC 20315

Defense Advanced Research
Projects Agency
ATTN: (Dr. R. Reynolds)
1400 Wilson Boulevard
Arlington, VA 22209

Commandant
US Army Air Defense School
ATTN: ATSAD-T-CSM
Fort Bliss, TX 79916

Commander
US Army Armament R&D Command
ATTN: DRDAR-RD
Dover, NJ 07801

Commander
US Army Ballistic Research Lab.
ATTN: DRXRD-BAD
Aberdeen Proving Ground
Aberdeen, MD 21005

Commandant
US Army Command and General
Staff College
ATTN: Acquisitions, Lib. Div.
Fort Leavenworth, KS 66027

Commander
US Army Communication Command
ATTN: CC-OPS-PD
Fort Huachuca, AZ 85613

Commander
US Army Materials and Mechanics
Research Center
ATTN: Chief, Materials Sciences
Division
Watertown, MA 02172

Commander
US Army Materiel Development
and Readiness Command
ATTN: Technical Library, Rm.7S 35
5001 Eisenhower Avenue
Alexandria, VA 22333

Commander
US Army Missile R&D Command
ATTN: Chief, Document Section
Redstone Arsenal, AL 35809

Commander
US Army Satellite Communications
Agency
Fort Monmouth, NJ 07703

Commander
US Army Security Agency
ATTN: IARD-T
Arlington Hall Station
Arlington, VA 22212

Project Manager
ARTADS
EAI Building
West Long Branch, NJ 07764

Commander/Director
Atmospheric Sciences Lab. (ECOM)
ATTN: DRSEL-BL-DD
White Sands Missile Range, NM 88002

Commander
US Army Electronics Command
ATTN: DRSEL-NL-O (Dr. H.S. Bennett)
Fort Monmouth, NJ 07703

Director
TRI-TAC
ATTN: TT-AD (Mrs. Briller)
Fort Monmouth, NJ 07703

Commander
US Army Electronics Command
ATTN: DRSEL-CT-L (Dr. R. Buser)
Fort Monmouth, NJ 07703

Director
Electronic Warfare Lab. (ECOM)
ATTN: DRSEL-WL-MY
White Sands Missile Range, NM 88002

Executive Secretary, TAC/JSEP
US Army Research Office
P.O. Box 12211
Research Triangle Park, NC 27709

Commander
Frankford Arsenal
Deputy Director,
Pitman-Dunn Laboratory
Philadelphia, PA 19137

Project Manager
Ballistic Missile Defense Program Office
ATTN: DACS-DMP (Mr. A. Gold)
1300 Wilson Blvd.
Arlington, VA 22209

Commander
Harry Diamond Laboratories
ATTN: Mr. John E. Rosenberg
2800 Powder Mill Road
Adelphi, MD 20783

HQDA (DAMA-ARZ-A)
Washington, DC 20310

Commander
US Army Electronics Command
Fort Monmouth, NJ 07703
ATTN: DRSEL-TL-E (Dr. J.A. Kohn)
DRSEL-TL-EN (Dr. S. Kronenberg)
DRSEL-NL-T (Mr. R. Kulinyi)
DRSEL-NL-B (Dr. E. Lieblein)
DRSEL-TL-MM (Mr. N. Lipetz)
DRSEL-RD-O (Dr. W.S. McAfee)
DRSEL-NL-B (Dr. D.C. Pearce)
DRSEL-NL-MM-1 (Dr. F. Schwering)
DRSEL-TL-I (Dr. C.G. Thornton)

COL Robert Noce
Senior Standardization Representative
US Army Standardization Group, Canada
Canadian Force Headquarters
Ottawa, Ontario, Canada KIA K2

Director
Night Vision Laboratory
ATTN: DRSEL-NV-D
Fort Belvoir, VA 22060

Commander
Picatinny Arsenal
ATTN: SMUPA-TS-T-S
Dover, NJ 07801

Dr. Sidney Ross
Technical Director
SARPA-TD
Frankford Arsenal
Philadelphia, PA 19137

US Army Research Office (3cpe)
ATTN: Library
P.O. Box 12211
Research Triangle Park, NC 27709

Director
Division of Neuropsychiatry
Walter Reed Army Institute of
Research
Washington, DC 20012

Commander
White Sands Missile Range
ATTN: STEWS-ID-R
White Sands Missile Range, NM 88002

Mr. Robert Barrett
RADC/ETS
Hanscom AFB, MA 01731

Dr. Carl E. Baum
AFWL (ES)
Kirtland AFB, NM 87117

Dr. R. Champagne
AFAL/DH
Wright-Patterson AFB, OH 45433

Dr. R. P. Dolan
RADC/ETSD
Hanscom AFB, MA 01731

Mr. W. Edwards
AFAL/TE
Wright-Patterson AFB, OH 45433

Professor R.E. Fontana
Head, Dept. of Electrical Eng.
AFIT/ENE
Wright-Patterson AFB, OH 45433

Dr. Alan Garscadden
AFAPL/POD
Wright-Patterson AFB, OH 45433

USAF European Office of Aerospace
Research
ATTN: Major J. Gorrell
Box 14, FPO, New York 09510

LTC Richard J. Gowen
Dept. of Electrical Engineering
USAF Academy, CO 80840

Mr. Murray Kesselman (ISCA)
Rome Air Development Center
Griffiss AFB, NY 13441

Dr. G. Knausenberger
Air Force Member, TAC
Air Force Office of Scientific
Research
(AFSC) AFOSR/NE
Bolling Air Force Base, DC 20332

Dr. L. Kravitz
Air Force Member, TAC
Air Force Office of Scientific
Research
(AFSC) AFOSR/NE
Bolling Air Force Base, DC 20332

Mr. R. D. Larson
AFAL/DHR
Wright-Patterson AFB, OH 45433

Dr. Richard B. Mack
RADC/ETER
Hanscom AFB, MA 01731

Mr. John Mottsmith (MCIT)
HQ ESD (AFSC)
Hanscom AFB, MA 01731

Dr. Richard Picard
RADC/ETSL
Hanscom AFB, MA 01731

Dr. J. Ryles
Chief Scientist
AFAL/CA
Wright-Patterson AFB, OH 45433

Dr. Allan Schell
RADC/ETE
Hanscom AFB, MA 01731

Mr. H.E. Webb, Jr. (ISCP)
Rome Air Development Center
Griffiss AFB, NY 13441

LTC G. Wepfer
Air Force Office of Scientific
Research
(AFSC) AFOSR/np
Bolling Air Force Base, DC 20332

LTC G. McKemie
Air Force Office of Scientific
Research
(AFSC) AFOSR/NM
Bolling Air Force Base, DC 20332

Dr. R. S. Allgaier
Naval Surface Weapons Center
Code WR-303
White Oak
Silver Spring, MD 20910

Naval Weapons Center
ATTN: Code 5515 - H.F. Blazek
China Lake, CA 93555

Dr. H. L. Blood
Technical Director
Naval Undersea Center
San Diego, CA 95152

Naval Research Laboratory
4555 Overlook Avenue, SW
Washington, DC 20375
ATTN: Code 5200 - A. Brodzinsky
Code 7701 - J. D. Brown
Code 5210 - J. E. Davey
Code 5460/5410 - J.R. Davis
Code 5510 - W. L. Faust
Code 2627 - Mrs. D. Folen

Naval Ocean Systems Center
ATTN: Code 75 - W.J. Dejka
271 Catalina Boulevard
San Diego, CA 92152

Naval Weapons Center
ATTN: Code 601 - F.C. Essig
China Lake, CA 93555

Dr. Robert A. Fossum
Dean of Research
Naval Postgraduate School
Monterey, CA 93940

Dr. G. G. Gould
Technical Director
Naval Coastal System Lab.
Panama City, FL 32401

Naval Ocean Systems Center
ATTN: Code 7203 - V.E. Hildebrand
271 Catalina Boulevard
San Diego, CA 92152

Naval Ocean Systems Center
ATTN: Code 753 - P.H. Johnson
217 Catalina Boulevard
San Diego, CA 92152

Donald E. Kirk
Professor and Chairman
Electronic Engineer, SP-304
Naval Postgraduate School
Monterey, CA 93940

Naval Air Development Center
ATTN: Code 01 - Dr. R. K. Lobb
Johnsville
Warminster, PA 18974

Naval Research Laboratory
ATTN: Code 5270 - B.D. McCombe
4555 Overlook Avenue, SW
Washington, DC 20375

Capt. R.B. Meeks
Naval Sea Systems Command
NC 43
2531 Jefferson Davis Hwy
Arlington, VA 20362

Dr. H. J. Mueller
Naval Air Systems Command
Code 310
JP 01
1411 Jefferson Davis Hwy
Arlington, VA 20360

Dr. J.H. Mills, Jr.
Naval Surface Weapons Center
Electronics Systems Department
Code DF
Dahlgren, VA 22448

Naval Ocean Systems Center
ATTN: Code 702 - H.T. Mortimer
271 Catalina Boulevard
San Diego, CA 92152

Naval Air Development Center
ATTN: Technical Library
Johnsville
Warminster, PA 18974

Naval Ocean Systems Center
ATTN: Technical Library
271 Catalina Boulevard
San Diego, CA 92152

Naval Research Laboratory
Underwater Sound Reference Division
Technical Library
P.O. Box 8337
Orlando, FL 32806

Naval Surface Weapons Center
ATTN: Technical Library
Code DX-21
Dahlgren, VA 22448

Naval Surface Weapons Center
ATTN: Technical Library
Building 1-330, Code WX-40
White Oak
Silver Spring, MD 20910

Naval Training Equipment Center
ATTN: Technical Library
Orlando, FL 32813

Naval Underseas Center
ATTN: Technical Library
San Diego, CA 92152

Naval Underwater Systems Center
ATTN: Technical Library
Newport, RI 02840

Office of Naval Research
Electronic & Solid State Sciences
Program (Code 427)
800 North Quincy Street
Arlington, VA 22217

Office of Naval Research
Mathematics Program (Code 432)
800 North Quincy Street
Arlington, VA 22217

Office of Naval Research
Naval Systems Division
Code 220/221
800 North Quincy Street
Arlington, VA 22217

Director
Office of Naval Research
New York Area Office
715 Broadway, 5th Floor
New York, NY 10003

Office of Naval Research
San Francisco Area Office
One Hallidie Plaza - Suite 601
San Francisco, CA 94102

Director
Office of Naval Research Branch
Office
495 Summer Street
Boston, MA 02210

Director
Office of Naval Research Branch
Office
536 South Clark Street
Chicago, IL 60605

Director
Office of Naval Research Branch
Office
1030 East Green Street
Pasadena, CA 91101

Mr. H. R. Riedl
Naval Surface Weapons Center
Code WR-34
White Oak Laboratory
Silver Spring, MD 20910

Naval Air Development Center
ATTN: Code 202 - T. J. Shoppie
Johnsville
Warminster, PA 18974

Naval Research Laboratory
ATTN: Code 5403-J. E. Shore
4555 Overlook Avenue, SW
Washington, DC 20375

A. L. Slafkovsky
Scientific Advisor
Headquarters Marine Corps
MC-RD-1
Arlington Annex
Washington, DC 20380

Harris B. Stone
Office of Research, Development,
Test and Evaluation
NOP-987
The Pentagon, Room 5D760
Washington, DC 20350

Mr. L. Sumney
Naval Electronics Systems Command
Code 3042, NC 01
2511 Jefferson Davis Hwy.
Arlington, VA 20360

David W. Taylor
Naval Ship Research and
Development Center
Code 522.1
Bethesda, MD 20084

Naval Research Laboratory
ATTN: Code 4105-Dr. S. Teitler
4555 Overlook Avenue, SW
Washington, DC 20375

Lt.Cdr. John Turner
NAVMAT 0343
CP 05, Room 1044
2211 Jefferson Davis Hwy.
Arlington, VA 20360

Naval Ocean Systems Center
ATTN: Code 746-N.H. Wieder
271 Catalina Boulevard
San Diego, CA 92152

Dr. W. A. Von Winkle
Associate Technical Director
for Technology
Naval Underwater Systems Center
New London, CT 06320

Dr. Gernot M. R. Winkler
Director, Time Service
US Naval Observatory
Massachusetts Avenue at
34th Street, NW
Washington, DC 20390

Dr. Howard W. Etzel
Deputy Director
Division of Materials Research
National Science Foundation
1800 G Street
Washington, DC 20550

Mr. J. C. French
National Bureau of Standards
Electronics Technology Division
Washington, DC 20234

Dr. Jay Harris
Program Director
Devices and Waves Program
National Science Foundation
1800 G Street
Washington, DC 20550

Los Alamos Scientific Laboratory
ATTN: Reports Library
P.O. Box 1663
Los Alamos, NM 87544

Dr. Dean Mitchell
Program Director
Solid-State Physics
Division of Materials Research
National Science Foundation
1800 G Street
Washington, DC 20550

Mr. F. C. Schwenk, RD-T
National Aeronautics and Space
Administration
Washington, DC 20546

M. Zane Thornton
Deputy Director,Institute for
Computer Sciences and Technology
National Bureau of Standards
Washington, DC 20234

Director
Columbia Radiation Laboratory
Columbia University
538 West 120th Street
New York, NY 10027

Director
Coordinated Science Laboratory
University of Illinois
Urbana, IL 61801

Director of Laboratories
Division of Applied Sciences
Harvard University
Pierce Hall
Cambridge, MA 02138

Director
Electronics Research Center
The University of Texas
Engineering-Science Bldg. 112
Austin, TX 78712

Director
Electronics Research Laboratory
University of California
Berkeley, CA 94720

Director
Electronics Sciences Laboratory
University of Southern California
Los Angeles, CA 90007

Director
Microwave Research Institute
Polytechnic Institute of New York
333 Jay Street
Brooklyn, NY 11201

Director
Research Laboratory of Electronics
Massachusetts Institute of
Technology
Cambridge, MA 02139

Director
Stanford Electronics Laboratory
Stanford University
Stanford, CA 94305

Stanford Ginzton Laboratory
Stanford University
Stanford, CA 94305

Officer in Charge
Carderock Laboratory
Code 18-G.H. Gleissner
David Taylor Naval Ship Research
and Development Center
Bethesda, MD 20084

Dr. Roy F. Potter
3868 Talbot Street
San Diego, CA 92106

ED

78